Control Loop Interactions and Their Mitigation Schemes in VSC-HVDC Systems

by

Fatemeh Ahmadloo

A thesis
presented to the University of Waterloo
in fulfillment of the
thesis requirement for the degree of
Doctor of Philosophy
in
Electrical and Computer Engineering

Waterloo, Ontario, Canada, 2022

Examining Committee Membership

The following served on the Examining Committee for this thesis. The decision of the Examining Committee is by majority vote.

External Examiner: Rajiv Kumar Varma
Professor, Dept. of ECE, University of Western Ontario

Supervisor: Sahar Pirooz Azad
Assistant Professor, Dept. of ECE, University of Waterloo

Internal Member: Mehrdad Kazerani
Professor, Dept. of ECE, University of Waterloo

Internal Member: Kankar Bhattacharya
Professor, Dept. of ECE, University of Waterloo

Internal-External Member: Baris Fidan
Professor, Dept. of MME, University of Waterloo

Author's Declaration

I hereby declare that I am the sole author of this thesis. This is a true copy of the thesis, including any required final revisions, as accepted by my examiners.

I understand that my thesis may be made electronically available to the public.

Abstract

In line with two goals of the United Nations, i.e., providing affordable and clean energy as well as combating climate change, various converter-interfaced renewable energy sources (RESs) are being integrated into the power systems. The transfer of renewable power generated by the RESs such as offshore wind farms to remote load centers may require the use of direct current (DC) lines, which are connected to the alternating current (AC) grid via AC-DC converters. In addition to facilitating the reliable connection of RESs to the power grid, high-voltage DC (HVDC) lines may be used for the transcontinental exchange of power to transfer power over long distances.

One of the major challenges in the evolution of AC systems to hybrid AC-DC systems is the control of converters. Each converter station owns various control loops that require proper tuning in their stand-alone mode of operation. Furthermore, control loops of adjacent converters may also impact one another, and as a result, there must be coordination among the control design of converters to guarantee stability and appropriate dynamic response of the entire grid. The control loop interactions among the converters worsen with increasing the size of the system and the number of converters, especially when one converter station is already in operation and re-tuning the converter's controllers is not an option. Another important aspect of future AC-DC power grids is the employment of converters built by multiple vendors, who will take part in the development of converter controllers with unique designs and know-how. These independently designed controllers will form a part of the grid control system. In this scenario, the stability of the entire system is of great importance and needs to be verified due to control loop interactions.

This thesis studies both internal and external control loop interactions in voltage-sourced converters (VSCs) embedded in AC-HVDC systems. This thesis, first, studies the internal control loop interactions, where the control loops within one single converter interact with one another, and develops a method to design the individual control loops within a VSC such that the converter stability is ensured. A metric is proposed to measure interaction levels, and the impact of interactions on set-point tracking capability is also investigated.

This thesis, next, considers the connections among various converters either from the AC side or the DC side and studies the external control loop interactions among the adjacent converters. Regarding the external control loop interactions caused by DC side connections, suitable system models are introduced to enable individual control design for the converters in a multi-terminal DC (MTDC)-HVDC grid. As for the AC side external control loop interactions, two scenarios are considered: 1) the converters are in the grid-following (GFL) mode of operation, and 2) the converters are in the grid-forming (GFM) mode of operation. Regarding the GFL mode of operation, the impact of control modes on the interactions is studied, and the control modes causing the highest interaction levels are identified. A novel control design framework is designed to relate the control design of each converter to the interconnected system stability. The multi-vendor issue then is considered, and the interactions are mitigated by designing individual robust controllers or by employing interaction filters. The interaction analyses are then extended to the parallel connection of GFM converters and hybrid connections of GFL and GFM converters. Stability and coupling analyses are performed among GFL and GFR converters. small-signal stability of parallel GFM converters is proved, and real-time simulations and hardware-in-the-loop-test are performed for validating the studies.

Acknowledgements

First and foremost, I dedicate my sincere thanks to my supervisor professor Sahar Pirooz Azad for all her guidance and support throughout my Ph.D. studies. She supported me, had faith in me, and opened up many opportunities so that I can learn and grow. I am truly grateful for having such a strong woman as a role model in my life.

I would like to sincerely thank the respected committee members for their time and the valuable comments that they provided. It has been an honor for me to finish my thesis with their support and feedback.

I would like to dedicate my greatest thanks to my wonderful family for everything they have done for me to become the person I am today. I have come this far because of their love and their sacrifices. This accomplishment would not have been possible without them.

Last but not least, I am grateful for having amazing friends on this journey. Their love will be a part of me forever.

Dedication

To mom and dad for their never-ending love and their sacrifices.

"*Don't hope for better. Just be better. Be something better. Be more compassionate, more resilient, more humble, more disciplined*" [Mark Manson], because "*from little seeds grow mighty trees.*" [unknown author]

Table of Contents

List of Tables

List of Figures

List of Abbreviations

AC Alternating Current 1

APCL Active Power Control Loop 1

APCM Active Power Control Mode 1

AVCL AC Voltage Control Loop 1

BESS Battery Energy Storage System 1

DC Direct Current 1

dq Direct-Quadrature 1

DVCL DC Voltage Control Loop 1

DVCM DC Voltage Control Mode 1

EMT Electromagnetic Transient 1

GFL Grid-Following 1

GFM Grid-Forming 1

HIL Hardware In-the-Loop 1

HVDC High Voltage DC 1

IEA International Energy Association 1

IF Interaction Filter 1

IFSYS Interaction-Free System 1

INDSYS Individual System 1

INTSYS Interconnected System 1

ISTF Interconnected Multi-VSC System Transfer Function 1

LHP Left-Half Plane 1

LTI Linear Time-Invariant 1

MTDC Multi Terminal DC System 1

PCC Point of Common Coupling 1

PLL Phase-Locked Loop 1

RES Renewable Energy Source 1

RGA Relative Gain Array 1

RPCL Reactive Power Control Loop 1

SCR Short Circuit Ratio 1

VSTF Vendor-Specific Transfer Function 1

WPP Wind Power Plant 1

Chapter 1

Introduction

1.1 Motivation

In line with two goals of the United Nations, i.e., providing affordable and clean energy as well as combating climate change, various converter-interfaced renewable energy sources (RESs) are being integrated into the power systems. According to the International Energy Association (IEA) report, RESs including wind, solar, and hydroelectric power will be the fastest-growing energy sources shaping a secure and sustainable energy system by 2050 [10, 76]. The transfer of renewable power generated by the RESs such as offshore wind farms to remote load centers may require the use of direct current (DC) lines, which are connected to the alternating current (AC) grid via voltage-sourced converters (VSCs). In addition to facilitating the reliable connection of RESs to the power grid, high-voltage DC (HVDC) lines may be used to transfer power over long distances [6]. Compared to high-voltage AC transmission lines, HVDC lines appear to be more efficient for bulk transmission of power over long distances due to lower investment costs, lower losses, and better controllability. Furthermore, HVDC transmission provides the possibility of asynchronous connections between AC systems and creates a firewall against the severe blackouts that are otherwise cascaded over different areas [26, 78]. HVDC lines can also be used to provide electricity to offshore platforms with minimal harmful impacts on the surrounding environment. Some examples of HVDC projects around the world are given in Table 1.1.

The integration of RESs within the grid and the transmission of power over long distances have resulted in various alterations in power grids. One example is the formation of multi-terminal direct current (MTDC) systems, where the DC system is connected to

Table 1.1: Some HVDC projects around the world [1, 2, 7]

Commissioning	Project Name	Country	Rating(MW)	Manufacturer
2018	Maritime Link	Canada	500 MW	ABB
2010	Trans Bay Cable	USA	400MW	Siemens
2023	DolWin6	Germany	900	Siemens
2023	Creyke Beck A, UK	UK	1200	ABB
2021	ULTRANET	Germany	2000	Siemens
2020	ElecLink	UK-France	1000	Siemens
2019	Nemo Link	UK-Belgium	1000	Siemens
2020	ElecLink	UK-France	1000	ABB
2010	Caprivi Link	Namibia - Gerus	300	ABB
Ready for infeed	DolWin3	Germany	900	GE
2017	Rio Maderia Bipole II	Brazil	3150	GE
2015	Xiamen, Fujian Province	China	1000	C-EPRI

the AC system via VSCs [78]. The general idea behind the formation of a global ”super grid” is to expand the existing point-to-point HVDC connections to multi-terminal and then meshed configurations, as shown in Fig. 1.1 [78]. Unlike point-to-point configurations, multi-terminal HVDC systems create the possibility of having different tappings on

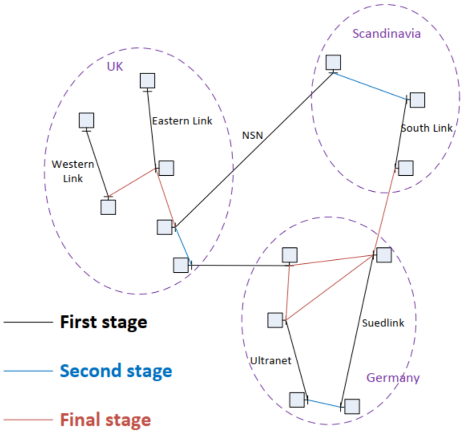

Figure 1.1: Different stages of a DC grid development in Europe [11].

the DC side, and thus power can be transferred to different areas, or new sources of power can be easily added to the DC side. Furthermore, meshed DC systems can decrease the number of converters used on the DC side to provide alternative paths for power to flow if an outage occurs [78]. Therefore, in the future hybrid AC-DC systems, several converters may be located in close proximity.

Another important aspect of future super grids is the employment of converters built by multiple vendors, who will take part in the development of converter controllers with unique designs and know-how. These independently designed controllers will form a part of the grid control system. In this scenario, the stability of the entire system is controversial and needs to be verified due to control loop interactions. A significant concern in the multi-vendor realization of super grids is the confidentiality of information of each party. Confidentiality requires an independent design of converter controllers with limited information about the design of other parties. As an example, the converter stations embedded in the HVDC system of the Johan Sverdrup (JS) project are planned to be designed and commissioned in two phases. In the first phase, the in-operation line of the JS HVDC project was built by ABB. Another line is going to be added to this project by Siemens in the second phase. Therefore, at the end of this project, two HVDC lines and the associated converter stations from two different suppliers will be located in close proximity. As full models cannot be exchanged between the suppliers, and the suppliers have created individual designs, interaction testing is required to integrate the two HVDC lines and converter stations. The interaction testing and the required changes in each supplier's design will be performed by a third party through an iterative process. The test cases will be run, and the reports generated will be used to direct suppliers in modifying their designs [8]. Fig. 1.2 shows a schematic diagram of the JS HVDC project.

1.2 Statement of the Problem and Objectives

An interaction is defined as a situation in which the components within the HVDC system affect each other, causing the system response to deviate from the intended one. The VSCs embedded in AC-HVDC systems are controllable devices and own several control loops. Control loop interactions occur when the control loops within one converter affect each other or those of the neighbouring converter(s). The two types are respectively referred to as internal and external control loop interactions. It should be underlined that the control loop interactions depend not only on the controllers and their parameters but also on the physical connection among the converters [25]. Thus, external control loop interactions are due to the interactions of nearby converters connected to each other on the AC side or due

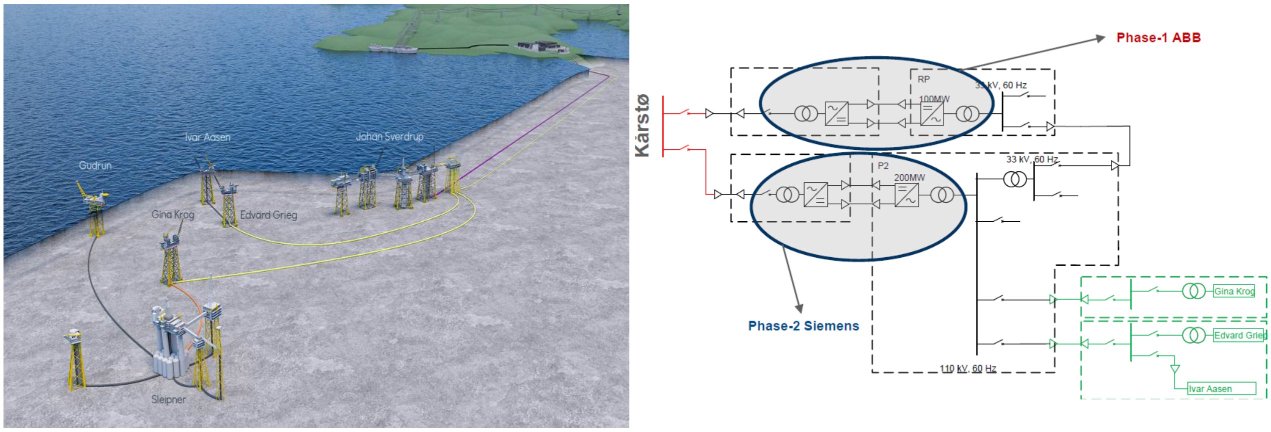

Figure 1.2: Johan Sverdrup HVDC project [8].

to likely interactions with converters connected to a shared DC system. The configuration of the DC system impacts the latter, while the connection at the AC side impacts the former.

This thesis focuses on both internal and external control loop interactions in VSCs embedded in AC-HVDC systems. Fig. 1.3 shows a general classification of different types of control loop interactions. As for the configuration of the system under study, two types of connections are considered: I) converters are connected to the same AC grid and share the same point of common coupling (PCC), and II) converters share a common DC system. The exact configuration of the DC system is not the focus of this research; the only requirement is to have some connections among the converters at the DC side so that their control loops' mutual impact on one another can be studied. As for the adjacent AC system, because this research does not address the impact of control loops of converters on those of the AC system and vice-versa, the AC system is modelled as a voltage source behind an impedance.

The main objectives of this thesis are listed below:

1. Internal control loop interactions:
    - To study the impact of internal control loop interactions on the stability and performance of a VSC.
    - To study different parameters that impact interactions.
    - To mitigate the internal interactions by tuning the controller parameters.

2. External DC side control loop interactions:
    - To study the external control loop interactions among the converters connected to a shared DC system.
    - To develop system models for control design to mitigate the interactions.
3. External AC side control loop interactions:
    - To study the interactions among grid-following converters sharing the same PCC and analyze the impact of the control mode on the interactions.
    - To develop control design methods to mitigate the interactions in converters sharing the same PCC with multi-vendor considerations.
    - To develop interaction filters to mitigate the interactions in converters sharing the same PCC with multi-vendor considerations.
    - To study the impact of control philosophy, i.e., grid-following and grid-forming, on the stability and level of interactions in parallel converters connected to a shared PCC.
    - To study the stability of parallel grid-forming converters connected to a shared PCC.

1.3 Methodology

The following methodology is used to achieve the objectives mentioned in Section 1.2.

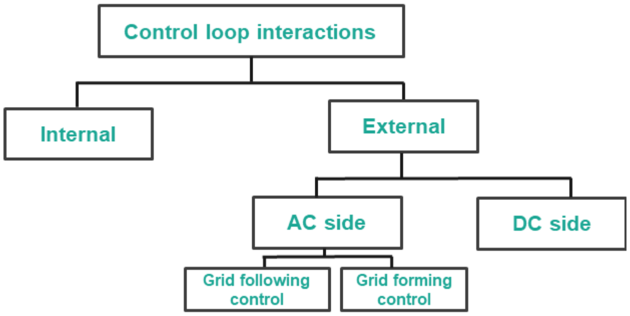

Figure 1.3: Classification of control loop interactions in VSC-HVDC systems

- Construct linear and nonlinear averaged models (type 6 model defined in CIGRE B4.57 [48]) of a single VSC, VSCs connected to a common AC system, and VSCs connected to a common DC system.

- Develop detailed equivalent circuit models (type 4 model defined in CIGRE B4.57 [48]) in EMT software environments such as EMT/SIMULINK and PSCAD.

- Perform model validation to evaluate the consensus between the detailed and averaged models.

- Obtain the state-space and transfer function models of each one of the averaged models.

- Study the internal and external control loop interactions using the state-space and transfer function models, and design controllers and interaction filters to mitigate the interactions.

- Perform time-domain simulations in Matlab/SIMULINK and EMT software environment to evaluate the validity of the interaction studies and controller designs. All the time-domain simulations are performed under small disturbances (small-signal stability and dynamic performance).

- Validate the results of offline EMT simulations using real-time simulations and hardware-in-the-loop (HIL) tests.

1.4 Thesis Outline

This thesis is prepared in nine chapters. Chapter 2 reviews the available studies on control loop interactions in VSC-HVDC systems. Chapter 3 addresses the internal control loop interactions within one VSC. Chapter 4 studies the DC side control loop interactions. Chapter 5 focuses on the AC side external control loop interactions. Chapter 6 and Chapter 7 present methods for mitigating control loop interactions in parallel VSCs with multi-vendor considerations. Chapter 8 focuses on the AC side external control loop interactions among grid-following and grid-forming converters, and chapter 9 concludes the thesis and recommends future lines of research.

Chapter 2

Literature Review

2.1 Introduction

This chapter presents a review of the available studies on control loop interactions in voltage-sourced converter (VSC)-high-voltage direct current (HVDC) systems. The chapter is categorized into two sections: internal control loop interactions and external control loop interactions. The latter is classified based on the type of interactions (DC side and alternating current (AC) side) and the control philosophy under which each converter is controlled (grid-forming (GFM) and grid-following (GFL)).

2.2 Internal Control Loop Interactions

VSCs embedded in HVDC systems are usually controlled in the direct (d)-quadrature (q) rotating reference frame based on a cascaded scheme, where the inner loops control the current, and the d-axis and q-axis outer control loops regulate the DC voltage or active power and the AC voltage or reactive power, respectively [86]. Moreover, a phase-locked-loop (PLL) is utilized to align the dq-reference frame with the voltage at the point of common coupling (PCC) and to synchronize the rotation speed of the reference frame with the AC grid frequency [86], [83]. Assuming that the VSC active and reactive power control loops are decoupled at steady-state if the AC grid is stiff [86], a large number of studies on the design of VSC controllers offer solutions based on independent control of d-axis and q-axis control loops [20–22, 77, 83, 88]. However, the outer control loops in a VSC interact with one another when VSC is connected to a weak AC system [23,35] or even to a strong AC system [83].

To properly design the individual d-axis and q-axis control loops as well as PLL, first, the impact of control loop interaction on VSC stability should be analyzed. This issue has been addressed in several studies using i) time-domain simulations [28,95], ii) modal analysis [44,46], iii) Nyquist plots [44], iv) Bode diagrams [46,97], and v) the equivalent of the motion equation of synchronous generators for VSCs. [47,80,88].

Using time-domain simulations, [95] illustrates that PLL gain strongly affects the stability of VSCs connected to weak AC systems, whereas it can be neglected in the stability analysis of VSCs connected to strong AC systems [28]. In [46], using modal analysis and Bode diagrams, the impact of changing the controller gains of the DC voltage control loop (DVCL) and the AC voltage control loop (AVCL) on the location of eigenvalues of a single VSC and consequently stability is analyzed. In [44], modal analysis and the DC gain of transfer functions is used to study the impact of interactions among PLL, DVCL and AVCL on the power stability limit. The modal analysis in [81] addresses the resonance between PLL and DVCL and its impact on VSC stability. Using Bode diagrams, the impact of PLL on DVCL stability is studied in [97] (considering PLL and DVCL) and [46] (considering PLL, DVCL, and AVCL). The similarity between the dynamic behaviour of DC voltage and that of a synchronous generator's rotor is used in [47,80,88] to study the impact of interactions on stability. Several dynamic indices based on H_∞ norm of transfer functions are proposed in [17] to quantify the level of interactions among the control loops in the DC link time-scale.

In addition to the studies that showed the negative impact of control loop interactions on VSC stability and dynamic performance, using eigenvalue and modal analysis, several papers provided controller tuning methods to improve VSC stability. For example, increasing the proportional gain of the AVCL controller [44,88] and decreasing that of PLL [44] were proposed to improve VSC stability. In [46], the bandwidths of PLL and DVCL were selected far from each other to minimize the interactions. [15] modified the control loops by adding two blocks to d-axis and q-axis control loops to shape the output impedance of the converter and to stabilize the converter even in weak grids. Additionally, [23] proposed a re-tuning of the controllers with a fast AVCL and a slow PLL for weak AC systems where an individual tuning of the controllers did not result in satisfactory performance of VSCs.

The stability of a VSC in above-mentioned studies is achieved by simultaneous tuning of the parameters of all control loops. Furthermore, most of the existing analytical investigations into the control loop interactions are limited to the study of overall system eigenvalues and the change in their locus with respect to the controller gains. Therefore, a method based on the tuning of the individual outer control loops (d- and q-axis controllers as well as PLL), rather than the interconnected control system, is required to reduce the control loop interactions that may destabilize the VSC especially in case of weak AC systems. Besides, the impact of interactions on the set-point tracking capability of control loops as well as quantitative assessment of the level of interactions among the control loops are not explored in the literature.

2.3 External Control Loop Interactions

The are two main types of external control loop interactions depending on the connection of converters on the AC or DC side of the grid. These interactions are discussed in this section.

2.3.1 DC side control loop interactions

The trend toward an increased number of converters in multi-terminal direct current(MTDC) systems has turned AC-MTDC system stability into a compelling topic that has been studied in several papers [25,30,34,40,52,53,59,87,89]. As shown in [25], in an MTDC system, there might exist several interactive system modes that are associated with more than one converter and with DC transmission lines. These interactive modes are different from the local modes that originate from one single converter or only the DC system. These interactive modes stem from the dynamic interactions among the converter stations and the DC system components that are not considered in the control design of individual converters [25, 30]. Due to these interactive modes, the connection of converters to a shared DC system may result in poorly-damped or unstable modes as the eigenvalue locus of the interconnected AC-MTDC system may differ from that of the individual converters' models for which the controllers are designed [52].

Three approaches have been proposed in the literature to address the undesired impact of interactive system modes on the AC-MTDC system performance. The first approach is to modify the control system of the converters based on the interconnected system modes, as suggested in [25]. This process requires the entire AC-MTDC system model and might be iterative, costly, and time-consuming, specifically if the number of converters and thus the number of state and controlled variables is large. The second approach to prevent poorly damped or oscillatory interactive system modes is to employ supplementary controllers for each converter station, obtained through an impedance matching process by solving an optimization problem [14,16]. The drawbacks of such an approach are associated with the selection of appropriate weighting functions and the cost of adding an additional controller to each converter. Simultaneous design of the controllers for all the converter stations, considering the entire AC-MTDC system dynamics, is the third approach that is used in [24] to mitigate the poorly damped modes and stabilize the system through solving an optimization problem. However, as the size of an MTDC system increases, achieving a simultaneous control design for all the converter stations may be challenging.

Given the drawbacks of the aforementioned approaches, another approach to prevent interconnected AC-MTDC system instability is to involve the interactive modes in the individual design of converter controllers. To do so, suitable system models, which do not rely on the full dynamic model of the AC-MTDC system, but include the interactive system modes, are required for converters' controller design. However, most of the system models employed in stability and interaction analyses of AC-MTDC systems are the current source based models, where the adjacent converters are modeled as current sources and the dynamics of the DC system are not considered [16, 25, 30, 34, 40, 52, 60, 71, 73, 83, 84]. Furthermore, in some studies, the components included in the model of each converter are not clearly described, and it is not evident whether the couplings among the converters are considered in the control design [36, 54, 57, 59, 89]. In the interconnected AC-DC system model in [25,29,39], the converters are modeled by their equivalent droop or current source model, but how the interactive modes can be incorporated into the model of individual converters is not discussed. As a result, suitable individual system models are required to enable designing converter controllers independent of those of the adjacent converters connected to a shared DC system.

2.3.2 AC side control loop interactions

In large-scale power systems with high integration of renewable energy sources (RESs), multiple VSCs may be connected to a shared PCC, causing the adjacent converters to interact with one another through their PCCs and cause instability and an undesirable transient response [45, 79]. Although the control loop interactions might happen among the control loops of one single VSC [28, 44, 46, 47, 80, 88, 95, 97], the interactions among the control loops of several converters will hinder the integration of large-scale RESs into the AC grid. Various factors may impact the AC- side external control loop interactions, which will be elaborated upon in the following subsections.

Impact of control mode

A VSC usually includes three main control loops in the dq-frame: a d-axis control loop, a q-axis control loop, and a PLL. Depending on the VSC's operating mode (control mode), the d-axis control loop can regulate either the DC voltage or active power, and the q-axis control loop may regulate the AC voltage or reactive power [86]. Although there are several control loops in a VSC, the literature does not pay specific attention to the impact of VSCs' control modes on the external control loop interactions [45, 67–70, 72, 79, 82].

Specific sets of control modes have been selected for external control loop interaction studies in the existing literature. The DC voltage/AC voltage control mode is considered in [45] for all VSCs, while the inner current loops are neglected. In [45], the interaction of each VSC with the adjacent VSC is modeled by a transfer function, and Bode diagrams are employed to study the impact of the AC system short circuit ratio (SCR) and changes in the active power of adjacent VSCs on the interactions and consequently on system stability. The interaction analysis in [79] is based on a comparison of the stability regions of individual and interconnected VSCs, but only the DC voltage control loop is considered, and the dynamics of the PLL and the q-axis outer control loop are ignored. [72] attempts to identify the VSC control mode that results in maximum interactions between a VSC and a STATCOM by using relative gain array (RGA) analysis. The studies provided in [72] are not comprehensive as the impact of the d-axis control mode on interactions is not considered, and the RGA analysis has only been used to study the interactions among control loops under the steady-state condition and for a specific control mode. [16] utilizes RGA to find the frequency at which the maximum interactions occur among converters connected to a shared DC system. This frequency is later used to obtain weighting functions for an H_∞ controller design. Interactions among PLLs of multiple VSCs sharing the same PCC are studied in [67, 68]. By considering VSCs as ideal current sources and neglecting the d-axis and q-axis control loops, [67, 68] examine the impact of interactions between PLLs on stability using the output impedance of VSCs. In [69, 70], interactions between a grid-following and a grid-forming VSC are studied. A robust stability margin with respect to system parametric uncertainties is defined in [70] using μ analysis, and an eigenvalue analysis is employed in [69] to illustrate the impact of connecting VSCs with different control philosophies to the same PCC on system stability. Neither the converters' controller nor the control mode is the focus in [69, 70]; thus, the outer control loops of the grid-following VSC are not involved in the analysis.

The limitations associated with the existing interaction studies can be summarized as follows: I) The impact of converters' control mode on the interactions is not explored, and the studies are performed considering a specific set of control modes for each converter.

Although the control mode may not be a design choice for any legal or operational reasons, the impact of control modes on the interactions is of high importance as it can facilitate the design of converters' controllers to reduce the interactions and improve system stability. II) The outer control loops and consequently, various control modes of converters are neglected in several interaction studies. This is because the focus of such studies is on identifying system parameters impacting the interactions. III) the existing studies about the impact of controller design on external control loop interactions are limited to the study of overall system eigenvalue locus as the controller gains change. The findings of these studies cannot be applied to the individual controller design of converters such that the interconnected system is stabilized as well. Making a connection between tuning the controllers of individual and interconnected VSCs to stabilize the multi-VSC system is missing from these studies.

Multi-vendor considerations

Another issue with the connection of converters to a shared AC system is the multi-vendor realization of VSC-based hybrid AC-DC systems that has attracted considerable attention in recent years [32]. Recent studies, based on industrial replicas of converter control and protection systems, have shown the feasibility of constructing HVDC systems with multiple vendors [27]. The formation of hybrid AC-DC systems from converters built by different manufacturers may result in interoperability issues including control interactions [64]. These control interactions may stem from the impact of independently designed converter controllers, due to model confidentiality, on one another and consequently on the performance of the interconnected systems [16, 19, 79]. In the multi-vendor realization of hybrid AC-DC systems, vendor-specific models are used in the design of individual converter controllers. Typically, vendor-specific models are proprietary and confidential, and the vendors' know-how in converters' detailed model and control design is not shared with other converter manufacturers. Therefore, integrating the independently designed VSCs into an interconnected system of converters may result in system instability and undesirable dynamic response, whose root cause is the control interaction among the converters and participation of various converters' state variables in particular eigenvalues [25].

Connecting multiple VSCs built by various vendors to a shared PCC results in various control challenges due to the interactions among the converters, which may lead to the interconnected converters' response deviating from the desired one. Although the individual converters with independently designed controllers may be stable, their connection to a PCC may cause system instability [79]. The level of converter interactions and the severity of their impact on the system's dynamic behavior depend on various factors such as the AC system short circuit ratio [45, 79], the active power set-point of converters [45], the bandwidth of PLLs [67, 68], and the controller gains [79].

The *BestPaths* project is the first systematic study using electromagnetic transients (EMT) and real-time simulation tools to assess and resolve interoperability issues caused by the multi-vendor realization of HVDC systems [3, 32, 64]. In the *BestPaths* project, several HVDC test cases with various DC side topologies were considered to identify interoperability issues. In these studies, an interoperability issue is identified if the performance of the interconnected AC-DC system is deteriorated when multi-vendor converter models are employed, but is improved when single-vendor converter models are utilized. In [32], about 15% of the case studies reveal interoperability issues, where the root cause of a number of them is the difference in the control implementation of the converters due to confidentiality requirements. So far, the proposed solutions to mitigate the interactions in real-world projects have been based on an iterative process such as that in John sverdrup's HVDC project. A list of information is agreed to be shared between the parties before the start of the project. The design has been performed by Siemens and ABB, and an interaction study is performed by a third party. At the end of interaction studies, certain solutions are provided to the vendors to modify their designs [9].

Mitigating converter control interactions in multi-vendor AC-DC systems is a challenge because the controllers that are independently designed based on the vendor-specific models are employed in an interconnected AC-DC system. Reference [37] optimizes the converters' droop settings to lessen the AC system dynamic variations caused by the outage of a VSC connected to a shared DC system. However, neither the independently designed controllers nor the impact of converters on one another during the system's normal operation is considered in the analysis. In recent years, only a few methods have been proposed to mitigate the interactions among converters with independently designed controllers. A supplementary controller is proposed in [13, 16], which is obtained by solving an impedance matching problem, to address the multi-vendor realization of converters sharing a DC system, but not an AC system.

Mitigating the interactions among converters connected to a PCC to properly integrate VSCs with independently designed controllers into an interconnected multi-VSC system is not addressed in the literature.

Impact of control philosophy

A VSC in an AC-DC power system can be controlled either to follow the AC grid specifications (grid-following) using a PLL or to replicate a voltage source (grid-forming). The

GFL converters mostly are controlled through the cascaded inner-outer current loops and as a result, resemble the behavior of a current source. The GFM converters, on the other hand, are controlled to form the characteristics of a voltage source. Literature has studied the issues associated with the GFL converters extensively: issues with connection to weak AC grids [12, 23, 31, 63, 81, 94, 95], the interaction of various control loops [18, 44, 81, 92], and inability to operate in the stand-alone mode [62] count as the main drawbacks of GFL converters. On the other hand, GFM converters have shown improvement in system stability even under weak AC systems [50, 85, 90, 98], but are not mature enough to be used in real-world applications [63] and still are under development. Several variants of GFM control schemes have been proposed in the literature, including virtual synchronous generator [51, 56], synchronverter [93], virtual synchronous generator [43], power synchronization control (PSC) [90], and IP PLL-free control [62], to name but a few. A comprehensive review on the available GFM control techniques can be found in [63].

To be able to use the capabilities of both GFM and GFL control schemes, connecting converters with different control philosophies seems a possible solution. Parallel connection of converters with hybrid control philosophies have been considered in [70, 85, 98] . Using small-signal stability analysis, it has been shown in [85, 98] that connecting a grid-forming converter to the AC grid is equivalent to increasing the grid strength. The optimal location of GFM converters is also obtained through solving an optimization problem [85]. The robust stability of the parallel connection of a GFL and a GFM converter is studied in [70], where the GFL converter is modeled as an ideal current source without considering the outer control loops. It is shown that the GFM converter increases the robust stability margin of the two-VSC system. The interactions among a battery energy storage system (BESS) operated under PSC scheme and the adjacent wind power plant (WPP) are studied in [91]. The interaction analysis shows that the coupling between the voltage reference and power is significant. [98] proposes guidelines for designing controllers of the GFL and GFM in a two-bus system.

Although the available studies show that connecting a GFM converter to the AC grid improves system stability, an open question is whether a GFL converter can be replaced by a GFM control scheme when several converters are connected to the same AC system.

2.4 Summary

This chapter presented a background review of the available control loop interaction studies in VSC-HVDC systems. The studies were classified based on the type of interaction analysis they performed, i.e., internal or external control loop interactions. The gaps in the existing studies were highlighted, which will be addressed in the following chapters of this thesis.

Chapter 3

Internal Control Loop Interactions[1]

3.1 Introduction

This chapter studies how the interactions among various control loops in a single voltage-sourced converter (VSC) affect the stability, transient response, and set-point tracking capability of control loops. This chapter develops a method based on the tuning of the individual outer control loops (direct (d)- and quadrature (q)-axis controllers as well as phase-locked loop (PLL)), rather than the interconnected control system, to reduce the control loop interactions that may destabilize the VSC, especially in case of weak AC systems. The developed method does not modify the individual controllers' structure and leverages the individual control design stage to determine a feasible range of control parameters that stabilizes the interconnected control system of VSCs by reducing the interactions among the control loops. Compared to control design methods based on Nyquist plots and eigenvalue and modal analyses [44,46,88], in which the stability of VSC is achieved by simultaneous tuning of the parameters of all control loops, the developed method designs the individual controllers separately and provides the range of individual control loop parameters, which results in the stability of the interconnected control system. Furthermore, most of the existing analytical investigations into the control loop interactions are limited to the study of overall system eigenvalues and the change in their locus with respect to the controller gains. This chapter investigates the impact of interactions on individual control loops in addition to the impact on overall system stability. Besides, the impact of interactions on the set-point tracking capability of control loops as well as

---

[1] Ahmadloo, Fatemeh, and Pirooz Azad, Sahar. "Analysis of Internal Control Loop Interactions in VSCs: An Individual Design Perspective." IEEE Transactions on Power Delivery 37.3 (2021): 1465-1475.

quantitative assessment of the level of interactions among the control loops, which have not been explored in the literature, are addressed in this chapter.

3.2 VSC Small-Signal Model

The schematic of a VSC with its control loops in the dq rotating reference frame is shown in Fig. 3.1. The fundamental small-signal model of a VSC is provided in [83, 86]. In the small-signal model presented in this section, the inner current control loops and several possible combinations of outer control loops are considered. The resistive part of the AC grid impedance is also considered in this model.

As indicated in Fig. 3.1, the VSC is controlled in a cascaded scheme, and the outer control loops provide the set-points of the inner current control loops. Thus, the control signals of the inner and outer control loops are respectively, given by

$$u_x = \underbrace{(K_p^{in,x} + K_I^{in,x} \int)}_{K^{in,x}(s)} (i_x^* - i_x); \quad x \in \{d, q\}, \tag{3.1}$$

$$i_x^* = \underbrace{(K_p^{o,x} + K_I^{o,x} \int)}_{K^{o,x}(s)} (y_x^* - y_x); \quad x \in \{d, q\}, \tag{3.2}$$

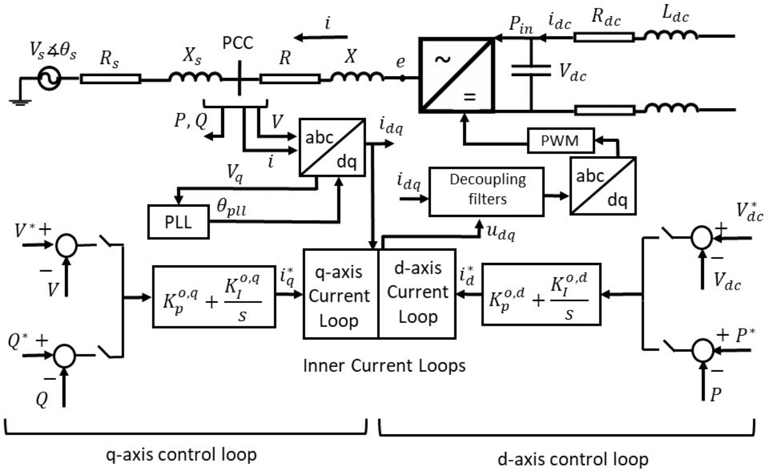

Figure 3.1: The schematic of a VSC with its control loops.

where i_d and i_q are the dq-components of the current at the AC side, the superscript * indicates the reference signal, and y_d (y_q) and u_d (u_q) are, respectively, the output and control signal of the d-axis (q-axis) control loop. The outputs of DC voltage control loop (DVCL) and active power control loop (APCL) are, respectively, the DC voltage (V_{dc}) and the active power (P). The reactive power (Q) and the AC voltage (V) serve as the outputs of reactive power control loop (RPCL) and AC voltage control loop (AVCL), respectively. The feed-forward decoupling filters are considered in the last step in Fig. 3.1 to remove the cross-couplings between d-axis and q-axis inner current loops [86]. The gains of inner current controllers are assumed to be constant [86], and the controllers of the outer control loops are designed individually to ensure the stability and proper performance of the d-axis and q-axis control loops. The outer control loops are designed to be slower than the inner current loops for the proper operation of the cascaded control scheme [88].

The small-signal model of the VSC is obtained by linearizing all the nonlinear equations associated with the active and reactive power at the PCC, the DC link voltage, the AC voltage, and the voltage-current relationship at the VSC terminal around an operating point [44, 83, 86]. The fundamental nonlinear equations are given in the following.

The dynamic model of the AC side of the converter in the dq frame is given by [83]

$$e_d - V_d = L\frac{\mathrm{d}i_d}{\mathrm{d}t} + Ri_d - \omega L i_q, \tag{3.3}$$

$$e_q - V_q = L\frac{\mathrm{d}i_q}{\mathrm{d}t} + Ri_q + \omega L i_d, \tag{3.4}$$

where e_{dq} and V_{dq} are the terminal voltage of the converter and PCC voltage, respectively. This dynamic model can be re-written using the terminal voltage of the converter and the source voltage as

$$e_d - V_s cos\theta_{ps} = L_t\frac{\mathrm{d}i_d}{\mathrm{d}t} + R_t i_d - \omega L_t i_q, \tag{3.5}$$

$$e_q + V_s sin\theta_{ps} = L_t\frac{\mathrm{d}i_q}{\mathrm{d}t} + R_t i_q + \omega L_t i_d, \tag{3.6}$$

where R_s, L_s and R, L are the resistance and inductance of AC gid and the filter, respectively, $R_t = R + R_s$, $L_t = L + L_s$, and $\theta_{ps} = \theta_{pll} - \theta_s$, θ_{pll} is the angle provided by the PLL, and θ_s is the source-voltage angle. Utilizing appropriate modulation signals [86], which realize the decoupling of the inner current loops, as

$$e_d = V_d + u_d - \omega L i_q, \tag{3.7}$$

$$e_q = V_q + u_q + \omega L i_d, \tag{3.8}$$

where ω is the angular frequency, the d- and q-components of the voltage at the PCC can be described using the algebraic equations of

$$V_d = \frac{L_s}{L_t}\, e_d + \frac{LR_s - L_sR}{L_t}\, i_d + \frac{L}{L_t}\, V_s cos\theta_{ps}, \tag{3.9}$$

$$V_q = \frac{L_s}{L_t}\, e_q + \frac{LR_s - L_sR}{L_t}\, i_q - \frac{L}{L_t}\, V_s sin\theta_{ps}. \tag{3.10}$$

Having the d- and q-components of the voltage and current, the active and reactive powers at the PCC can be computed as

$$P = V_d i_d + V_q i_q, \tag{3.11}$$

$$Q = V_q i_d - V_d i_q. \tag{3.12}$$

Also, the magnitude of the PCC voltage is given by

$$V = \sqrt{V_d^2 + V_q^2}. \tag{3.13}$$

The dynamics of the DC link voltage are described by

$$C_{dc}\frac{\mathrm{d}V_{DC}}{\mathrm{d}t} = i_{dc} - \frac{P_{in}}{V_{DC}}\ , \tag{3.14}$$

where C_{dc} is the DC link capacitance, and P_{in} is the active power from the DC side.

In the rest of this chapter, $\tilde{x}$ refers to the deviation of variable x from its operating point x_0, i.e., $\tilde{x} = x - x_0$.

Fig. 3.2 presents the small-signal block diagrams of PLL, d-axis control loops (DVCL and APCL), and q-axis control loops (RPCL and AVCL). Table 3.1 presents the control loops coefficients based on the converter's control mode. In Fig. 3.2, all the inputs that are associated with the other control loops are identified as external inputs. For example, $\tilde{\theta}_{ps}$ and $\tilde{u}_q$ correspond to PLL and the q-axis control loop and are identified as the external inputs to the d-axis control loop. Similarly, $\tilde{\theta}_{ps}$ and $\tilde{u}_d$, which correspond to PLL and the d-axis control loop, appear as external inputs to the q-axis control loop. Likewise, $\tilde{u}_d$ and $\tilde{u}_q$ are the external inputs to PLL. The control loops are not combined to allow for the study of the impact of interactions on the individual control loops. Throughout this chapter, the term *"individual control loops"* refers to each of d-axis control loop, q-axis control loop,

Table 3.1: The coefficients of d-axis and q-axis control loops.

Coefficients	Control Mode	
	DVCL	APCL
a_0	-1	1
a_1	$V_s(cos\theta_{ps_0} i_{q0} + sin\theta_{ps_0} i_{d_0})$	
a_2	1	0
a_{21}	$-\omega L_s i_{d_0} + \frac{LR_s - L_s R}{L}\ i_{q0}$	
a_{22}	$\frac{L_s}{L}\ i_{q0}$	
a_3	$C_{dc}s - \frac{P_0}{V_{dc_0}^2}$	1
a_4	V_{dc_0}	1
a_5	$\omega L_s i_{q_0} + V_{d_0} + \frac{LR_s - L_s R}{L}\ i_{d_0}$	
a_6	$\frac{L_s}{L}\ i_{d_0}$	
Coefficients	Control Mode	
	RPCL	AVCL
a_7	$V_s(sin\theta_{ps_0} i_{q_0} - cos\theta_{ps_0} i_{d_0})$	-$V_s sin\theta_{ps_0}$
a_{81}	$\omega L_s i_{d_0} - \frac{LR_s - L_s R}{L}\ i_{q0}$	$\frac{LR_s - L_s R}{L}$
a_{82}	$-\frac{L_s}{L}\ i_{q0}$	$\frac{L_s}{L}$
a_9	$\omega L_s i_{q_0} - V_{d_0} + \frac{LR_s - L_s R}{L}\ i_{d_0}$	$-\omega L_s$
a_{10}	$\frac{L_s}{L}\ i_{d_0}$	0

and PLL enclosed by solid boxes in Fig. 3.2 with no connection to one another. The overall block diagram of Fig. 3.2 is referred to as the "*interconnected control system*".

As shown in Fig. 3.2, the control loops in a VSC are not inherently decoupled, and

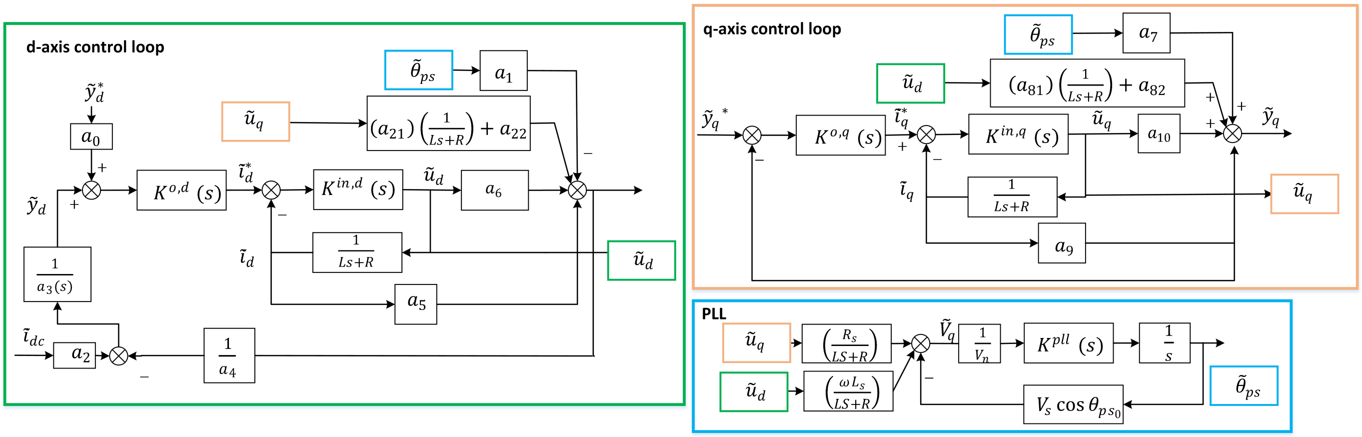

Figure 3.2: The small-signal model of all the control loops in a VSC.

the level of coupling among them depends on the operating point and the AC system low short circuit ratios (SCR). A lower SCR results in a stronger coupling between the d-axis and q-axis control loops as a_{21}, a_{22}, a_{81}, and a_{82}, which are the coupling coefficients of the d-axis and q-axis control loops, are directly proportional to the AC system impedance. Furthermore, a lower SCR results in a larger ωL_s that is the coupling coefficient relating the d-axis control loop to PLL.

It should be noted that in the rest of the analysis, no perturbation from the DC side, represented by $\tilde{i}_{dc}$ in Fig. 3.2, is considered as the aim is to study the interactions among the control loops of a single converter.

3.3 Analysis of Control Loop Interactions

This section, first, investigates the impact of control loop interactions on the stability regions of the d-axis and q-axis control loops. Second, using a novel formulation and utilizing the small-gain theorem, a subset of individually-tuned controller gains, which stabilize the interconnected control loop of VSC, is presented. Third, the impact of interactions on the transient response of the d-axis and q-axis control loops is investigated. Fourth, the interaction level between control loops is determined based on the infinity norm of specific transfer functions. Finally, the impact of interactions on the set-point tracking capability of the control loops is studied.

3.3.1 Impact of interactions on system stability

Fig. 3.3a shows a simple schematic of VSC for stability analysis, which is obtained by substituting each control loop of Fig. 3.2 with two transfer functions G_{yx} from the external inputs (generated by loop x) to the control signals of loop y. The set-points are eliminated as the aim of this section is to examine stability. To ensure the VSC stability, all the individual control loops and the interconnected control system of Fig. 3.3 must be stable. As a result, the stability region of the interconnected control system may be smaller than those of the individual control loops.

Fig. 3.3b shows the signal flow graph [58] of the system in Fig. 3.3a. Using Fig. 3.3b, the characteristic polynomial of the interconnected control system is given by the numerator of

$$P(s) = 1 - [G_{dq}G_{qd} + G_{\theta q}G_{q\theta} + G_{d\theta}G_{\theta d}] - [G_{d\theta}G_{\theta q}G_{qd} + G_{dq}G_{q\theta}G_{\theta d}]. \tag{3.15}$$

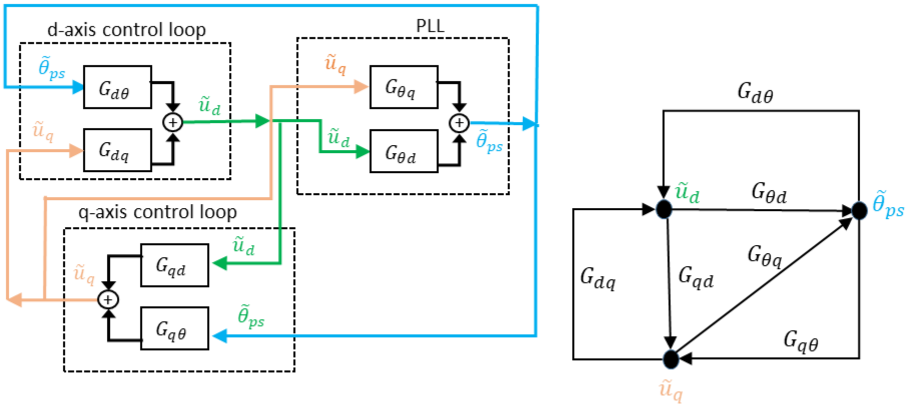

(a) (b)

Figure 3.3: (a) The schematic of the interconnected control loops of the VSC for stability analysis and (b) its signal flow graph.

To determine the stability region of the interconnected control system, the bounded-input, bounded output stability theorem is applied to characteristic polynomial of the interconnected control system. Thus, all the zeros of $P(s)$ must reside in the open left-half plane (LHP) to ensure the stability of the interconnected control system.

As the gains of three control loops must be considered to obtain the stability region of the interconnected system based on (3.15), the range of controller gains that result in the stability of the interconnected control system cannot be identified independent of each other, and it is not possible to obtain a simple and closed-form representation of the stability region of the interconnected system in terms of the individual stabilizing controller gains. To overcome this problem, the transfer function of (3.15) is re-arranged as

$$\begin{aligned} P(s) = (1 - G_{\theta q}G_{q\theta}) - \frac{N_{dq}}{D_d}\Big[&(G_{qd} + G_{q\theta}G_{\theta d}) \\ &+ \frac{N_{d\theta}}{N_{dq}}(G_{\theta d} + G_{\theta q}G_{qd})\Big] = (1 - G_{\theta q}G_{q\theta})\times \\ &(1 - \underbrace{\frac{N_{dq}}{D_d}}_{G_{dq}} \underbrace{\frac{(G_{qd} + G_{q\theta}G_{\theta d}) + \frac{N_{d\theta}}{N_{dq}}(G_{\theta d} + G_{\theta q}G_{qd})}{1 - G_{\theta q}G_{q\theta}}}_{\triangle(s)}, \end{aligned} \tag{3.16}$$

where $G_{dq} = \frac{N_{dq}}{D_d}$ and $G_{d\theta} = \frac{N_{d\theta}}{D_d}$ are irreducible transfer functions with an identical denominator D_d as they are associated with the same control loop. Using (3.16), the stability region of the interconnected control system of the VSC is determined by solving for the zeros of

$$\bar{P}(s) = 1 - \triangle(s)G_{dq}, \tag{3.17}$$

(3.17) is a new formulation of VSC stability, in which $\triangle(s)$ only depends on the transfer functions associated with the q-axis control loop (G_{qd} and $G_{q\theta}$) and PLL ($G_{\theta d}$ and $G_{\theta q}$) as $\frac{N_{d\theta}}{N_{dq}}$ =-$\frac{a_1(Ls+R)}{a_{21}+(Ls+R)a_{22}}$, and a_1, a_{21}, and a_{22} are related to the system operating point and are independent of the control gains. Thus, $\triangle(s)$ is considered as a multiplicative uncertainty applied to the stable transfer function $M(s) = G_{dq}(s)$, Fig. 3.4. The small-gain theorem is used next to determine the range of controller gains that ensures the stability of M-$\triangle$ connection of Fig. 3.4.

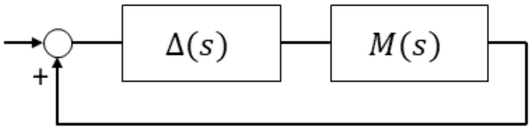

Figure 3.4: The closed-loop block diagram associated with (3.17).

Based on the small-gain theorem [96], for the M-$\triangle$ feedback connection of Fig. 3.4, with $M \in RH_\infty$ and $\gamma > 0$, the interconnected system is stable for all $\triangle \in RH_\infty$ with

$$||\triangle(s)||_\infty < \gamma^{-1} \quad if\ \ and\ \ only\ \ if \quad ||M(s)||_\infty < \gamma, \tag{3.18}$$

where RH_∞ is the set of all proper and real rational **stable** transfer functions, and the infinity norm of $\triangle(s)$ is given by $||\triangle(s)||_\infty = \max_{w} \triangle(jw)$ [33].

Considering that the d-axis control loop is individually stabilized, $M(s) \in RH_\infty$. The stability of $\triangle(s)$ depends on the stability of the interconnection of PLL and the q-axis control loop. With stable $M(s)$ and $\triangle(s)$, the stability of the interconnected system depends on the upper-bound of H_∞ norms. The interconnected system stability is guaranteed for $||\triangle(s)||_\infty < \gamma_\Delta$ and $||M(s)||_\infty < \gamma_M$ if $\gamma_M < \gamma_\Delta^{-1}$. γ_M is adjusted by the d-axis controller gains, and γ_Δ depends on the controller gains of the q-axis control loop and PLL. It should be noted that (3.18) is not applicable in case $G_{\theta q} = 1$ and $G_{q\theta} = 1$ as this would result in the instability of Δ and (3.18) requires stable M and Δ before the interconnection.”

To obtain γ_Δ and γ_M:

1. Find the stabilizing range of controller gains for individual d-axis loop, q-axis loop, and PLL.

2. Using the stabilizing range of controller gains, generate a 2-dimensional grid of controller gains associated with the d-axis loop and a 4-dimensional grid of controller gains associated with the q-axis loop and PLL. Then, $||M(s)||_\infty$ is calculated for all the points in the 2-dimensional grid and $||\Delta(s)||_\infty$ is calculated for each point in the 4-dimensional grid. γ_M and γ_Δ are the largest H_∞ norms associated with each grid.

3. According to γ_M and γ_Δ and (3.18), determine the range of the controller gains associated with the d-axis loop, q-axis loop, and PLL such that $\gamma_M < \gamma_\Delta^{-1}$.

Any controller gain within these ranges stabilizes the interconnected control system of the VSC. Thus, the interactions among the control loops, which are not initially considered in the individual controllers' design, will not destabilize the interconnected control system of the VSC.

3.3.2 Impact of interactions on the VSC transient response

In an interconnected control system, the transient response of the individually designed control loops might be affected by interactions among the control loops. Considering the interconnection of the control loops, the external inputs behave as disturbances in the d-axis and q-axis control loops and may disrupt their transient response. Fig. 3.5 is obtained from Fig. 3.2 and shows how the output of each individual control loop is affected by the external inputs (disturbances) and its set-point. The corresponding transfer functions of Fig. 3.5 are given in the Appendix.

To measure the most severe impact of interactions on the VSC transient response, the following indices based on the infinity norm of the transfer functions from the external inputs to the output of the d-axis and q-axis control loops are defined.

$$\begin{aligned} In_{dq} &= ||G_{\tilde{y}_d,\tilde{u}_q}(s)||_\infty, \quad In_{d\theta} = ||G_{\tilde{y}_d,\tilde{\theta}_{ps}}(s)||_\infty, \\ In_{qd} &= ||G_{\tilde{y}_q,\tilde{u}_d}(s)||_\infty, \quad In_{q\theta} = ||G_{\tilde{y}_q,\tilde{\theta}_{ps}}(s)||_\infty. \end{aligned} \tag{3.19}$$

In_{dq} and $In_{d\theta}$, respectively, correspond to the maximum impact of the q-axis control loop and PLL on the d-axis control loop output. Similarly, In_{qd} and $In_{q\theta}$ are, respectively, associated with the maximum impact of the d-axis control loop and PLL on the q-axis control loop output. The smaller the indices in (3.19) are, the lower the impact of interactions

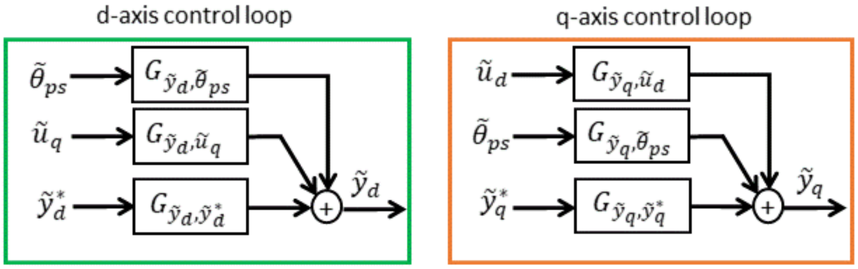

Figure 3.5: A simple schematic of the VSC control system for transient response and set-point tracking analysis.

on the transient response of each control loop is. In particular, near-zero indices correspond to similar transient responses of the corresponding individual and interconnected control loops.

3.3.3 Impact of interactions on the VSC set-point tracking

To evaluate the impact of interactions on the set-point tracking capability of each control loop, the closed-loop transfer functions from the set-points of the d-axis and q-axis control loops ($\tilde{y}_d^*$ and $\tilde{y}_q^*$) to their outputs ($\tilde{y}_q$ and $\tilde{y}_d$) are derived. Using the block diagrams of Fig. 3.5,

$$\tilde{y}_d = G_{\tilde{y}_d,\tilde{y}_d^*}\tilde{y}_d^* + G_{\tilde{y}_d,\tilde{\theta}_{ps}}\tilde{\theta}_{ps} + G_{\tilde{y}_d,\tilde{u}_q}\tilde{u}_q, \tag{3.20}$$

$$\tilde{y}_q = G_{\tilde{y}_q,\tilde{y}_q^*}\tilde{y}_q^* + G_{\tilde{y}_q,\tilde{\theta}_{ps}}\tilde{\theta}_{ps} + G_{\tilde{y}_q,\tilde{u}_d}\tilde{u}_d. \tag{3.21}$$

Using Fig. 3.3, $\tilde{\theta}_{ps} = G_{\theta d}\tilde{u}_d + G_{\theta q}\tilde{u}_q$, and substituting $\tilde{\theta}_{ps}$ into (3.20)-(3.21) results in

$$\underbrace{\begin{bmatrix}\tilde{y}_d\\ \tilde{y}_q\end{bmatrix}}_{Y} = \underbrace{\begin{bmatrix}G_{\tilde{y}_d,\tilde{\theta}_{ps}}G_{\theta d} & G_{\tilde{y}_d,\tilde{\theta}_{ps}}G_{\theta q} + G_{\tilde{y}_d,\tilde{u}_q}\\ G_{\tilde{y}_q,\tilde{\theta}_{ps}}G_{\theta d} + G_{\tilde{y}_q,\tilde{u}_d} & G_{\tilde{y}_q,\tilde{\theta}_{ps}}G_{\theta q}\end{bmatrix}}_{G_{yu}(s)}\begin{bmatrix}\tilde{u}_d\\ \tilde{u}_q\end{bmatrix} + \underbrace{\begin{bmatrix}G_{\tilde{y}_d,\tilde{y}_d^*} & 0\\ 0 & G_{\tilde{y}_q,\tilde{y}_q^*}\end{bmatrix}}_{G^*(s)}\underbrace{\begin{bmatrix}\tilde{y}_d^*\\ \tilde{y}_q^*\end{bmatrix}}_{Y^*}. \tag{3.22}$$

Considering (3.1)-(3.1),

$$\begin{bmatrix}\tilde{u}_d\\ \tilde{u}_q\end{bmatrix} = \underbrace{\begin{bmatrix}K^d(s) & 0\\ 0 & K^q(s)\end{bmatrix}}_{K(s)}\begin{bmatrix}\tilde{y}_d^* - \tilde{y}_d\\ \tilde{y}_q^* - \tilde{y}_q\end{bmatrix}, \tag{3.23}$$

where

$$K^x(s) = \frac{(K_p^{in,x} + \frac{K_I^{in,x}}{s})(K_p^{o,x} + \frac{K_I^{o,x}}{s})}{1 + (K_p^{in,x} + \frac{K_I^{in,x}}{s})(\frac{1}{Ls+R})} \quad x \in \{d, q\}. \tag{3.24}$$

Substituting $\tilde{u}_d$ and $\tilde{u}_q$ from (3.23) into (3.22) results in

$$Y = G_{yu}(s)K(s)(Y^* - Y) + G^*(s)Y^*, \tag{3.25}$$

$$Y = \underbrace{(I + G_{yu}(s)K(s))^{-1}[G_{yu}(s)K(s) + G^*(s)]}_{G_{cl}(s)} Y^*. \tag{3.26}$$

Since $K(s)$ has a pole at the origin, and $G_{yu}(s)$ has no zero at the origin, $G_{cl}(0) = I_{2\times 2}$, where I is the identity matrix. Therefore, the DC gain of the transfer function matrix from the set-points to the control outputs is equal to the identity matrix irrespective of the controller gains and the converter control mode. Therefore, in a stable VSC, the steady-state response of the d-axis and q-axis control loops only depends on the set-point of the individual control loops. In other words, the interactions among the control loops do not impact the set-point tracking of the d-axis and q-axis control loops.

3.4 Simulation Results

The model of a point-to-point VSC-HVDC is built in SIMULINK. The rated parameters of the system are: $P = 100$ MW, $V_{dc} = 400$ KV, $V_s = 230$ kV, $C_{dc} = 300$ μF, $R_{dc} = 14$ Ω, L_{dc}=1.1936 H, and L=0.0725 H. The converter model used in the test system can be found in [4]. It should be noted that all controller gains presented in this section are in per-unit. Since the control loop interactions in one single VSC are studied, the converter at the other end of the HVDC link behaves as a constant load to the converter understudy.

3.4.1 Model validation

To validate the small-signal model of the VSC used in this chapter, the nonlinear model of the VSC and the small-signal model of the system shown in Fig. 3.2 are compared against each other. The nonlinear electromagnetic transient (EMT) model, as well as the nonlinear averaged and small-signal models of the VSC, are built in PSCAD/EMTDC and SIMULINK software environments, respectively. Figs. 3.6-3.7 shows the time-domain responses of the model to a 10% change in the DC voltage set-point. he required transfer

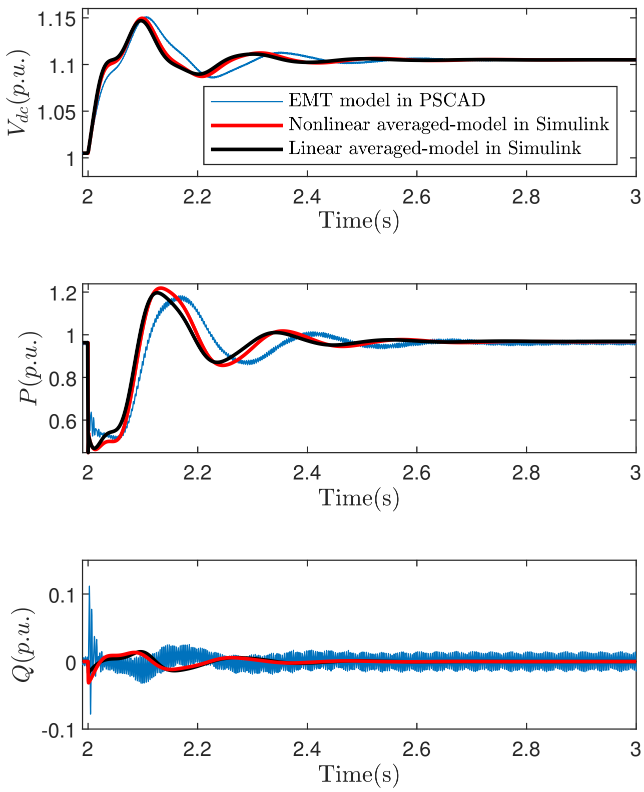

Figure 3.6: Time domain responses for model validation.

functions are given in the following. It is worth mentioning that the harmonic content in EMT waveforms in Figs. 3.6-3.7 has a frequency of about 310 Hz, which is the fifth harmonic.

$$M(s) = G_{dq} = \frac{[a_{21} + (Ls+R)a_{22}]K^{o,d}(s)K^{in,d}(s)}{a_3a_4[(Ls+R) + K^{in,d}(s)] + [a_6(Ls+R) + a_5]K^{o,d}(s)K^{in,d}(s)},$$

$$G_{d\theta} = \frac{-a_1(Ls+R)K^{o,d}(s)K^{in,d}(s)}{a_3a_4[(Ls+R) + K^{in,d}(s)] + [a_6(Ls+R) + a_5]K^{o,d}(s)K^{in,d}(s)},$$

$$G_{\tilde{y}_d,\tilde{u}_q}(s) = \frac{-[a_{21} + (Ls+R)a_{22}]}{a_3a_4[(Ls+R) + K^{in,d}(s)] + [a_6(Ls+R) + a_5]K^{o,d}(s)K^{in,d}(s)},$$

$$G_{\tilde{y}_d,\tilde{\theta}_{ps}}(s) = \frac{a_1(Ls+R)}{a_3a_4[(Ls+R) + K^{in,d}(s)] + [a_6(Ls+R) + a_5]K^{o,d}(s)K^{in,d}(s)},$$

$$G_{\tilde{y}_d,\tilde{y}_d^*}(s) = \frac{-a_0 a_6 (Ls+R) K^{o,d}(s) K^{in,d}(s)}{a_3 a_4 [(Ls+R) + K^{in,d}(s)] + [a_6(Ls+R) + a_5] K^{o,d}(s) K^{in,d}(s)} \ ,$$

$$G_{\tilde{y}_q,\tilde{u}_d}(s) = \frac{[a_{81} + (Ls+R) a_{82}]}{(Ls+R) + K^{in,q}(s) + (a_{10}(Ls+R) + a_9) K^{o,q}(s) K^{in,q}(s)} \ ,$$

$$G_{\tilde{y}_q,\tilde{\theta}_{ps}}(s) = \frac{a_7 (Ls+R)}{(Ls+R) + K^{in,q}(s) + (a_{10}(Ls+R) + a_9) K^{o,q}(s) K^{in,q}(s)} \ ,$$

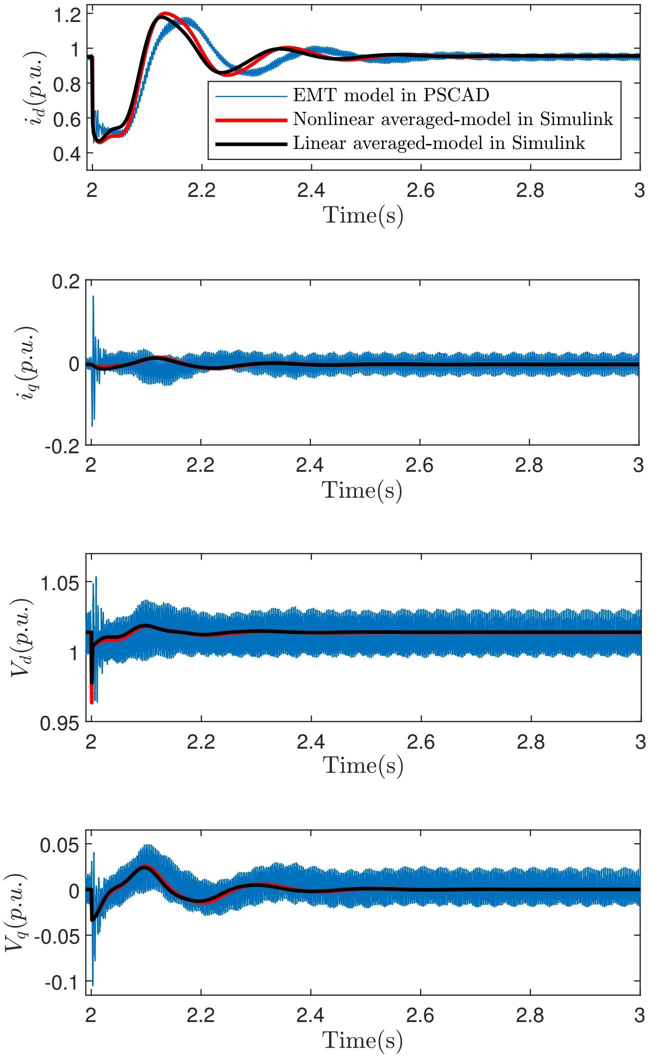

Figure 3.7: Time domain responses for model validation.

$$G_{\tilde{y}_q,\tilde{y}_q^*}(s) = \frac{a_{10}(Ls+R)K^{o,q}(s)K^{in,q}(s)}{(Ls+R)+K^{in,q}(s)+(a_{10}(Ls+R)+a_9)K^{o,q}(s)K^{in,q}(s)} ,$$

$$G_{q\theta} = \frac{-a_7(Ls+R)K^{o,q}(s)K^{in,q}(s)}{(Ls+R)+K^{in,q}(s)+(a_{10}(Ls+R)+a_9)K^{o,q}(s)K^{in,q}(s)} ,$$

$$G_{qd} = \frac{-[a_{81}+(Ls+R)a_{82}]K^{o,q}(s)K^{in,q}(s)}{(Ls+R)+K^{in,q}(s)+(a_{10}(Ls+R)+a_9)K^{o,q}(s)K^{in,q}(s)} ,$$

$$G_{\theta d} = \frac{\omega L_s}{Ls+R}\ \frac{K^{pll}(s)}{s+K^{pll}(s)V_s cos\theta_{ps_0}} ,$$

$$G_{\theta q} = \frac{R_s}{Ls+R}\ \frac{K^{pll}(s)}{s+K^{pll}(s)V_s cos\theta_{ps_0}} .$$

3.4.2 Impact of interactions on system stability

To study the impact of interactions on the VSC stability, the stability regions of the individual control loops are compared against those of the interconnected control system. In Figs. 3.8-3.12, the stability regions of individual and interconnected control loops are represented by the red and blue dots, respectively.

The stability region of the interconnected control system is derived by determining the controller gains that result in the zeros of (3.15) to be in the open LHP. To achieve this, the stabilizing controller gains of the d-axis (q-axis) control loop are determined while the controller gains of PLL and the q-axis (d-axis) control loop are set at constant values. The constant values of the controller gains are solely selected to demonstrate the impact of interactions on the stability region of control loops, and the stability regions need to be re-plotted for another set of constant controller gains. The selected constant controller gains are $K_p^{pll} = 10$, $K_I^{pll} = 580$, $K_p^{o,d}$=2.5, $K_I^{o,d}$=170, $K_p^{o,q}$(AVCL)=-9, $K_I^{o,q}$(AVCL)=-50, $K_p^{o,q}$(RPCL)=-0.1, and $K_I^{o,q}$(RPCL)=-30. Except for RPCL proportional gain, the same constant controller gains are selected under different SCRs to better demonstrate the impact of SCR on the VSC stability. It should be noted that the presented stability regions shaded in blue do not show the complete stability region of the interconnected control system, because they are obtained by fixing two other sets of control parameters. That is the reason some of the stability regions are not in the form of a convex region.

Fig. 3.8 shows the stability regions of the individual and interconnected control system for a strong AC grid with SCR=5 under various control modes. Figs. 3.8a and 3.8c, respectively, show the stability regions of the d-axis and the q-axis control loops for the

DC voltage and reactive power control modes. Figs. 3.8b and 3.8d are associated with the stability regions of DVCL and AVCL. Based on Fig. 3.8, the stability regions of the individual and interconnected control loops in a strong AC grid are identical. Fig. 3.9 is the counterpart of Fig. 3.8 for a weak AC grid with SCR=1.5. Fig. 3.9 shows a significant shrinkage in the stability region of the interconnected control loop for a low SCR. Fig. 3.10 is plotted for the same operating point and controller gains as those of Fig. 3.9, but with $K_p^{pll} = 40$, resulting in an acceptable transient response of PLL. Comparing Figs. 3.9 and 3.10 signifies the strong impact of PLL on the stability of VSCs connected to weak AC systems.

The stability region of the d-axis and the q-axis control loops under active power control mode for SCR=5 and SCR=1.5 are depicted in Figs. 3.11 and 3.12, respectively. In Figs. 3.11a and 3.12a, $K_p^{o,q} = -0.32$ and $K_p^{o,q} = -0.14$, respectively, which correspond to the boundary of the stability region of the individual q-axis control loop (RPCL) in Figs. 3.8c and 3.9c. The rest of the constant controller gains are the same as those discussed for Figs. 3.8 and 3.9. The comparison of Fig. 3.8 against Fig. 3.9 and Fig. 3.11 against Fig. 3.12

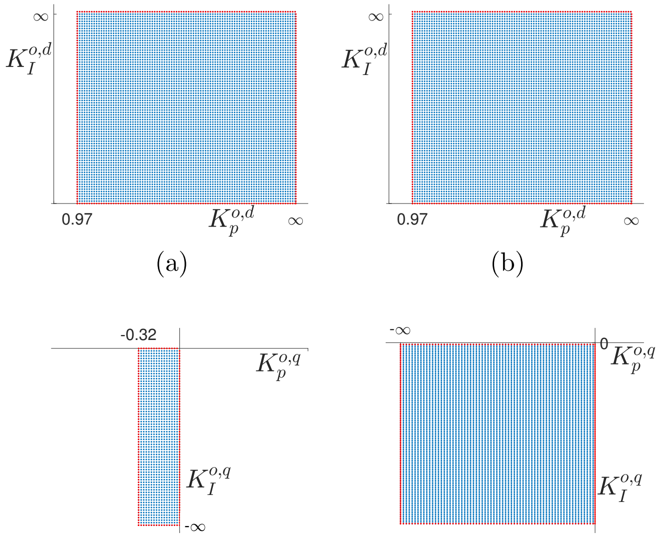

(a) (b)

(c) (d)

Figure 3.8: The stability region of the d-axis and the q-axis control loops for SCR=5 under (a), (c): the DC voltage/reactive power control mode and (b), (d): the DC voltage/AC voltage control mode.

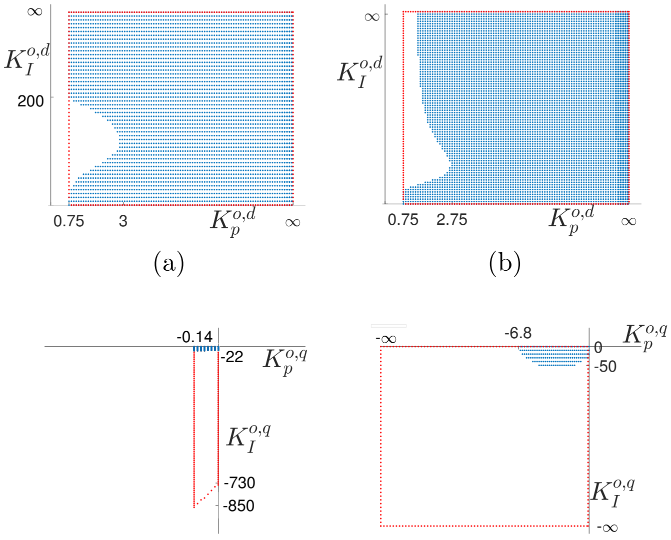

(a) (b)

(c) (d)

Figure 3.9: The stability region of the d-axis and the q-axis control loops for SCR=1.5 under (a), (c): the DC voltage/reactive power control mode and (b), (d): the DC voltage/AC voltage control mode.

shows a large shrinkage in the stability regions of the interconnected control loops under low SCRs. At high SCRs, the stability regions of the interconnected control loops are not affected by the interactions.

Although the stability of the VSC interconnected control system can be evaluated using (3.15), it will result in a stability region depending on six controller gains. Such a stability criterion is hard to be evaluated and be used for the design of the interconnected control system. Therefore, (3.18) is used to determine a subset of the stability region that guarantees the stability of the VSC and depends on a lower number of controller gains. To find this subset, the upper-bound of $||\triangle(s)||_\infty$, γ_Δ, should be determined. Table 3.2 provides γ_Δ corresponding to a selected subset of the complete stability region of the individual PLL and the q-axis control loop as based on (3.17), $\triangle(s)$ depends on those controller gains. Since the lower SCRs result in shrinkage in the stability regions of the control loops, Figs. 3.8-3.10, smaller subsets of the individual stability regions need to be selected for low SCRs. A wider range of controller gains in Table 3.2 may increase γ_Δ, which will later decrease the stabilizing range of d-axis controller gains.

After finding γ_Δ, the upper-bound of $||M(s)||_\infty$, denoted by γ_M, is determined. Since $M(s)$ only depends on the controller gains $K_p^{o,d}$ and $K_I^{o,d}$, γ_M is calculated for the range of $K_{p,min}^{o,d} < K_p^{o,d} < \infty$ and $0 < K_I^{o,d} < \infty$. Fig. 3.13 shows γ_M against $K_{p,min}^{o,d}$ for two SCRs.

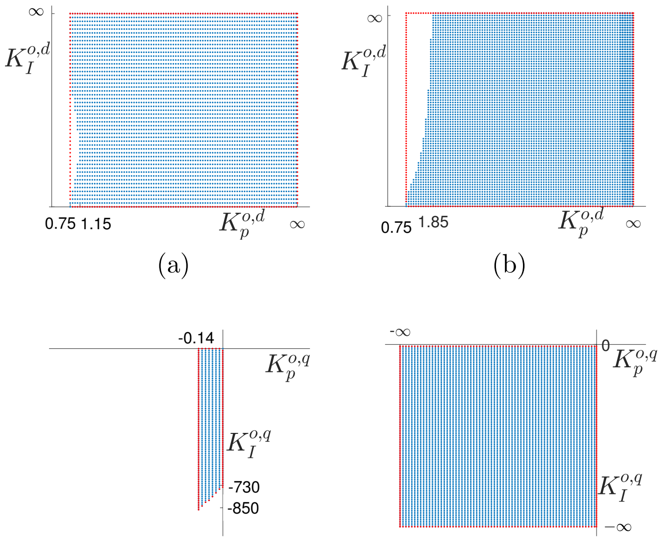

(a) (b)

(c) (d)

Figure 3.10: The stability region of the d-axis and the q-axis control loops for SCR=1.5 and $K_p^{pll} = 40$ under (a), (c): the DC voltage/reactive power control mode and (b), (d): the DC voltage/AC voltage control mode.

Table 3.2: The upper-bound of $||\triangle(s)||_\infty$.

SCR	Case No.	Controller Gains			γ_Δ
		q-axis control loop		PLL	
5	1	RPCL	$-0.32 \leq K_p^{o,q} < 0$ $-\infty < K_I^{o,q} < 0$	$10 \leq K_p^{pll} < 600$ $100 \leq K_I^{pll} < 1500$	0.8344
	2	AVCL	$K_p^{o,q} = 0$ $-\infty < K_I^{o,q} < 0$		0.8179
1.5	3	RPCL	$-0.12 \leq K_p^{o,q} < 0$ $-100 \leq K_I^{o,q} < 0$		1.5668
	4	AVCL	$K_p^{o,q} = 0$ $-700 < K_I^{o,q} < 0$		1.6250

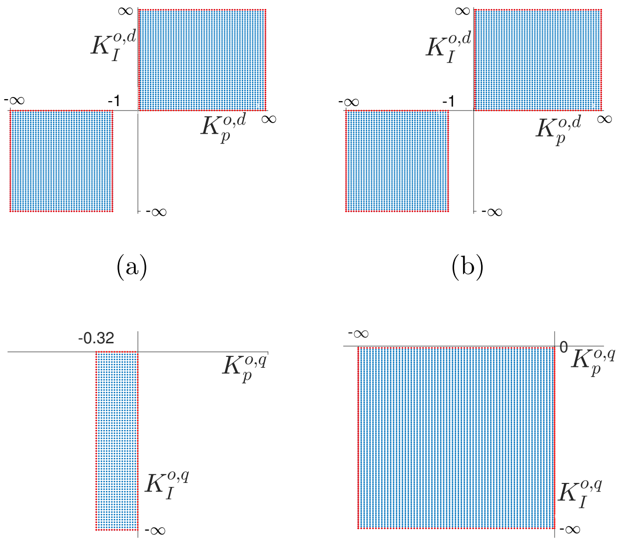

(a) (b)

(c) (d)

Figure 3.11: The stability region of the d-axis and the q-axis control loops for SCR=5 under (a), (c): the active power/reactive power control mode and (b), (d): the active power/AC voltage control mode.

The range of the d-axis controller gains that guarantees the interconnected control system stability is determined by selecting $K_{p,min}^{o,d}$ values from Fig. 3.13 that are associated with $\gamma_M < \gamma_\Delta^{-1}$. Such a range of the d-axis controller gains is presented in Table 3.3 for the two d-axis control modes. These ranges of the d-axis controller gains along with the provided ranges of controller gains for the q-axis control loop and PLL in each Case No. in Table 3.2 constitute a subset of the controller gains that stabilize the interconnected control system of the VSC. It should be noted that the provided range of the controller gains corresponds to the complete range of viable parameters that stabilize the interconnected control system. The range of the parameters can be limited based on the required transient response specifications of the system.

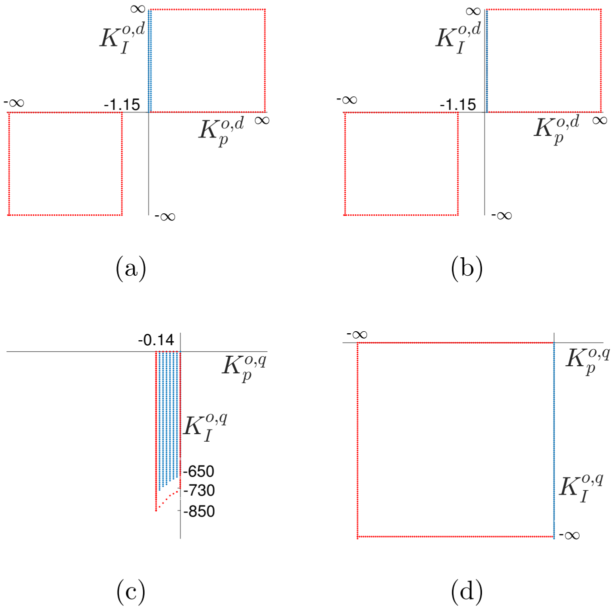

Figure 3.12: The stability region of the d-axis and the q-axis control loops for SCR=1.5 under (a), (c): the active power/reactive power control mode and (b), (d): the active power/AC voltage control mode.

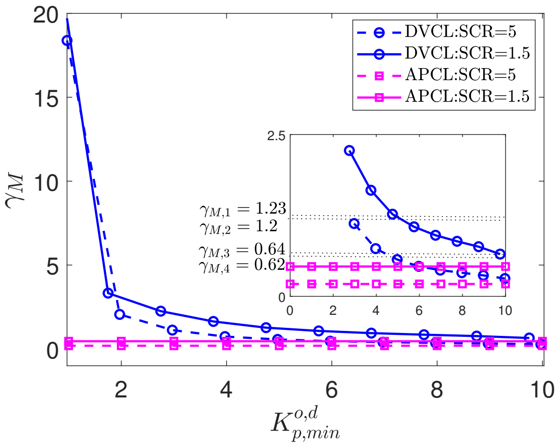

Figure 3.13: The upper-bound of $||M(s)||_\infty$.

3.4.3 Impact of interactions on the transient response and the set-point tracking capability of the VSC

To study the impact of interactions on the transient response of the VSC, the indices of (3.19) as well as time-domain simulations are utilized, Figs. 3.14-3.15. Regarding the impact of interactions on the transient response of the d-axis control loop, Figs. 3.14a and 3.14b show In_{dq} and $In_{d\theta}$ against SCR. The indices are small even for low SCRs, which shows that the impact of PLL and the q-axis control loop on the transient response of the d-axis control loop is small.

Figs. 3.14c and 3.14d illustrate the impact of interactions on the transient response of the q-axis control loop. In Fig. 3.14c, In_{qd} associated with AVCL is larger than one for all SCRs, which indicates that disturbances applied to the d-axis loop will affect AVCL output significantly. Similarly, any disturbances applied to PLL will significantly affect the transient response of RPCL output, Fig. 3.14d. The comparison of Fig. 3.14c against Fig. 3.14d shows that the transient response of AVCL is mostly affected by its interaction with the d-axis control loop rather than PLL, while the transient response of RPCL is more impacted by the interaction with PLL rather than the d-axis control loop.

Moreover, all indices in Figs. 3.14a-3.14d decrease as the SCR increases, indicating that the impact of interactions on the transient response of the VSC becomes less severe when the AC system becomes stronger. The comparison of Figs. 3.14a and 3.14b against Figs. 3.14c and 3.14d reveals that the transient response of the q-axis control loops is more affected by the interactions due to the larger q-axis indices (In_{qd} and $In_{q\theta}$).

Fig. 3.15 shows the time-domain response of the individual and interconnected control loops for two different SCRs. To be able to compare the transient response of individual control loops with that of the interconnected control loops, a 10% increase is applied to the set-point of d-axis (q-axis) control loop. At the same time, to study the impact of interactions and changes in the other control loops on the transient response of the d-axis (q-axis) control loop, the set-point of the q-axis (d-axis) control loop or the input voltage

Table 3.3: The range of the d-axis control loop gains to ensure the overall system stability.

	Case No.			
Control Loop	1	2	3	4
DVCL	$K_p^{o,d} \geq 3.2$ $K_I^{o,d} > 0$	$K_p^{o,d} \geq 2.9$ $K_I^{o,d} > 0$	$K_p^{o,d} \geq 9.8$ $K_I^{o,d} > 0$	$K_p^{o,d} \geq 10$ $K_I^{o,d} > 0$
APCL	$K_p^{o,d} > 0,\ K_I^{o,d} > 0$			

of PLL is increased by 10%. According to Figs. 3.15a-3.15d, the transient response of the individual and interconnected d-axis control loops are almost similar at various SCRs. These observations confirm the small In_{dq} and $In_{d\theta}$ in Figs. 3.14a and 3.14b. On the other hand, based on Figs. 3.15e-3.15h, the transient responses of the q-axis control loops at low SCRs are significantly affected by changes in the d-axis control loop and PLL as the response of the individual and interconnected loops deviate from each other. The reactive power is highly affected by disturbances in PLL, Fig. 3.15f. Moreover, the AC voltage is highly affected by disturbances in the d-axis control loop, Fig. 3.15g. The time-domain studies of Figs. 3.15e-3.15h verify In_{qd} and $In_{q\theta}$ in Figs. 3.14c and 3.14d.

Figs. 3.15a, 3.15c, 3.15e, and 3.15g can also be used to study the impact of interactions on the set-point tracking capability of the VSC. In Figs. 3.15a and 3.15c, when the set-point of the q-axis loop is changed, the d-axis output tracks its own set-point. Similarly, the change in the set-point of the d-axis loop does not impact the steady-state value of the

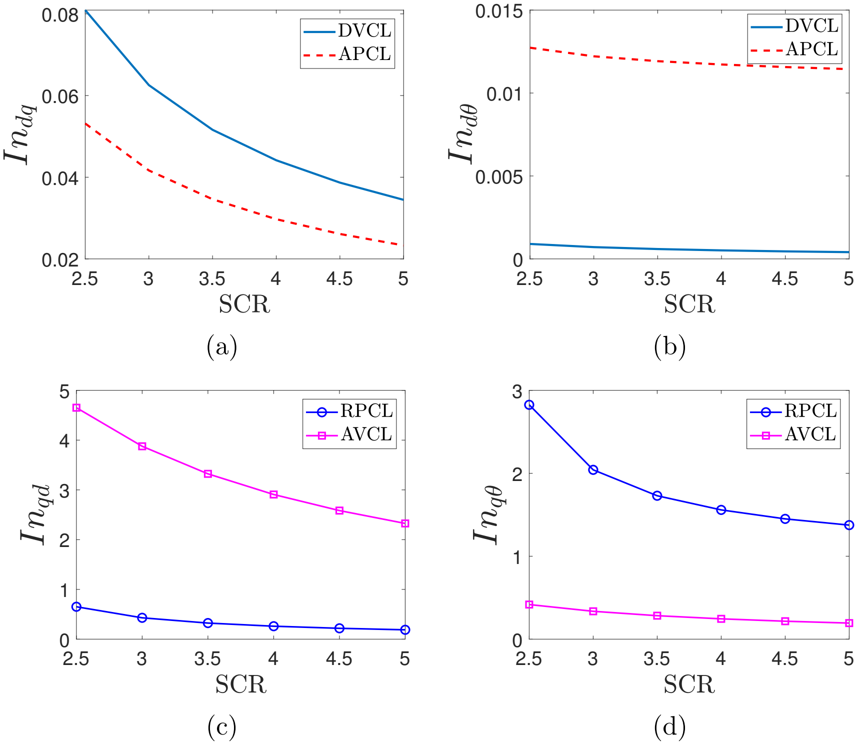

Figure 3.14: The impact of interactions on the transient response of the VSC: (a) In_{dq}, (b) $In_{d\theta}$, (c) In_{qd}, and (d) $In_{q\theta}$.

q-axis outputs in Figs. 3.15e and 3.15g. This observation confirms the analysis of Section 3.3.3 based on the DC gain of the matrix transfer function.

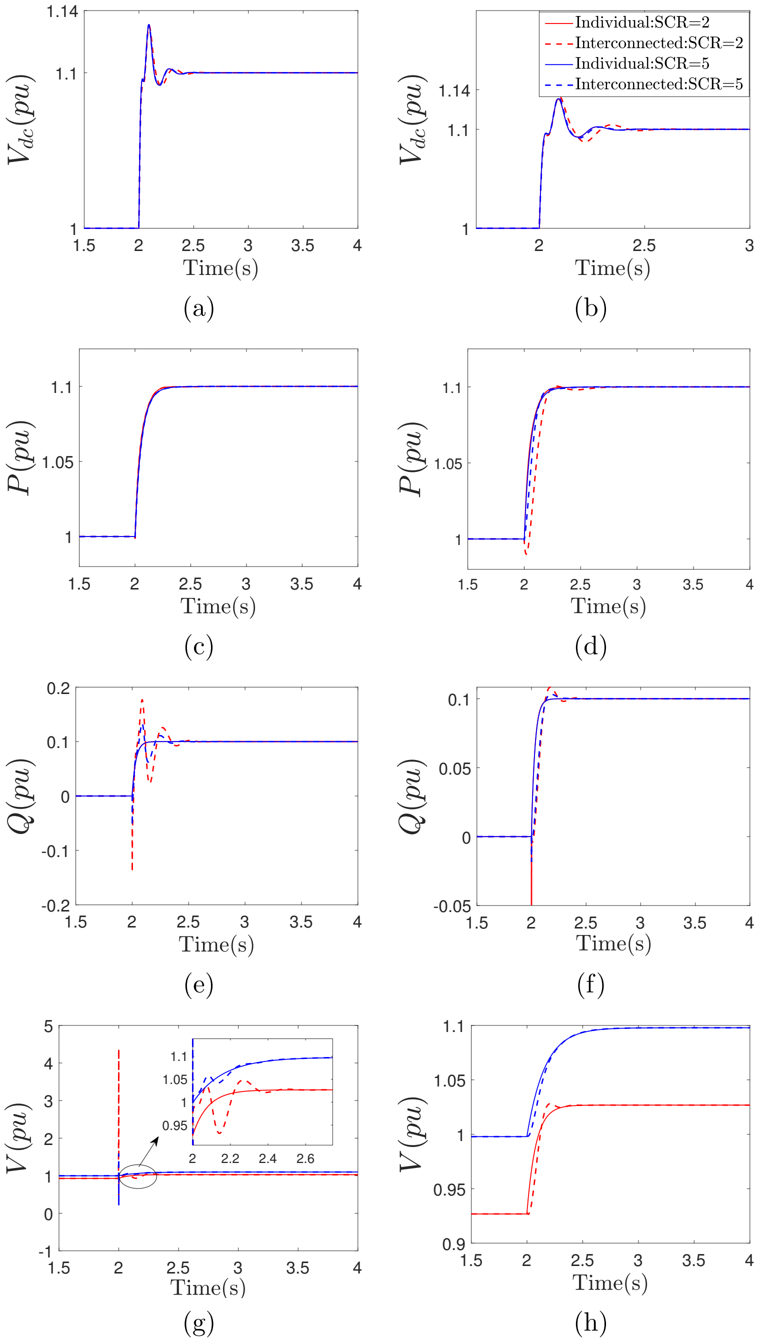

(a) (b)

(c) (d)

(e) (f)

(g) (h)

Figure 3.15: Transient response of the individual and interconnected control loops: (a) and (c) to a 10% increase in the set-point of the q-axis loop; (e) and (g) to a 10% increase in the set-point of the d-axis loop; and (b), (d), (f), and (h) to a 10% increase in the PLL input (V_q).

3.5 Conclusion

This chapter investigated the interactions among the control loops of VSCs from an individual design perspective in three aspects of stability, transient response, and set-point tracking capability of a VSC. The impact of interactions on stability was studied by observing whether a shrinkage occurs in the stability regions of the individual control loops when they operate simultaneously. It is concluded that the control loop interactions significantly affect the stability region of the loops in the interconnected control scheme when the AC system is weak. A new formulation of the VSC stability criterion was also presented, and the small-gain theorem was used to determine a range of stabilizing individual controller gains that ensures the stability of VSC. Furthermore, new indices were introduced to determine the impact of control loop interactions on the transient response of VSCs. According to the studies, the transient response of the d-axis control loops is not impacted by the interactions even for low SCRs, whereas that of the q-axis control loops is significantly impacted by the interactions. Thus, the d-axis control loop can be designed separately, but its impact has to be considered in the design of the q-axis control loop. The results are validated by time-domain simulations. Moreover, using the DC gain of certain transfer functions, it is proved that the control loop interactions do not affect the steady-state response of the VSC.

Chapter 4

DC Side External Control Loop Interactions

4.1 Introduction

The growing need for affordable and clean energy has resulted in various alterations in power grids. One example is the formation of multi-terminal direct current (MTDC) systems, which enables power transmission over long distances and the integration of renewable energy sources within the grid. In an MTDC system, the direct current (DC) system is connected to the alternating current (AC) system via several voltage-sourced converters (VSCs) [78]. The trend toward an increased number of converters in MTDC systems has turned AC-MTDC system stability into a compelling topic due to the interactions among the converters.

In AC- MTDC systems, if converter controllers are designed individually, the interactive system modes stemming from the dynamic couplings among the converters and the DC system components may result in the instability of the interconnected system (INTSYS). In this chapter, using available core models in the literature, a comparative study has been done and suitable individual system (INDSYS) models are selected to enable designing converter controllers independent of those of the adjacent converters. Proper selection of INDSYS models by including the dynamics of certain components of the converters' DC side would lead to a close matching between the dynamics of the interconnected AC-MTDC system and INDSYS models. The selected INDSYS models have the following specifications: I) the superimposed eigenvalue locus of these models is close to the eigenvalue locus of the INTSYS, and II) these models do not include the internal dynamics of adjacent converters. The first specification guarantees a close matching between the dynamic response of the converters operating individually and when connected to other converters. The second specification enables the individual design of converter controllers without any need to access the entire INTSYS model or the internal dynamics of adjacent converters.

The developed method simplifies the control design of large-scale INTSYSs as the control design is performed for several small subsystems rather than a single large INTSYS. Both master-slave and droop control modes are analyzed, and specific individual models are proposed for each mode. Using eigenvalue, sensitivity, and participation factor analyses, it is demonstrated that the selected INDSYS models meet the two necessary specifications that were discussed above and thus are appropriate choices for individual control design.

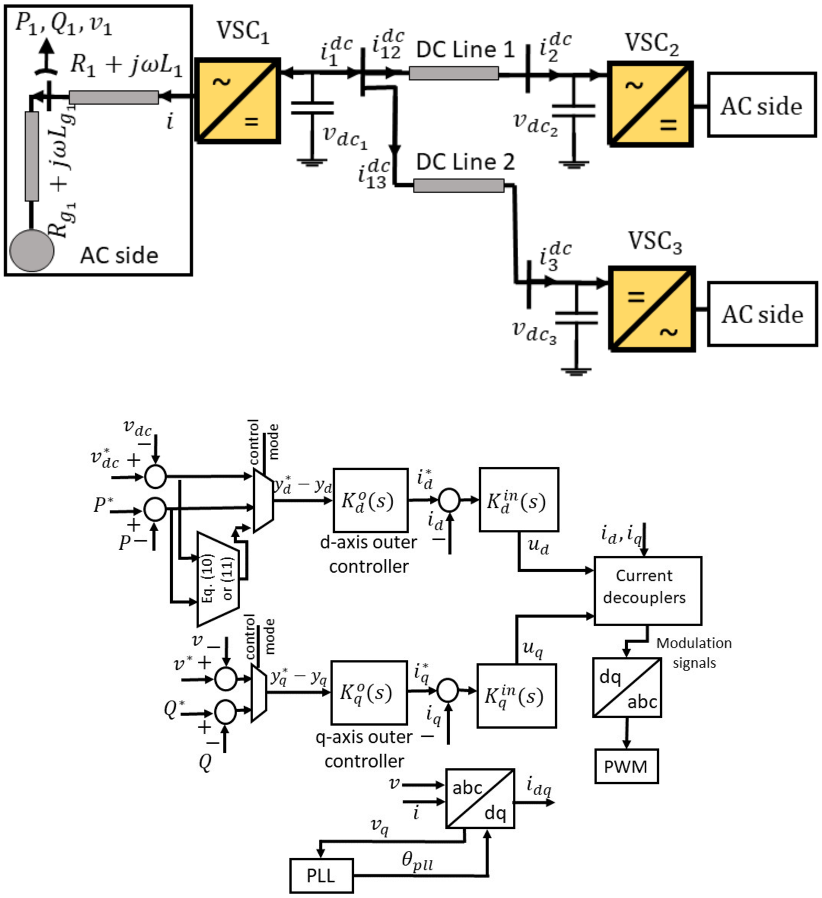

Figure 4.1: (a) Single line diagram of three converters connected to a shared DC system and (b) control system of each converter.

4.2 Interconnected AC-MTDC System Dynamics

Fig. 4.1a shows the schematic diagram of the INTSYS, which includes three VSCs connected to a shared DC system. The system includes only three VSCs (as an example of a system with a larger number of converters) to be able to consider all possible control scenarios and provide a comprehensive analysis. Each converter is connected to the AC grid; modeled by a voltage source behind an impedance; through a filter and is connected to the other converters via DC transmission lines. Because the presented study in this thesis is a small-signal analysis, an RL line model including a resistor and an inductor is considered [53]. The parallel capacitors in the DC lines' model can be included in the capacitors connected to the DC terminal of the converters. Fig. 4.1b shows the control system of the converters in the direct quadrature (dq) rotating frame [86]. The dq indices represent the d- and q-axis components of a variable; i and v, P, Q, respectively refer to the line current at the AC side of the converter, as well as voltage, active power and reactive power at the AC terminal of the converter; and θ_{pll} indicates the reference frame angle provided by the phase-locked loop (PLL).

Considering the dynamics of the dq-components of AC line currents, PLL, active and reactive power in their most general form [86], as well as the DC side dynamics, the small-signal state-space model for the INTSYS is given by

$$\dot{x} = Ax + Bu, \tag{4.1}$$

$$y = Cx + Du, \tag{4.2}$$

where $x = [x_1, x_2, x_3, i_L]^T$, $x_i = [\Delta i_d, \Delta i_q, \Delta\theta_{pll}, x_{pll}, \Delta v_{dc}]^T$ and x_{pll} represents the internal state of PLL, $i_L = [\Delta i_{12}^{dc}, \Delta i_{13}^{dc}]^T$, $y = [\Delta y_1, \Delta y_2, \Delta y_3]^T$, $u = [\Delta u_1, \Delta u_2, \Delta u_3]^T$, and the control signal u_i is generated by the local controller of VSC$_i$ in the dq-axis frame as $u_i = [u_{d_i}, u_{q_i}]^T$ and $y_i = [y_{d_i}, y_{q_i}]^T$. For the converter in DC voltage control mode (DVCM), $y_{d_i} = v_{dc_i}$, for a converter in active power control mode (APCM), $y_{d_i} = P_i$, and for a converter in the droop control mode of operation, y_{d_i} is a combination of active power and DC voltage. y_{q_i} is the q-axis control output, which can be either AC voltage or reactive power, or a combination thereof. The fundamental equations to obtain (4.1)-(4.2) can be found in [86].

According to (4.1)-(4.2), the state variables and control inputs of all VSCs collectively impact INTSYS stability. While the inner current loops are mostly designed based on the AC filter parameters (R_1, L_1) to achieve a fast response for inner control loops [86], tuning the outer control loops for achieving the desired dynamic response depends on the coupling dynamics among the converters, which may not be included in the models used for converter controller design. Fig. 4.2 distinguishes between the control design and the application stages when the full dynamic model of converters is accessible or unavailable. In the control design stage, the design might be based on employing INDSYS models (Fig. 4.2a), which only include the necessary coupling dynamics rather than the full and detailed dynamics of adjacent converters. This approach is referred to as individual control design. In contrast, in the simultaneous design (Fig. 4.2b), the INTSYS model of all the converters and their detailed dynamics are required, which results in a more complex control design procedure. Ultimately, the individually or simultaneously designed controllers will be applied to the interconnected system as shown in Fig. 4.2c. The objective of this chapter is to select suitable INDSYS models to simplify the control design and ensure interconnected system stability.

4.3 INDSYS Models for Converters in Master-Slave Control Mode

Various INDSYS models for converters in the master-slave control mode are presented in this section. The converters are assumed to be in the master-slave control mode, i.e., VSC$_1$ operates in DVCM, and VSC$_2$ and VSC$_3$ operate in APCM.

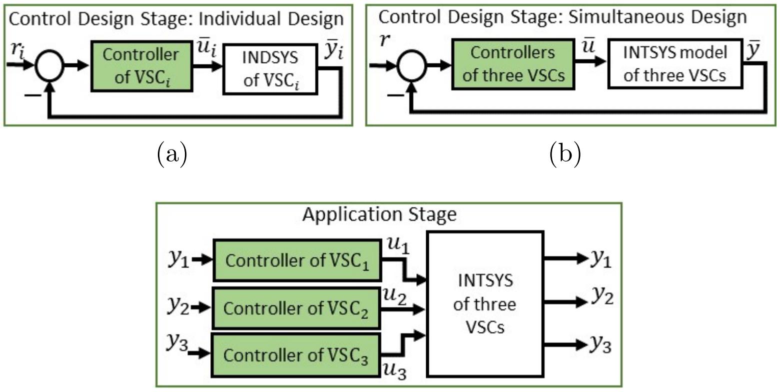

(a) (b)

(c)

Figure 4.2: Employment of the designed controllers in the INTSYS.

4.3.1 Operation in DVCM

Fig. 4.3 shows two possible INDSYS models for VSC_1. In the current source model (model No. 1-DVCM) in Fig. 4.3a, used in [16, 30, 34, 40, 52, 60, 71, 73, 83, 84], the impact of other converters and the DC system on the DC voltage of VSC_1 has not been considered, and the adjacent converters operating in APCM are modeled by constant current sources. On the other hand, model No. 2-DVCM in Fig. 4.3b incorporates the dynamics of DC lines and the operating mode of VSC_2 and VSC_3 in the INDSYS model of VSC_1. It should be also mentioned that in Fig. 4.3b, only the operating mode of adjacent converters–not their internal and detailed dynamics–are considered. Moreover, Fig. 4.3b shows the INDSYS model of VSC_1 only, which is different from [39], [29] where all the converters are replaced by current sources forming the INTSYS model (not the INDSYS model).

Based on the variants shown in Fig. 4.3, Table 4.1 presents the DC side dynamics of various INDSYS models of VSC_1. Considering the internal dynamics of VSC_1 in their most general form by including the PLL and the dq-axis currents [86], as well as the DC side dynamics given in Table 4.1, the small-signal state-space representation of INDSYS model for VSC_1 will be given by

$$\dot{\bar{x}}_1 = \bar{A}_1\bar{x}_1 + \bar{B}_1\bar{u}_1, \tag{4.3}$$

$$\bar{y}_1 = \bar{C}_1\bar{x}_1 + \bar{D}_1\bar{u}_1, \tag{4.4}$$

where $\bar{x}_1 = [\bar{x}_{ac_1}, \bar{x}_{dc}]^T$, $\bar{u}_1 = [\Delta u_{d_1}, \Delta u_{q_1}]^T$, and $\bar{y}_1 = [\Delta v_{dc_1}, \Delta y_{q_1}]^T$. $\bar{x}_{dc}$ is given in Table 4.1 and $\bar{x}_{ac_1} = [\Delta i_d, \Delta i_q, \Delta\theta_{pll}, x_{pll}]^T$. The overbars in (4.3)-(4.4) are used to distinguish

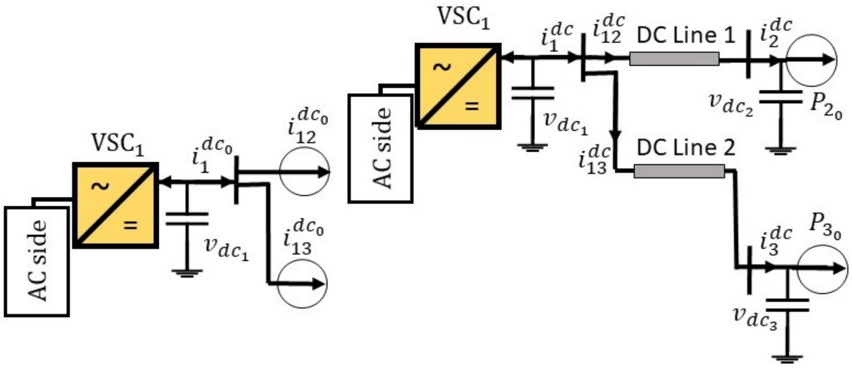

(a) (b)

Figure 4.3: INDSYS model of VSC_1 in DVCM: a) model No. 1-DVCM and b) model No. 2-DVCM.

Table 4.1: The DC side dynamics of the INDSYS models of VSC$_1$ in DVCM.

Model No. 1-DVCM	Model No. 2-DVCM
$\mathrm{C}_1\frac{\mathrm{d}v_{dc_1}}{\mathrm{d}t} = -\underbrace{(i_{12}^{dc_0}+i_{13}^{dc_0})}_{i_1^{dc_0}} - \frac{P_1}{v_{dc_1}}$	$\mathrm{C}_1\frac{\mathrm{d}v_{dc_1}}{\mathrm{d}t} = -\underbrace{(i_{12}^{dc}+i_{13}^{dc})}_{i_1^{dc}} - \frac{P_1}{v_{dc_1}}$ $\mathrm{L}_L\frac{\mathrm{d}i_{12}^{dc}}{\mathrm{d}t} + R_L i_{12}^{dc} = v_{dc_1} - v_{dc_2}$ $\mathrm{L}_L\frac{\mathrm{d}i_{13}^{dc}}{\mathrm{d}t} + R_L i_{13}^{dc} = v_{dc_1} - v_{dc_3}$ $\mathrm{C}_2\frac{\mathrm{d}v_{dc_2}}{\mathrm{d}t} = i_{12}^{dc} - \frac{P_{2_0}}{v_{dc_2}}$ $\mathrm{C}_3\frac{\mathrm{d}v_{dc_3}}{\mathrm{d}t} = i_{13}^{dc} - \frac{P_{3_0}}{v_{dc_3}}$
$\bar{x}_{dc}=\Delta v_{dc_1}$	$\bar{x}_{dc} = [\Delta v_{dc_1},\quad \Delta i_{12}^{dc},\quad \Delta i_{13}^{dc},\quad \Delta v_{dc_2},\quad \Delta v_{dc_3}]^T$

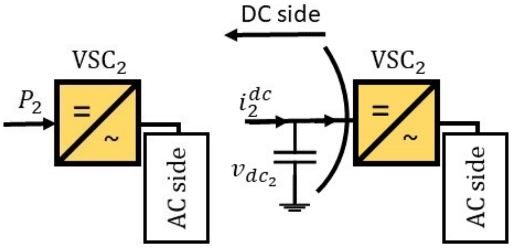

(a) (b)

Figure 4.4: INDSYS model of VSC$_2$ in APCM: a) model No. 1-APCM and b) model No. 2-APCM.

between the INDSYS and INTSYS models. In Table 4.1, the subscript “0” represents the operating point at which the system model is linearized. Based on Table 4.1, two sets of state-space models in the form of (4.3)-(4.4) are obtained for VSC$_1$ and are compared against each other in Section 4.6 to determine the most suitable model.

4.3.2 Operation in APCM

For a converter in APCM, the active power controlled at the AC terminal of the converter is described by

$$P = v_d i_d + v_q i_q, \tag{4.5}$$

which is independent of voltages and currents at the DC side of the converter. After linearizing (4.5), the state-space representation of a converter in APCM given by

$$\dot{\bar{x}}_k = \bar{A}_k \bar{x}_k + \bar{B}_k \bar{u}_k, \tag{4.6}$$

$$\bar{y}_k = \bar{C}_k \bar{x}_k + \bar{D}_k \bar{u}_k; k \in \{2, 3\}, \tag{4.7}$$

where $\bar{y}_k = [\Delta P_k, \Delta y_{q_k}]^T$, $\bar{x}_k = [\Delta i_d, \Delta i_q, \Delta\theta_{pll}, x_{pll}, \Delta v_{dc}]^T$, and the output and state matrices have the following forms:

$$\bar{C}_k = \begin{bmatrix} \times_{2\times4} & 0_{2\times1} \end{bmatrix}, \bar{A}_k = \begin{bmatrix} \times & 0 & 0 & 0 & 0 \\ 0 & \times & 0 & 0 & 0 \\ \times & \times & \times & \times & 0 \\ \times & \times & \times & 0 & 0 \\ \times & \times & \times & 0 & \times \end{bmatrix}, \tag{4.8}$$

where × shows the non-zero elements. The zero entries in (4.8) are created because neither the active power in (4.5) nor the AC voltage/reactive power depends on the DC voltage. Based on (4.8), the DC voltage is an unobservable state when the converter is in APCM. Furthermore, the active power is controlled at the AC side and, thus, is not impacted by the operating mode of other converters. Therefore, it is neither necessary nor beneficial to include the dynamics of the DC terminal voltage in the state-space model of the converter in APCM. Consequently, among the two schematics shown in Fig. 4.4, where Fig. 4.4a ignores the DC side dynamics and Fig. 4.4b includes it, the schematic of Fig. 4.4a will be used as the selected INDSYS model of the converter in APCM. The state-space model of (4.6)-(4.7) is then valid with $\bar{x}_k = [\Delta i_d, \Delta i_q, \Delta\theta_{pll}, x_{pll}]^T$.

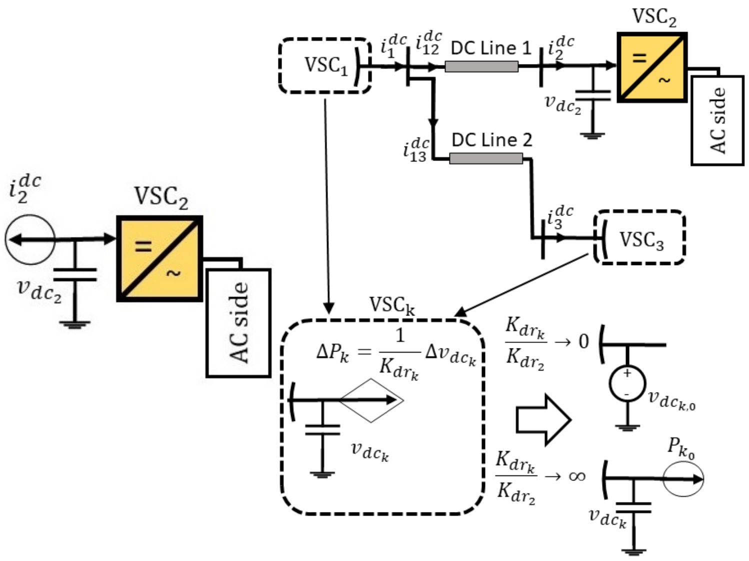

(a) (b)

Figure 4.5: INDSYS model of VSC$_2$ for droop mode of operation: a) model No. 1-Droop and b) model No. 2-Droop.

4.4 INDSYS Model of Converters in Droop Control Mode

The droop control describes a proportional relationship between the active power and DC voltage as

$$\underbrace{P_{k,0} - P_k}_{\Delta P_k} = (\frac{1}{K_{dr_k}})\underbrace{(v_{dc_{k,0}} - v_{dc_k})}_{\Delta v_{dc_k}}. \tag{4.9}$$

Based on (4.9), the control output in the droop control mode is a combination of DC voltage and active power ($y_{d_k} = P_k - \frac{1}{K_{dr_k}} v_{dc_k}$, or $y_{d_k} = v_{dc_k} - K_{dr_k} P_k$), in contrast to the constant DVCM or APCM. Because the DC voltage appears in the control output formulation (y_{d_k}), this converter is impacted by the adjacent converters through their DC voltages. It should be noted that the sign of the droop constant is adjusted in the control system by using a proper sign for controller gains.

Fig. 4.5 shows two INDSYS models for VSC$_2$ when all converters operate in droop control mode. Fig. 4.5a shows the current source model (model No. 1-Droop) that

Table 4.2: The DC side dynamics of two INDSYS models of VSC$_2$ in droop control mode.

Model No. 1-Droop	Model No. 2-Droop
$\mathrm{C}_2\frac{\mathrm{d}v_{dc_2}}{\mathrm{d}t} = -i_2^{dc_0} - \frac{P_2}{v_{dc_2}}$	$\mathrm{C}_2\frac{\mathrm{d}v_{dc_2}}{\mathrm{d}t} = i_{12}^{dc} - \frac{P_2}{v_{dc_2}}$ $\mathrm{L}_L\frac{\mathrm{d}i_{12}^{dc}}{\mathrm{d}t} + R_L i_{12}^{dc} = v_{dc_1} - v_{dc_2}$ $\mathrm{L}_L\frac{\mathrm{d}i_{13}^{dc}}{\mathrm{d}t} + R_L i_{13}^{dc} = v_{dc_1} - v_{dc_3}$ $\mathrm{C}_1\frac{\mathrm{d}v_{dc_1}}{\mathrm{d}t} = -(i_{12}^{dc} + i_{13}^{dc}) - \frac{P_1}{v_{dc_1}}$ $P_1 = P_{1,0} - \frac{1}{K_{dr_1}}(v_{dc_{1,0}} - v_{dc_1})$ $\mathrm{C}_3\frac{\mathrm{d}v_{dc_3}}{\mathrm{d}t} = i_{13}^{dc} - \frac{P_3}{v_{dc_3}}$ $P_3 = P_{3,0} - \frac{1}{K_{dr_3}}(v_{dc_{3,0}} - v_{dc_3})$

has been used in the literature [14, 16]. Neither the dynamics of the DC line nor the operating mode of adjacent converters are considered in this model. On the other hand, Fig. 4.5b shows the INDSYS model No. 2-Droop for VSC$_2$, in which the dynamics of DC transmission lines and the capacitor in the other converters are considered. The operating modes of adjacent converters are incorporated into this model using a voltage-dependent power source (according to (4.9)). This INDSYS model is different from that in [39] where the converters are replaced by current sources to form the INTSYS model.

Considering Fig. 4.5b, if K_{dr_k} is very small compared to K_{dr_2} ($\frac{K_{dr_k}}{K_{dr_2}} \to 0$), VSC$_k$ will experience less deviation in its DC voltage with changes in the active power. On the other hand, if K_{dr_k} is very large compared to K_{dr_2} ($\frac{K_{dr_k}}{K_{dr_2}} \to \infty$), VSC$_k$ will experience less deviation in its active power with changes in the DC voltage. Therefore, it can be concluded that if $\frac{K_{dr_k}}{K_{dr_2}}$ is very small, VSC$_k$ can be considered as a voltage source in the INDSYS model of VSC$_2$. If $\frac{K_{dr_k}}{K_{dr_2}}$ is sufficiently large, VSC$_k$ can be represented by a constant active power source in the INDSYS model of VSC$_2$. In the general case, where the droop constants of converters are neither small nor large compared to one another, the adjacent converters operating in droop control mode will be represented by a capacitor and a voltage-dependent power source as shown in the box in Fig. 4.5b. Table 4.2 shows the DC side dynamics of INDSYS models shown in Fig. 4.5.

If at least one of the converters is in APCM rather than in droop control mode, the INDSYS model of this converter will be model No. 1-APCM shown in Fig. 4.4a. The impact of this converter on the INDSYS model of other converters that operate in droop control mode will be similar to Fig. 4.5b, where the droop constant of the converter in APCM is very large compared to the droop constants of other converters.

4.5 Validation of the INDSYS Models

Prior to the comparative study, model validation is performed for model No. 1-DVCM and model No. 2-DVCM proposed in Fig. 4.3 and model No. 2-Droop in Fig. 4.5. In this process, the nonlinear electromagnetic transient (EMT) model, built in PSCAD environment, the averaged nonlinear model, built in SIMULINK, and the small-signal (linear) model are compared against each other. The required system and control parameters are given in Table 4.3. It should be mentioned that the system model built in PSCAD includes a parallel second order RLC filter with $f_{\text{cut}} = 450$ Hz for filtering the switching harmonics. Figs. 4.6-4.7 show the response of the models to a 10% change applied to the DC voltage at t=*8* s. The model validation confirms that the small-signal models used in this chapter are accurate.

Table 4.3: Parameters of the test system [5]

Quantity	Value	Description
P	200 MW	Active power
V_{dc}	400 KV	DC voltage
V_s	230 KV	AC grid RMS voltage
f	60	Frequency
L	0.0291 H	Filter inductance
R	0.005 Ω	Filter and switches on-state resistance
C_{dc}	300 μ F	DC side capacitance
τ	2 ms	Inner current loop time constant
K_p^{pll}, K_I^{pll}	30,460	Proportional and integral gains of PLL

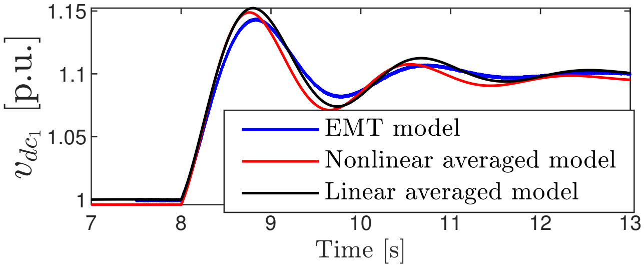

(a) INTSYS

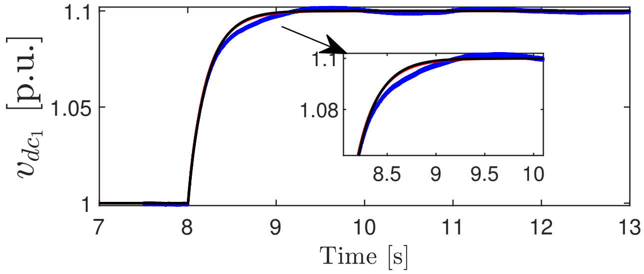

(b) Model No. 1-DVCM

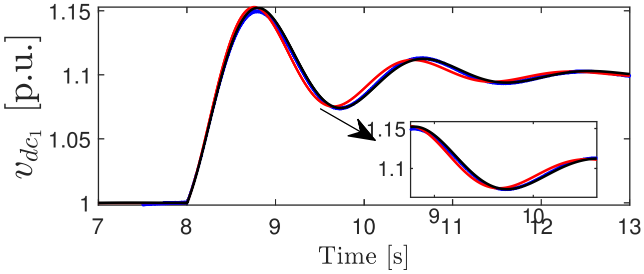

(c) Model No. 2-DVCM

Figure 4.6: Validation of the models in the master-slave mode of operation: time-domain response of the EMT, nonlinear averaged, and linear averaged models to a 10% change in the DC voltage at t=8s.

4.6 Comparative Study of INDSYS Models for the Master-Slave Mode of Operation

According to Section 4.3.2, for a VSC in APCM, the INDSYS model No. 1-APCM, while for a converter in DVCM, there are two potential INDSYS models shown in Fig. 4.3. In this

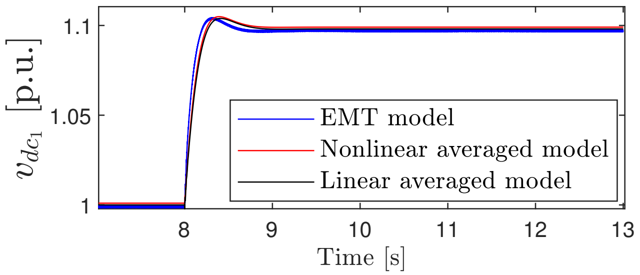

Figure 4.7: Validation of model No. 2-Droop in the droop control mode: time-domain response of the EMT, nonlinear averaged, and linear averaged models to a 10% change in the DC voltage at t=8s.

section, the suitable model among these two models will be identified using the eigenvalue, participation factor, and sensitivity analyses. These analyses are used to determine how the stability and dynamic performance of INTSYS are impacted by the type of INDSYS model.

4.6.1 Eigenvalue analysis

Fig. 4.8 compares INDSYS model No. 1-DVCM and No. 2-DVCM of VSC$_1$ shown in Fig. 4.3 in terms of the closeness of their eigenvalue locus to that of the INTSYS model under changing VSC$_1$ controller parameters. While the focus is on choosing the suitable INDSYS model for VSC$_1$ (in the DVCM), the eigenvalues associated with the INDSYS model of all three VSCs are plotted to show the correspondence between the eigenvalues of the INTSYS and the aggregate of the INDSYS models. Fig. 4.8a and Fig. 4.8b respectively show the impact of changing the integral gain (K_{I_1}) and the proportional gain (K_{p_1}) of the DC voltage controller on the eigenvalue locus of the INDSYS model of VSC$_1$ and INTSYS. The q-axis controller of VSC$_1$ is set to $\frac{16.46}{s}$. According to Fig. 4.8, the eigenvalue locus of INTSYS and INDSYS models do not match for model No. 1-DVCM. However, employing model No. 2-DVCM leads to an exact matching between the eigenvalues of INTSYS and INDSYS models.

Fig. 4.9 is the counterpart of Fig. 4.8 for a low SCR (SCR=1.5) associated with the AC grid connected to VSC$_1$. Similar to Fig. 4.8, Fig. 4.9 also shows a deviation in the eigenvalue locus of INTSYS and that of the INDSYS model No. 1-DVCM. Furthermore, Fig. 4.9 shows that while the INDSYS models are stable, the INTSYS might become unstable with variations of controller parameters. Thus, not only do the eigenvalues of

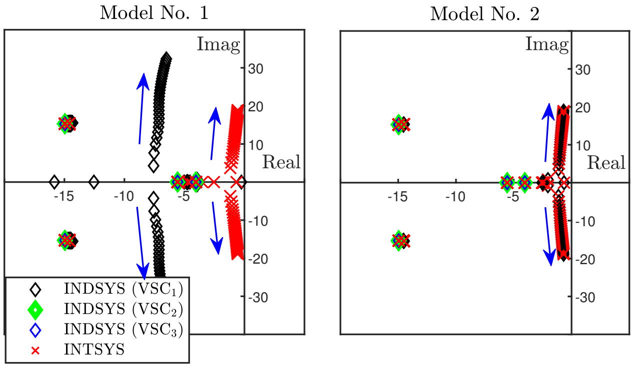

(a) Sweep of K_{I_1}={1;300} and K_{p_1}=2

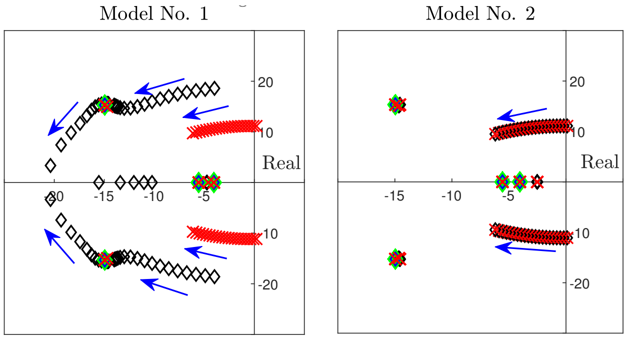

(b) Sweep of K_{p_1}={0.3;10.5} and K_{I_1}=100

Figure 4.8: Eigenvalue locus of INDSYS and INTSYS models for SCR=4 and a sweep of DC voltage controller parameters.

INTSYS deviate from the INDSYS model No. 1-DVCM, but instability occurs in INTSYS for a range of control parameters even though the INDSYS models are stable. Therefore, with these models, no mitigation approach can be taken during the individual design of converter controllers to stabilize the INTSYS as no instability is observed in the INDSYS models. Stabilizing the INTSYS, in this case, would require access to the entire INTSYS model and retuning of the individually designed controllers. Selecting model No. 2-DVCM, however, can solve this issue because whenever the INTSYS is unstable, the INDSYS model is unstable as well. Therefore, the INTSYS can be stabilized via the proper design of individual controllers.

To illustrate the significance of selecting proper models for individual converter controllers' design on the stability of the INTSYS, Fig. 4.10 compares the stability regions of the INTSYS model and INDSYS model of VSC$_1$. According to Fig. 4.10, the allowable

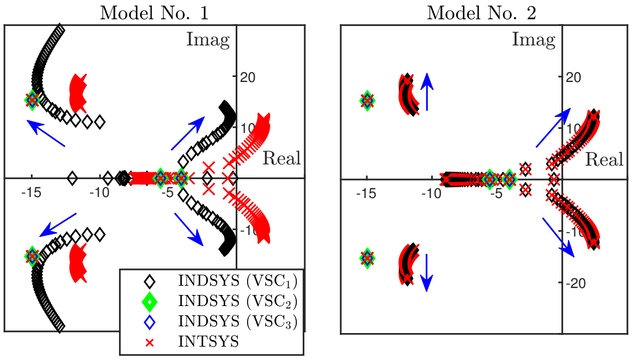

(a) Sweep of K_{I_1}={1;300} and K_{p_1}=2

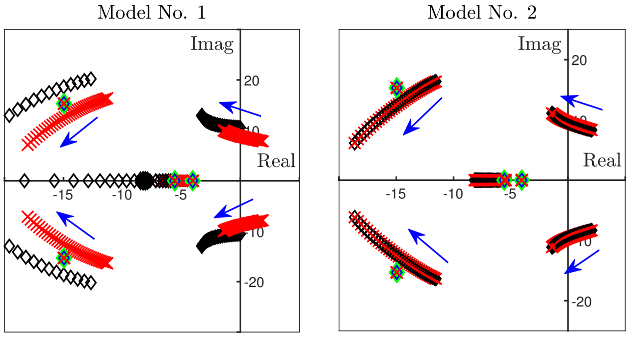

(b) Sweep of K_{p_1}={0.3;18.5} and K_{I_1}=100

Figure 4.9: Eigenvalue locus of INDSYS and INTSYS models for SCR=1.5 and a sweep of DC voltage controller parameters.

range of controller parameters to ensure the INTSYS stability shrinks with the connection of the converters to a shared DC system, and as a result, the INTSYS might lose stability even when VSC$_1$ is stable. However, the stability regions of the INDSYS model of VSC$_1$ and INTSYS model are exactly the same when model No. 2-DVCM is selected for designing the controllers of VSC$_1$.

To verify the conclusion made based on Fig. 4.10, the time-domain response of the INTSYS and INDSYS models to a small disturbance in the DC voltage for two sets of parameters are depicted in Fig. 4.11. The parameters of set 1 (corresponding to the stable region of INTSYS) are $K_{p_1} = 2.5, K_{I_1} = 10$, and the parameters of set 2 (corresponding to the unstable region of INTSYS) are $K_{p_1} = 2.5, K_{I_1} = 20$. Fig. 4.11 shows that all three models are stable for set 1 parameters. However, only INDSYS model No. 1-DVCM is stable for set 2 parameters. This confirms that the stability region of model No. 1-

DVCM is not similar to that of INTSYS, and thus, a controller designed for VSC_1 based on INDSYS model No. 1-DVCM will not stabilize the INTSYS.

4.6.2 Participation factor analysis

To identify the state variables that contribute significantly to the unstable modes of INTSYS in Fig. 4.9 and to determine whether model No. 2-DVCM, which showed the same eigenvalues as that of the INTSYS, includes these state variables, participation factor analysis is used. If model No. 2-DVCM includes the corresponding states, a controller designed based on this model for a converter in DVCM will stabilize the INTSYS.

Fig. 4.12 shows the participation factors of INTSYS state variables in the unstable modes. The state variables of each converter are shown on the horizontal axis, and the vertical axis shows the participation factors. Because Fig. 4.12 is plotted for the sweep of controller parameters of VSC_1, the state variables associated with the outer controller of VSC_1 are also highlighted on the horizontal axis. The sweep of parameters is similar to that in Fig. 4.9. It should be mentioned that the state variables and their order are similar to those in (4.1)-(4.2). Considering Fig. 4.12, the highest participation in the unstable modes is associated with the state variables of VSC_1 (in particular i_{dq_1}, v_{dc_1}, and the state variable associated with VSC_1 d-axis outer controller). The DC voltages of VSC_2 and VSC_3 (states number 11 and 21) also impact the unstable modes. Based on the discussion provided in Section 4.3.2, the DC voltage is not included in the INDSYS model of a converter in APCM. Therefore, to contain all the dynamics causing instability in the INDSYS models, the dynamics of capacitors of the converters in APCM (states number 11 and 21) must

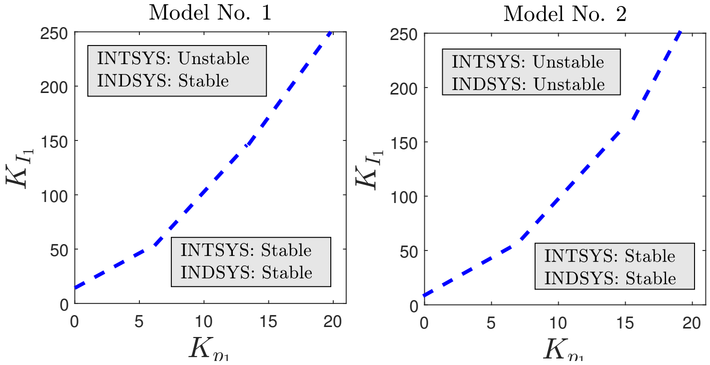

Figure 4.10: Stability region of INTSYS vs. stability region of INDSYS models of VSC_1 (SCR=1.5).

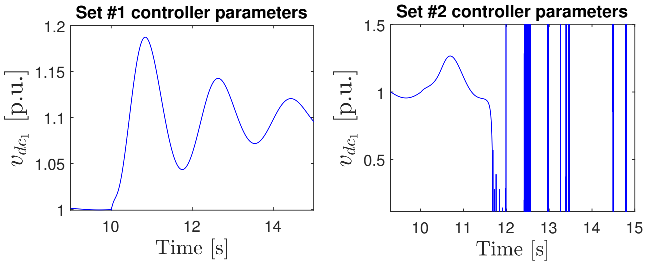

(a) INTSYS

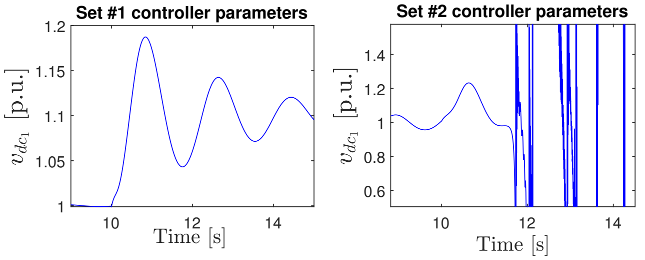

(b) INDSYS model No. 2-DVCM

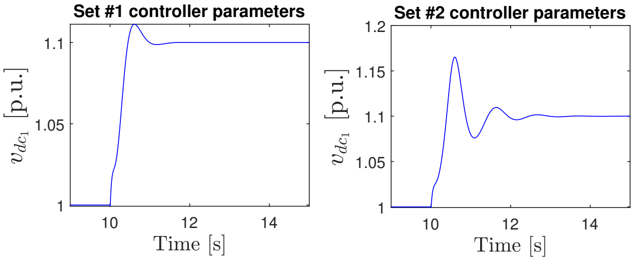

(c) INDSYS model No. 1-DVCM

Figure 4.11: Time-domain response of (a) INTSYS model, (b) INDSYS model No. 2-DVCM, and (c) INDSYS model No. 1-DVCM, to a 10% change in the DC voltage. Controller set 1: $K^o_{d_1} = 2.5 + \frac{10}{s}$, and controller set 2: $K^o_{d_1} = 2.5 + \frac{20}{s}$. $K^o_{q_1} = 0.002 + \frac{11.5}{s}$ for both cases

be considered in the INDSYS model of VSC$_1$, which operates in DVCM. Referring to Fig. 4.3, only INDSYS model No. 2-DVCM includes these necessary state variables.

4.6.3 Sensitivity analysis

According to the eigenvalue and participation factor analyses, model No. 2 for a converter in DVCM provides a close matching between the eigenvalues of the INDSYS and INTSYS

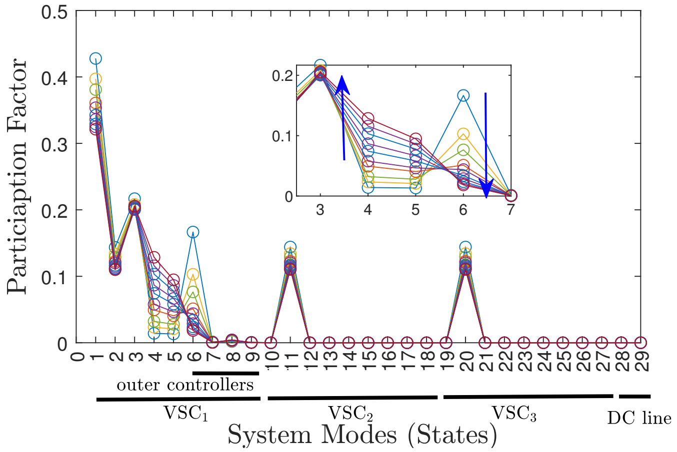

(a) Sweep of K_{I_1}={1;300} and K_{p_1}=2

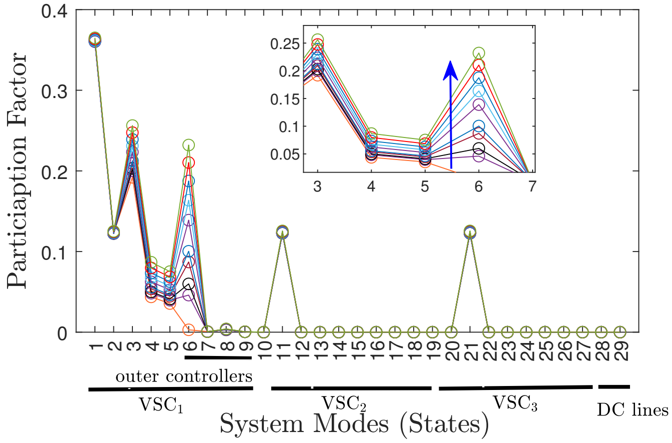

(b) Sweep of K_{p_1}={0.3;18.5} and K_{I_1}=100

Figure 4.12: Participation factors for INTSYS system's unstable modes in Fig. 4.9 with (a) sweep of K_{I_1} and (b) sweep of K_{p_1}.

models and also includes the required state variables that may cause instability. However, there exist discrepancies between the state-space model of INTSYS, given by (4.1)-(4.2), and that of INDSYS, given by (4.3)-(4.4) and (4.6)-(4.7). Fig. 4.13 shows the state-space model of the INTSYS in comparison to those of the INDSYS models. Yellow and green colors respectively correspond to INDSYS models No. 1-DVCM and No. 2-DVCM of VSC$_1$ shown in Fig. 4.3. The state-space representation of INDSYS models only include the elements that are highlighted in their corresponding color.

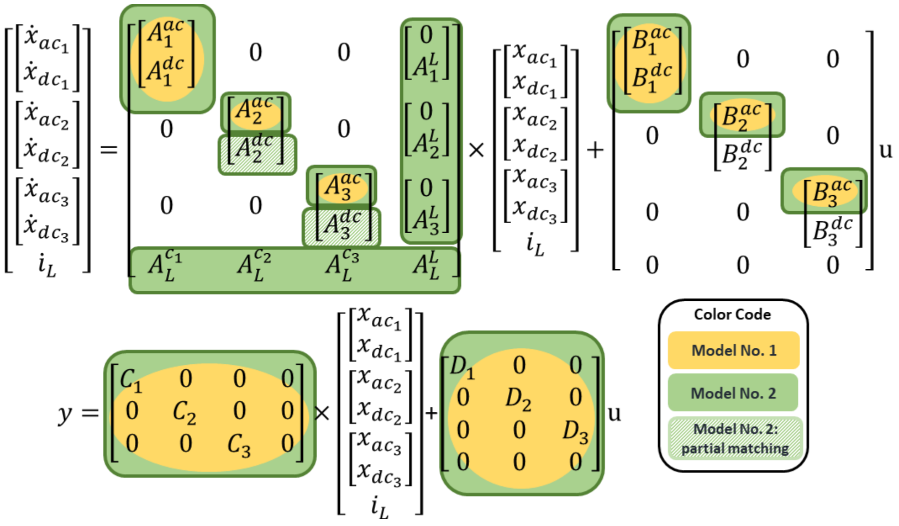

Figure 4.13: The matching level between INTSYS and INDSYS state-space models.

Fig. 4.13 confirms that there is a significant discrepancy between the A matrix of the INTSYS and INDSYS model No. 1-DVCM. Between the two INDSYS models for a converter in DVCM, model No. 2-DVCM (Fig. 4.3b) shows the largest similarity with the INTSYS. Although there is a significant matching between the state-space representation of the INTSYS and INDSYS model No. 2-DVCM, some discrepancies remain between the two models as the internal dynamics of the converters in APCM are ignored in model No. 2-DVCM. These discrepancies, which correspond to the partial matching or no matching between the dynamics of the INTSYS and model No. 2-DVCM are represented by A_2^{dc}, A_3^{dc}, B_2^{dc}, and B_3^{dc} matrices.

To verify whether this mismatch deteriorates the accuracy of INDSYS model No. 2-DVCM, the sensitivity of eigenvalues of the closed-loop system with respect to the elements of A_2^{dc}, B_2^{dc}, A_3^{dc}, and B_3^{dc} matrices in Fig. 4.13 is computed as

$$\frac{\partial \lambda_i}{\partial a_{kj}} = \Psi_{ik}\Phi_{ji}, \tag{4.10}$$

where Ψ_{ik} and Φ_{ji} are the elements of the left and right eigenvectors associated with λ_i [49], and a_{kj} corresponds to the elements of the INTSYS state matrix that are associated with A_2^{dc}, B_2^{dc}, A_3^{dc}, and B_3^{dc} (each of VSC$_2$ and VSC$_3$ has five state variables, so a_{kj} has 5 elements per converter). The sensitivity of all the eigenvalues to the elements of matrices corresponding to the mismatches is plotted in Fig. 4.14, where each color represents one eigenvalue. Fig. 4.14 illustrates that the sensitivity of eigenvalues to the elements that do not match between the INTSYS and INDSYS state-space models is very small, showing that their inclusion or exclusion in the models does not considerably impact the eigenvalue locus. Therefore, Fig. 4.3b and Fig. 4.4a provide precise models respectively for a converter in DVCM and for a converter in APCM.

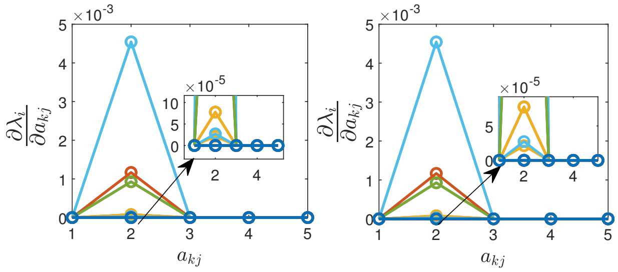

(a) SCR=4

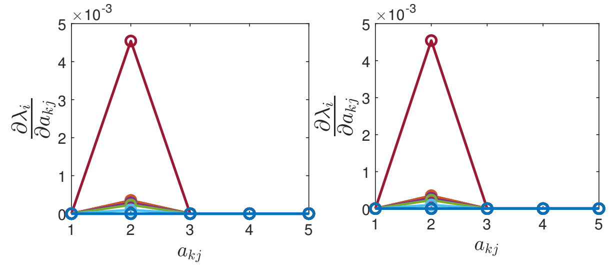

(b) SCR=1.5

Figure 4.14: Sensitivity of eigenvalues with respect to a_{kj}: (on the left: a_{kj} associated with A_2^{dc} and B_2^{dc}, and on the right: a_{kj} associated with A_3^{dc} and B_3^{dc}).

Table 4.4: Set of droop constants.

	Set 1	Set 2	Set 3	Set 4
Droop Constants	$K_{d_1} = 0.1$ $K_{d_2} = 10$ $K_{d_3} = 10$	$K_{d_1} = 10$ $K_{d_2} = 0.1$ $K_{d_3} = 0.1$	$K_{d_1} = 1$ $K_{d_2} = 1$ $K_{d_3} = 1$	$K_{d_1} = 3$ $K_{d_2} = 3$ $K_{d_3} = 3$

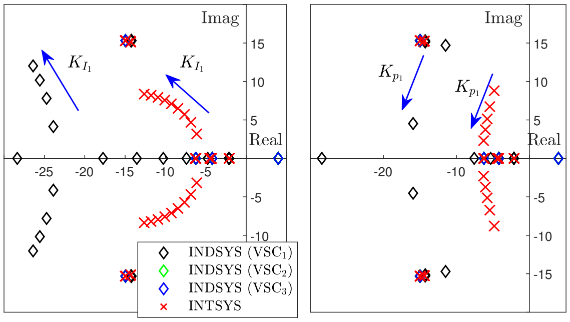

(a) Model No. 1-Droop

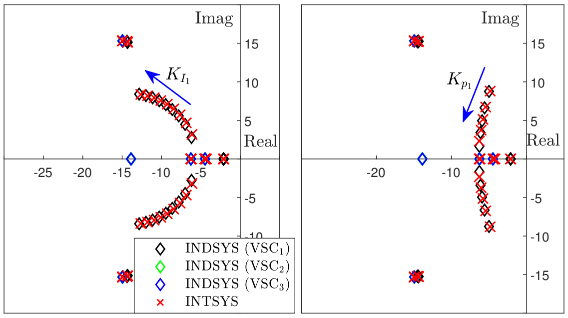

(b) Model No. 2-Droop

Figure 4.15: Eigenvalue locus of INTSYS and INDSYS models for droop set 1 for a) model No. 1 and b) model No. 2, with the sweep of parameters of VSC$_1$: (on the left: K_{p_1}=$\{0.3;2.5\}$ and K_{I_1}=10, and on the right: K_{I_1}=$\{10;50\}$ and K_{p_1}=2), and SCR=4.

4.7 Comparison of INDSYS Models for Converters in Droop Control Mode of Operation

Several droop constants are presented in Table 4.1 and are used to specify which one of the INDSYS models in Fig. 4.5 is a suitable choice for the individual control design of converters.

In set 1, the droop constant of VSC$_1$ is small, while the two other droop constants are large. Therefore, based on the discussion in Section 4.4, in the INDSYS model of VSC$_1$, VSC$_2$ and VSC$_3$ can be considered as active power sources. Likewise, in the INDSYS

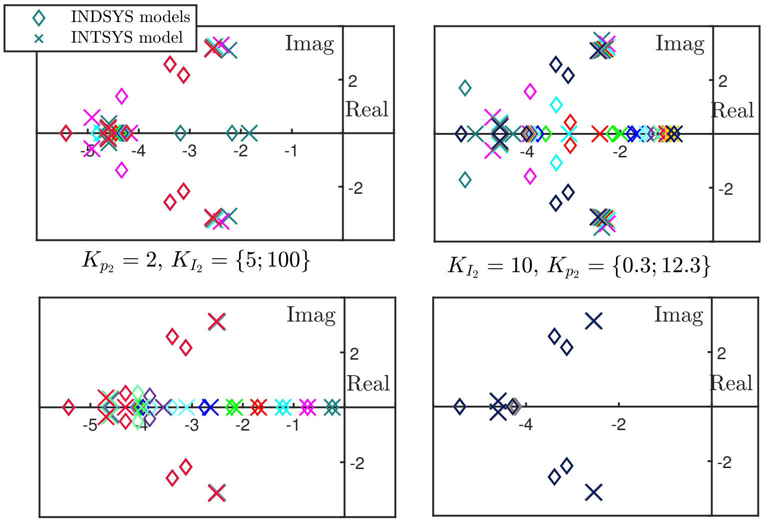

$K_{p_2} = 2,\ K_{I_2} = \{5; 100\}$

$K_{I_2} = 10,\ K_{p_2} = \{0.3; 12.3\}$

$K_{p_2} = 20,\ K_{I_2} = \{5; 100\}$

$K_{I_2} = 100,\ K_{p_2} = \{0.3; 12.3\}$

Figure 4.16: Eigenvalue locus of INTSYS and INDSYS models (model No. 2-Droop) for a sweep of controller parameters for droop set 3.

models of VSC_2 and VSC_3, VSC_1 can be considered as a constant voltage source. Fig. 4.15 shows the eigenvalue locus of INDSYS and INTSYS models for droop set 1. Fig. 4.15a and Fig. 4.15b respectively show the eigenvalue locus for the current source model and model No. 2-Droop. The eigenvalue locus of INTSYS and INDSYS models are similar in Fig. 4.15b, while they are different in Fig. 4.15a, showing that the current source model is not suitable, but the model of Fig. 4.5b contains the necessary coupling dynamics. Similar observations were made for droop set 2. Therefore, for droop sets 3 and 4, only model No. 2-Droop (Fig. 4.5b) will be considered, and its accuracy will be analyzed.

In the third and fourth sets of droop constants in Table 4.1, the droop constants for all the VSCs are the same. Fig. 4.16 shows the eigenvalue locus of the INTSYS model and the INDSYS model No. 2-Droop for droop set 3, where each color is associated with one specific set of control parameters. Based on Fig. 4.16, adjacent to each eigenvalue of the INDSYS there exists an eigenvalue associated with the INTSYS. In some cases, the exact matching between the eigenvalues of INTSYS and INDSYS does not happen, though they remain close to each other. The reason is that model No. 2-Droop does not include the internal dynamics of adjacent VSCs, even though the coupling between the DC voltage and the active power in the droop control mode is incorporated into the INDSYS model. Similar conclusions can be made for droop set 4.

To better compare the eigenvalue locus of INTSYS and INDSYS models, Fig. 4.17 shows the magnitude and the phase angle of dominant eigenvalues of the two models against control parameters of VSC_2 for droop sets 2-4. Due to the symmetry of the eigenvalue locus with respect to the real axis, the phase angles associated with only one of the complex-conjugate oscillatory modes are shown. Figs. 4.17a and c, associated with droop set 2, show a close matching between the magnitude and phase angle of eigenvalues of the INDSYS and INTSYS, confirming the conclusion made based on Fig. 4.15. Figs. 4.17b-c and Figs. 4.17e-f indicate a close matching between the eigenvalue locus of the INDSYS and INTSYS for equal droop constants and confirm the observations based on Fig. 4.16. According to Figs. 4.17c and f, the magnitude and phase angle of eigenvalues of INTSYS and INDSYS models for droop set 4 are closer to each other compared to those depicted in Figs. 4.17b and e for droop set 3. The reason can be explained based on model No. 2-Droop in Fig. 4.5b. When the droop constants become larger, $\frac{1}{K_{dr_k}}$ becomes smaller. As a result, according to (4.9), the adjacent converters that are represented by the voltage-dependent power source in Fig. 4.5b behave comparable to a constant active power source. In such a case, the coupling between the DC voltage and active power of adjacent converters becomes weaker, and the INDSYS models, which do not include the internal dynamics of adjacent converters, provide a closer match to the INTSYS model in terms of dynamic response.

Due to the coupling among the VSCs in the droop mode of operation, the superimposed eigenvalue of INDSYS models may be slightly different from that of the INTSYS model. The INDSYS model might not be an exact duplicate of INTSYS. However, INDSYS stability ensures INTSYS stability as the eigenvalues are in the same neighborhood. It should be noted that the purpose is to exclude the internal dynamics of adjacent VSCs from the INDSYS models, simplify the stability analysis and design the controllers individually while preventing the INTSYS instability. If the internal dynamics of adjacent VSCs are considered in the models, the control system design cannot be decomposed into that of smaller subsystems.

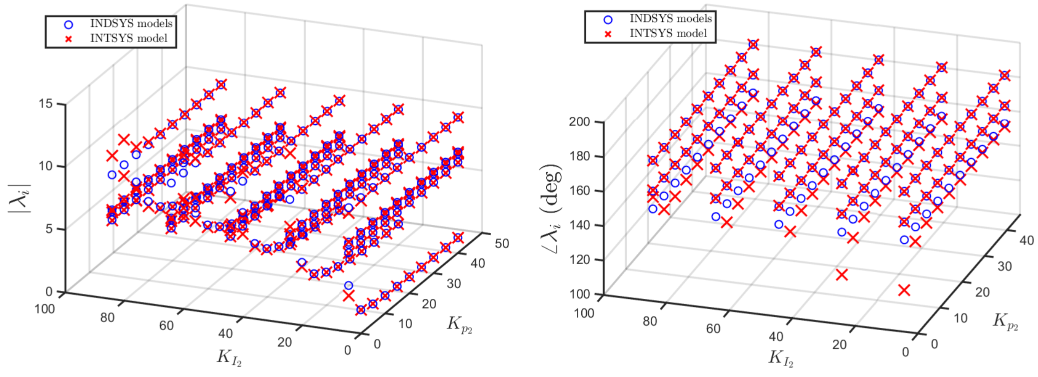

(a) Droop set 2 (b) Droop set 2

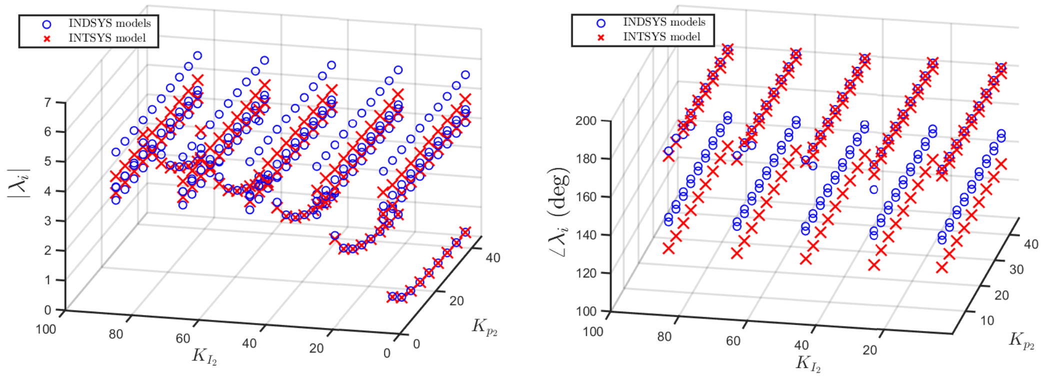

(c) Droop set 3 (d) Droop set 3

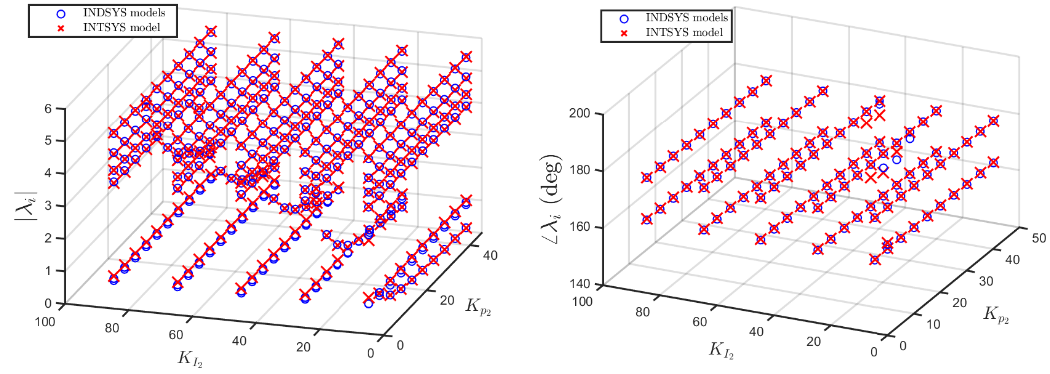

(e) Droop set 4 (f) Droop set 4

Figure 4.17: Magnitude and phase angle of all the eigenvalues close to the imaginary axis against controller parameters for a-b) droop set 2, c-d) droop set 3, and e-f) droop set 4.

4.8 Conclusion

This chapter studied the importance of proper inclusion of DC system components in the system models used for an individual control design of the converters embedded in AC-MTDC systems. The objective was to determine the appropriate system models that capture the necessary coupling dynamics among the converters. A controller that is designed individually based on the appropriate model can be employed in the interconnected system (INTSYS) without causing instability or poorly damped oscillations. The suitable individual system (INDSYS) models were selected such that they did not include the adjacent converters' internal dynamics but included the necessary coupling dynamics to prevent uncontrollable dynamic interactions among converters. Participation factor, sensitivity, and eigenvalue analyses were performed to verify the accuracy of the models.

The studies demonstrated that for a converter in DC voltage control mode (DVCM), the only model that leads to an exact matching between the eigenvalue locus of INTSYS and INDSYS models was the one that included the dynamics of DC transmission lines and the capacitor of the converters in the active power control mode (APCM). For a converter in APCM, including the converter's AC side dynamics in the INDSYS model was sufficient, and including the DC voltage dynamics was not necessary. For the droop control mode of operation, the model that included the DC transmission line and the operating mode of adjacent converters through a voltage-dependent power source led to the best match between INTSYS and INDSYS models. The impact of AC system SCR on INTSYS stability was also discussed. It was shown that for low SCR values, depending on the type of INDSYS model, the individually designed converter controllers may not stabilize the INTSYS. Selecting a suitable INDSYS model for control design, in this case, can provide a close matching between the stability regions of INTSYS and INDSYS models of VSCs.

Chapter 5

AC Side External Control Loop Interactions[1]

5.1 Introduction

Integration of converter-interfaced renewable energy sources (RESs) into the power system and the transfer of power from RESs to remote load centers over high-voltage DC (HVDC) lines may require connecting multiple voltage-sourced converters (VSCs) to a common AC grid. As a result of this connection, control loops of various converters will interact through the AC grid, leading to system instability and an undesirable transient response. In this chapter, the interactions are defined as deviations in the response of converters when they are connected to a shared AC system and when they are isolated. Considering this definition, this chapter achieves two main objectives: i) to identify the set of control modes for which the stability of individual VSCs can ensure the stability of multi-VSC systems and ii) to provide a sufficient stability criterion for designing the converter controllers independently such that the multi-VSC system, in the presence of interactions, is stabilized as well. To do so, a stability formulation is provided that relates the stability of the interconnected multi-VSC system to that of the independent VSCs. Then, μ analysis is used to study whether and under which control modes the independently stabilized VSCs connected to a shared AC system stabilize the multi-VSC system. This set of control modes creates the least disruptive impact on the multi-VSC system's stability. Finally,

---

[1] Ahmadloo, F., Pirooz Azad, S.: Grid interaction of multi-VSC systems for renewable energy integration. IET Renew. Power Gener. 1–12 (2023)

certain recommendations are provided about the design of converters' controllers to reduce the negative impact of interactions on the multi-VSC system's stability.

The main contributions of this chapter are as follows:

- The impact of control modes of converters on external control loop interactions is studied using μ analysis, and the set of control modes causing the highest and lowest interaction levels are identified.
- In contrast to the existing literature, in this chapter, all possible control modes of a grid-following VSC and the full dynamics of inner and outer control loops as well as PLL are considered in the interaction analysis.
- A sufficient stability criterion is proposed to perform an independent design of VSC's controllers that stabilizes the multi-VSC system as well.
- For the set of control modes causing the largest interactions, a joint design for controllers of VSCs is recommended to reduce the negative impacts of interactions on multi-VSC system stability.
- The approach taken in this chapter directly connects the stability of independent VSCs to that of the interconnected multi-VSC system, providing a new perspective to interaction analysis and mitigation. Although μ analysis has already been used in the literature for robust stability analysis, it is used for interaction analysis for the first time in this chapter. This tool is advantageous not only in the control design of multiple VSCs whose simultaneous design is not possible but also when retuning of adjacent converter controllers without impacting the entire system stability is required.

5.2 Modeling of VSCs Connected to a Shared PCC

In this section, the state-space and transfer function models of multiple VSCs connected to a shared PCC are presented in the dq-frame. The state-space model is presented to reveal the mechanism of interactions, and the transfer function model is used in Section 5.3 for interaction analysis. For further clarity, indices d and q refer to the d and q components of a variable, and '$\rightarrow$' and '$\sim$ ' respectively denote the space phasor and the small-signal representation of a variable.

Fig. 5.1a shows the schematic of a multi-VSC system, and Fig. 5.1b shows the control system of each VSC, where the control loops are in the cascaded inner-outer scheme.

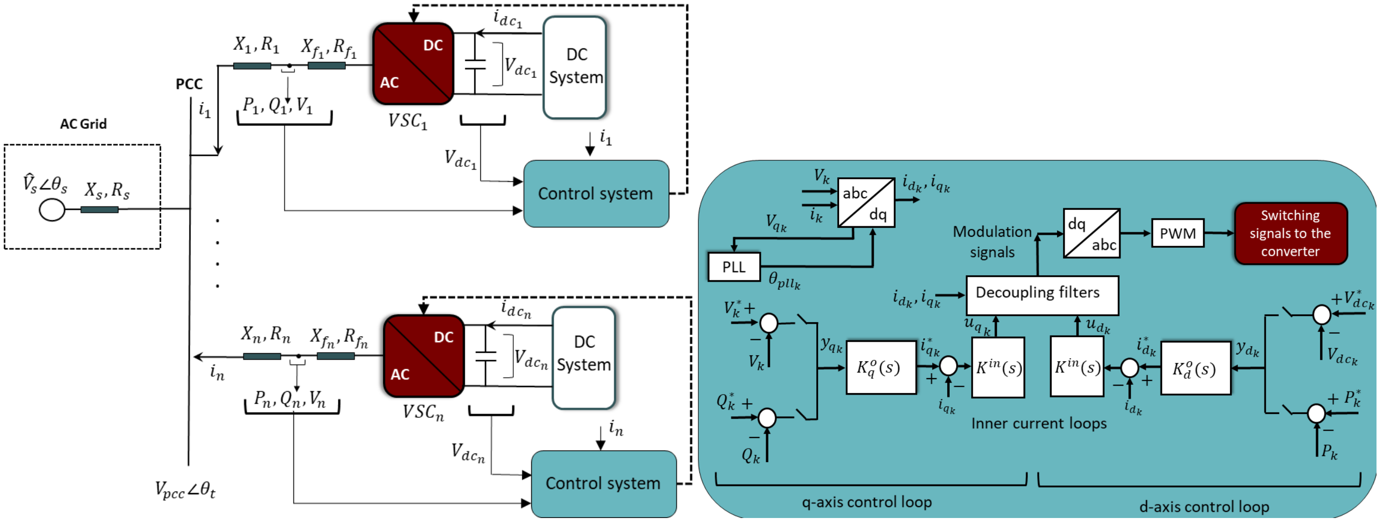

(a) (b)

Figure 5.1: (a) Schematic diagram of multiple VSCs having a connection at the AC side and (b) each VSC's control loops.

Because the focus of this work is control loop interactions, the AC side of each VSC is modeled only as an impedance, and all the elements behind the PCC are modeled by a voltage source behind an impedance [45, 70]. The parameters of the converters, which are needed for numerical illustrations, are given in Table 5.1. Using the space-phasor representation of the current-voltage dynamics at the AC side,

$$L_s\frac{\mathrm{d}(\overrightarrow{i}_1+\ldots+\overrightarrow{i}_n)}{\mathrm{d}t} = -R_s(\overrightarrow{i}_1+\ldots+\overrightarrow{i}_n)+\overrightarrow{V}_{pcc}-\hat{V}_s^{j\theta_s}, \tag{5.1}$$

where $\hat{V}_s$, θ_s, L_s, and R_s are respectively the voltage magnitude, voltage phase, inductance, and resistance of the AC system, $\hat{V}_{pcc}$ is the magnitude of the voltage at the PCC, and i_k is the AC line current of VSC_k given by

$$\overrightarrow{i}_k = (i_{d_k}+ji_{q_k})e^{j\theta_{pll_k}}; \quad k=\{1,2,..n\}, \tag{5.2}$$

where θ_{pll_k} is the reference frame angle provided by the PLL of VSC_k. The dedicated PLL of each VSC aligns its q-axis with the voltage at the corresponding converter terminal (V_k in Fig. 5.1). Combining (5.1)-(5.2) with the voltage-current relationship at the converters' terminals and considering the decoupling filters [86], the dq-components of the voltage at the AC terminal of VSC_k are given by

$$\begin{aligned} V_{d_k} = {} & [R_s + R_k - \frac{X_s + X_k}{X_{f_k}} R_{f_k}] i_{d_k} + \frac{X_s + X_k}{X_{f_k}} u_{d_k} \\ & - [X_k + X_s] i_{q_k} + \hat{V}_s cos\theta_{ps_k} \\ & + \underbrace{\sum_{j=1, j\neq k}^{n} [[(R_s - R_{f_j}\frac{X_s}{X_{f_j}}) i_{d_j} + \frac{X_s}{X_{f_j}} u_{d_j} - X_s i_{q_j}] cos\theta_{p_k p_j}}_{\text{Couplings}} \\ & + \underbrace{[(R_s - R_{f_j}\frac{X_s}{X_{f_j}}) i_{q_j} + \frac{X_s}{X_{f_j}} u_{q_j} + X_s i_{d_j}] sin\theta_{p_k p_j}}_{\text{Couplings}}], \end{aligned} \tag{5.3}$$

$$\begin{aligned} V_{q_k} = {} & [R_s + R_k - \frac{X_s + X_k}{X_{f_k}} R_{f_k}] i_{q_k} + \frac{X_s + X_k}{X_{f_k}} u_{q_k} \\ & + [X_k + X_s] i_{d_k} - \hat{V}_s sin\theta_{ps_k} \\ & - \underbrace{\sum_{j=1, j\neq k}^{n} [[(R_s - R_{f_j}\frac{X_s}{X_{f_j}}) i_{d_j} + \frac{X_s}{X_{f_j}} u_{d_j} - X_s i_{q_j}] sin\theta_{p_k p_j}}_{\text{Couplings}} \\ & \underbrace{+[(R_s - R_{f_j}\frac{X_s}{X_{f_j}}) i_{q_j} + \frac{X_s}{X_{f_j}} u_{q_j} + X_s i_{d_j}] cos\theta_{p_k p_j}}_{\text{Couplings}}], \end{aligned} \tag{5.4}$$

where R_f and X_f are respectively the resistance and reactance of each VSC's terminal filter, R and X represent the total resistance and reactance of the transformer and the transmission line connecting each VSC to the PCC, u_d and u_q are the control signals, $\theta_{ps_j} = \theta_{pll_j} - \theta_s$, and $\theta_{p_j p_k} = \theta_{pll_j} - \theta_{pll_k}$. The parameters of any other desired topology at the AC side can be embedded in the above-mentioned impedances.

Coupling terms identified in (5.3)-(5.4) are associated with the variables of adjacent VSCs. Thus, if the VSCs do not have a connection at the AC side, these terms become zero, and each VSC operates as if it is the sole converter connected to the AC system, and consequently, there will be no interactions among the VSCs. In the rest of the chapter, the term '*uncoupled*' dynamics refers to equations (5.3)-(5.4) without the coupling terms, and the multi-VSC system in this case is an interaction-free system (IFSYS). The term '*coupled*' dynamics refers to (5.3)-(5.4) in the presence of coupling terms, and the multi-VSC system, in this case, is an interconnected system (INSYS).

Considering (5.3)-(5.4) as well as the active power, reactive power, and DC-link voltage equations [86] of each VSC in Fig. 5.1, the small-signal dynamics of the system can be described by the multi-input multi-output state-space model of

$$\dot{x}_k = A_{kk}x_k + \sum_{j=1, j\neq k}^{n} [A_{kj}x_j + B_{kj}u_j], \tag{5.5}$$

$$y_k = C_{kk}x_k + \sum_{j=1, j\neq k}^{n} [C_{kj}x_j + D_{kj}u_j], \tag{5.6}$$

where $x_k = [\tilde{i}_{d_k}, \tilde{V}_{dc_k}, \tilde{i}_{q_k}, \tilde{\theta}_{pll_k}, \tilde{x}_{pll_k}]^T$, $\tilde{x}_{pll_k}$ is the internal state of PLL, $u_k = [u_{d_k}, u_{q_k}]^T$ is the converter control input, and $y_k = [y_{d_k}, y_{q_k}]^T$ is the converter control output, $k \in \{1, , ..., n\}$. The d-axis control output (y_d) can be either the DC voltage or active power, and the q-axis control output (y_q) shows the voltage or reactive power of the AC terminal, depending on the VSC's control mode. It should be noted that (5.5)-(5.6) provide the full small-signal dynamics of the multi-VSC system with the fast current dynamics and PLL included. As the objective of the chapter is studying the impact of control modes on the external control loop interactions, the PLL is not modeled separately and is embedded in (5.5)-(5.6). Furthermore, in (5.5)-(5.6), no perturbation from the DC side is considered because the aim is to study the interactions among the VSCs sharing a PCC, not those sharing a DC system.

Based on the state-space model in (5.5)-(5.6), the state variables of each VSC are impacted not only by its state variables and control inputs but also by those of the adjacent

Table 5.1: Parameters of the test system [5]

Quantity	Value	Description
P	200 MW	Active power of each VSC
V_{dc}	400 KV	DC voltage
V_s	230 KV	AC grid RMS voltage
f	60	Frequency
L	0.0291 H	Transformer+ transmission line inductance
L_f	0.0725 H	Filter inductance
C_{dc}	300 μ F	DC side capacitance
K_p^{pll}, K_I^{pll}	50, 716	PLL controller gains

converters, resulting in the coupled transfer function matrix of

$$G(s) = \begin{bmatrix} G_{11}(s) & .... & G_{1n}(s) \\ G_{21}(s) & ... & G_{2n}(s) \\ ... & ... & ... \\ G_{n1}(s) & ... & G_{nn}(s) \end{bmatrix}_{2n\times 2n}, \tag{5.7}$$

where $G_{ij}(s)$ is a 2×2 transfer function matrix. By neglecting the coupling dynamics in (5.3)-(5.4) and consequently neglecting the off-diagonal matrices $A_{kj}, B_{kj}, C_{kj}, D_{kj}$ in (5.5)-(5.6), the IFSYS of VSCs can be described by the uncoupled transfer function matrix

$$\bar{G}(s) = \begin{bmatrix} \bar{G}_{11}(s) & 0 & ... & 0 \\ 0 & \bar{G}_{22}(s) & 0 & ... \\ ... & ... & ... & \\ 0 & ... & 0 & \bar{G}_{nn}(s) \end{bmatrix}_{2n\times 2n}, \tag{5.8}$$

where $\bar{G}_{kk}(s)$ is different from $G_{kk}(s)$ due to the off-diagonal matrices $A_{kj}, B_{kj}, C_{kj}, D_{kj}$ in (5.5)-(5.6).

5.3 Interaction Analysis

In this section, μ analysis is introduced as the method of analysis to study the impact of control mode on external interactions and to identify the control modes for which stabilizing the IFSYS of VSCs ensures the stability of the INSYS of VSCs.

5.3.1 Interaction impact on system small-signal stability

To illustrate the impact of interactions on system stability, the dominant eigenvalues of the INSYS of three VSCs is presented in Fig. 5.2. In Fig. 5.2, SCR$= 1.3$ and all VSCs operate in DC voltage/AC voltage control mode. The VSCs are independently stabilized, and therefore, the IFSYS is stable. The set of outer controllers is $K^o_{d_k} = 3.13 + \frac{5.91}{s}$, $K^o_{q_k} = 0.0011 + \frac{2.73}{s}$, $k \in \{1, 2, 3\}$ (similar for all three VSCs). These controllers are obtained for each VSC independent of the others such that the outer control loops are at least 10 times slower than the inner loops (with the time constant of 2 ms), and the maximum overshoot is 20%. The time-domain step response of VSC_1 is presented in Fig. 5.2b to show the dynamic response of the independently designed VSCs. Based on Fig.

5.2a, although the IFSYS is stable and has a satisfactory dynamic response, the locations of the eigenvalues indicate that the INSYS of these three VSCs is unstable.

For clarity and simplicity of the analysis in the rest of the chapter, Table 5.2 presents the various possible combinations of control modes for a 3-VSC system, as a specific case of a multi-VSC system. Since the parameters of the converters are similar and to prevent redundancy, not all the possible permutations are included. The ”control mode No.” will be used later to refer to each set of control modes.

5.3.2 Method of analysis

Fig. 5.3a shows the VSCs' combined inner and outer controllers, which are designed independently for each VSC such that the IFSYS is stable and well-behaved, and Fig. 5.3b shows the employment of the independently designed controllers in the INSYS of three VSCs. The combined inner-outer controllers of VSC_k is described by

$$\underbrace{K_k(s)}_{2\times2} = \underbrace{\frac{K_k^{in}(s)}{1+K_k^{in}(s)(\frac{1}{L_{f_k}s+R_{f_k}})}}_{K_k^{in,cl}(s)} \underbrace{K_k^{o}(s)}_{2\times2}; k \in \{1, ..., n\}, \tag{5.9}$$

where $K_k^{in}(s)$ is the inner controller and $K_k^{o}(s)$ is the outer controller. The controller of the multi-VSC system is given by

$$K(s) = diag(\big[K_1(s), \quad ... \quad , K_n(s)\big])_{2n\times 2n}.$$

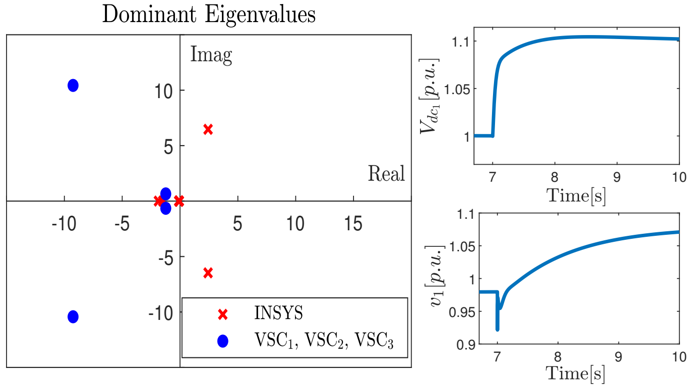

(a) (b)

Figure 5.2: (a) Dominant system eigenvalues for a certain set of controller parameters and (b) time-domain response of VSC_1.

Table 5.2: Various sets of control modes in a 3-VSC system

Control mode No.	Control outputs	Control mode No.	Control outputs
CN_{11}	$y_1 = [V_{dc_1}, v_1]$ $y_2 = [V_{dc_2}, v_2]$ $y_3 = [V_{dc_3}, v_3]$	CN_{21}	$y_1 = [P_1, v_1]$ $y_2 = [P_2, v_2]$ $y_3 = [P_3, v_3]$
CN_{12}	$y_1 = [V_{dc_1}, v_1]$ $y_2 = [V_{dc_2}, v_2]$ $y_3 = [V_{dc_3}, Q_3]$	CN_{22}	$y_1 = [P_1, v_1]$ $y_2 = [P_2, v_2]$ $y_3 = [P_3, Q_3]$
CN_{13}	$y_1 = [V_{dc_1}, v_1]$ $y_2 = [V_{dc_2}, Q_2]$ $y_3 = [V_{dc_3}, Q_3]$	CN_{23}	$y_1 = [P_1, v_1]$ $y_2 = [P_2, Q_2]$ $y_3 = [P_3, Q_3]$
CN_{14}	$y_1 = [V_{dc_1}, Q_1]$ $y_2 = [V_{dc_2}, Q_2]$ $y_3 = [V_{dc_3}, Q_3]$	CN_{24}	$y_1 = [P_1, Q_1]$ $y_2 = [P_2, Q_2]$ $y_3 = [P_3, Q_3]$

For two systems with the transfer functions $G(s)$ and $\bar{G}(s)$ and controller $K(s)$, the characteristic polynomials $det(I+GK)$ and $det(I+\bar{G}K)$, respectively, can be used to study system stability. The relationship between the two characteristic polynomials is

$$det(I + GK) = det(I + \bar{G}K)det(I + E\bar{T}), \tag{5.10}$$

where E is the relative difference between the coupled and uncoupled transfer function matrices, defined by [75]

$$E = (G - \bar{G})\bar{G}^{-1}, \tag{5.11}$$

and $\bar{T}$ is the complementary sensitivity function such that $\bar{T} = I - (I+\bar{G}K)^{-1}$. According to (5.10) and assuming that $\bar{T}$ is stable, $det(I + GK)$ will have all its roots in the open left-half plane (LHP) if and only if $det(I + E\bar{T})$ has all its roots in the LHP [75].

The term $det(I+E\bar{T})$ in (5.10) indicates how the characteristic polynomial of the IFSYS changes with interactions to form the characteristic polynomial of the INSYS. Therefore, as long as the interactions among the converters do not result in the roots of $det(I + E\bar{T})$ leaving the LHP, IFSYS's stability ensures INSYS's stability. Fig. 5.4 shows the roots of $det(I + E\bar{T})$ for the set of controller parameters used in Section 5.3. A. As some of the roots of $det(I + E\bar{T})$ are not located in the LHP, the IFSYS stability does not result in the stability of INSYS, which was also shown in Fig. 5.2a.

To have all the roots of $det(I + E\bar{T})$ in the LHP, the Nyquist plot of $det(I + E\bar{T})$ must

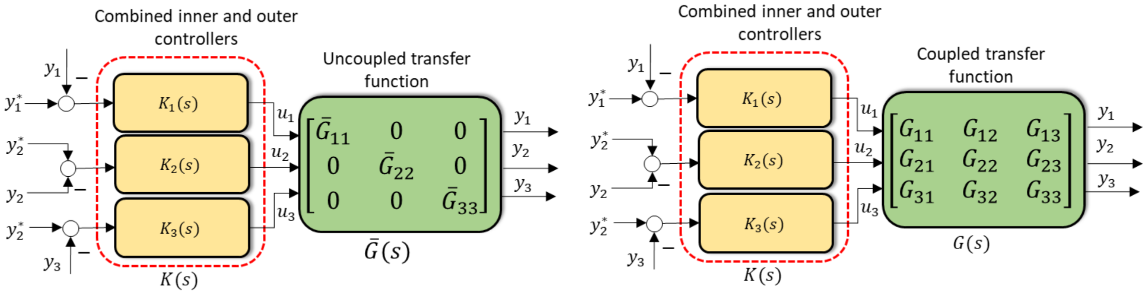

(a) (b)

Figure 5.3: (a) Independently designed controllers of the IFSYS and (b) INSYS with the independently designed controllers.

not encircle the origin, which leads to the sufficient stability condition of

$$\rho(E\bar{T}(j\omega)) < 1 \quad \forall\omega, \tag{5.12}$$

where ρ is the spectral radius [75]. (5.12) is a sufficient condition ensuring INSYS stability in the presence of interactions, when IFSYS is stable. A weaker sufficient condition for INSYS stability based on (5.12) is to have

$$\bar{\sigma}(\bar{T}(j\omega)) < \mu(E(j\omega))^{-1} \quad \forall\omega, \tag{5.13}$$

where $\bar{\sigma}$ is the maximum singular value [75]. μ is the structured singular value defined by

$$\mu(E) = \frac{1}{\min_{\Delta}\{\bar{\sigma}(\Delta)|\det(I - E\Delta) = 0\}}\ , \tag{5.14}$$

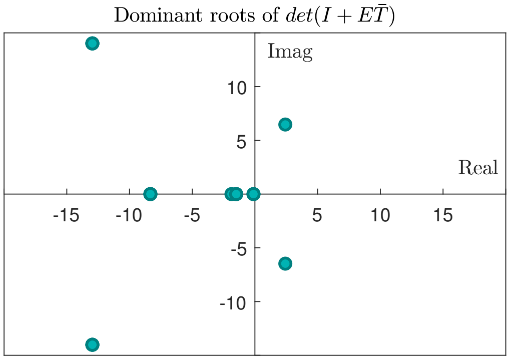
Dominant roots of $det(I + E\bar{T})$

Figure 5.4: Dominant roots of $det(I + E\bar{T})$ for the set of controller parameters used in Fig. 5.2.

where the structured uncertainty Δ has a block-diagonal structure similar to the structure of $\bar{T}$ [75]. $\mu(E)$ can be computed for any given E and by searching through stable perturbations Δ with a similar structure to $\bar{T}$ and finding the reciprocal of the smallest $\bar{\sigma}(\Delta)$ making $det(I - E\Delta) = 0$.

According to (5.13),

1. the magnitude of $\mu(E(s))^{-1}$ is an indicator of the level of interactions, and it corresponds to the impact of interactions on INSYS stability. The smaller the coupling terms in (5.3)-(5.4), the smaller E and $\mu(E)$ will be. If $\mu(E(s))^{-1}$ is large enough, the INSYS stability will be ensured for a wide range of controllers that have stabilized the IFSYS.
2. as $\mu(E(s))^{-1}$ does not depend on the controllers' parameters and only depends on the system parameters and control modes, it can be assumed as the available headroom for the independent design of converters' controllers that stabilize the INSYS. In the case of weak coupling among the converters, $\mu(E(s))^{-1}$ will be sufficiently large, leaving a large headroom for the independent design of controllers that stabilize the INSYS of multiple VSCs.

It should be noted that the controllers are often designed to provide an acceptable set-point tracking capability for the system. This requirement is usually taken care of by embedding an integrator in the controllers, resulting in $\bar{T} = I$ at low frequencies. Thus, the low frequency value of $\bar{\sigma}(\bar{T})$ is determined by the controllers' integral action, while the controller order and parameters can be adjusted to shape $\bar{\sigma}(\bar{T})$ in the mid- and high-frequency ranges. As a result, maintaining $\mu(E(s))^{-1} > 1$ at low frequencies is necessary to preserve (5.13). Satisfying (5.13) at mid- and high-frequency ranges can be taken care of by the proper selection of controller parameters. Thus, $\mu(E(0))^{-1}$ is an important criterion for the interaction analysis. If $\mu(E(0))^{-1} < 1$ for a certain control mode, any controller with set-point tracking capability would violate (5.13), and the stability of INSYS cannot be guaranteed even if the IFSYS is stable.

Fig. 5.5 shows two illustrative examples of $\mu(E(s))^{-1}$ for two different sets of control modes, CN_{11} and CN_{13}. To identify which control mode results in larger interactions, firstly, the value of $\mu(E(0))^{-1}$ in the two control modes should be compared to each other. In CN_{13}, $\mu(E(0))^{-1} > 1$, and thus the controller parameters can be selected such that (5.13) is satisfied and consequently INSYS is stabilized by stabilizing IFSYS. However, in CN_{11}, $\mu(E(0))^{-1} < 1$, which violates (5.13) for any well-tuned controllers. Therefore, the stabilizing controllers of IFSYS may or may not stabilize the INSYS in CN_{11}. Furthermore, compared to CN_{11}, there is a larger headroom for designing controllers operating in CN_{13} as $\mu(E(s))^{-1}$ is larger, and thus the interactions have less impact on the stability of INSYS in CN_{13}. It should also be noted that although $\mu(E(s))^{-1}$ in CN_{11} is larger than that in CN_{13} for the high frequency range, the decisive frequency range for the design of controllers such that (5.13) is satisfied is the low- and mid-frequency ranges. The reason is that by increasing the order of controllers, it would be possible to shape $\bar{\sigma}(\bar{T})$ such that, in the high-frequency range, it approaches zero and consequently satisfies (5.13).

In Section 5.5, $\mu(E(s))^{-1}$ will be plotted for all the possible control modes of Table 5.2, and the impact of the control mode on the interactions will be investigated accordingly. Prior to the simulations, in the following, it is proved that changing the d-axis control mode does not impact $\mu(E(0))^{-1}$.

Proof: Considering the small-signal dynamics of DC-link voltages in Fig. 1 and neglecting the DC side perturbations,

$$C_k \frac{\mathrm{d}\tilde{V}_{dc_k}}{\mathrm{d}t} = -\frac{\tilde{P}_k}{V_{dc_{k_0}}} + \frac{P_{k_0}}{V^2_{dc_{k_0}}} \tilde{V}_{dc_k}; \quad k \in \{1, 2, 3\}. \tag{5.15}$$

Using (5.15),

$$\tilde{V}_{dc_k}(s) = \frac{-1}{V_{dc_{k_0}}} \frac{1}{C_k s - (\frac{P_{k_0}}{V^2_{dc_{k_0}}})} \tilde{P}_k(s); \quad k \in \{1, 2, 3\}. \tag{5.16}$$

Based on (5.16), when the d-axis control mode changes from active power to DC voltage control, the control outputs of the system are related to each other by

$$\underbrace{[\tilde{V}_{dc_1}, y_{q_1}, \tilde{V}_{dc_2}, y_{q_2}, \tilde{V}_{dc_3}, y_{q_3}]^T}_{y_{dc}} = W(s) \underbrace{[\tilde{P}_1, y_{q_1}, \tilde{P}_2, y_{q_2}, \tilde{P}_3, y_{q_3}]^T}_{y_P}, \tag{5.17}$$

where

$$W(s) = diag\{[\frac{-1}{V_{dc_{k_0}}(C_k s - (\frac{P_{k_0}}{V^2_{dc_{k_0}}}))}, 1]\}. \tag{5.18}$$

Assuming $P_{k_0} = 1$ [pu] and $V_{dc_{k_0}} = 1$ [pu], it can be derived that $W(0) = I$ and consequently, $\mu(E(0))^{-1}|_{y_{dc}} = \mu(E(0))^{-1}|_{y_P}$. Therefore, if $\mu(E(0))^{-1} > 1$ is satisfied for the DC voltage control mode, it will also be satisfied for the active power control mode.

5.4 VSCs Control Design for Interaction Mitigation

In this section, a criterion is proposed for designing the controllers of the IFSYS independently, which ensures INSYS stability as well. The main advantage of the proposed

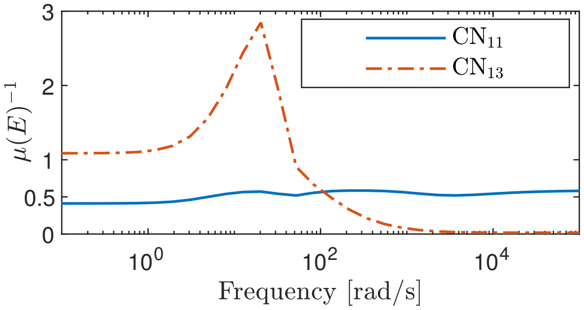

Figure 5.5: $\mu(E(s))^{-1}$ for two control modes versus frequency.

controller design is the mitigation of the negative impact of interactions on the interconnected system stability. It should be noted that this procedure can be applied to any type of individual controller as it aims at re-tuning the individual controllers to mitigate the interactions. For example, if robust controllers are initially designed for the individual converters, the proposed procedure can be utilized to design a set of robust controllers that ensure the stability of INSYS.

With an integrator in the outer control loops to achieve set-point tracking capability, $\mu(E(0))^{-1} > 1$ will become a necessary condition for using (5.13) to design the controllers of the IFSYS such that INSYS stability is ensured. The main steps of designing the controllers for each VSC are as follows:

1. Set the time constant of the inner controller (τ) and find the inner controller parameters as explained in [86]. Find $K_k^{in,cl}(s)$ in (5.9) and determine $\bar{G}_{kk}(s)K_k^{in,cl}(s)$.
2. Decide on the bandwidth of the outer control loop (BW_o) by considering the rule of thumb for cascaded inner-outer loops as $BW_o < \frac{0.1}{\tau}$. Depending on the order of $\bar{G}_{kk}(s)$, choose the order of the outer controller $K_k^o(s)$. An integral action must be included in the outer controller. Knowing $\bar{G}_{kk}(s)K_k^{in,cl}(s)$, $K_k^o(s)$ is the only unknown in the control structure of Fig. 5.3a. Tune the parameters of $K_k^o(s)$ to create a stable feedback loop in Fig. 5.3a and ensure the desirable time-domain specifications.
3. Check whether (5.13) is satisfied. Depending on the magnitude of $\mu(E(s))^{-1}$, there will be an available headroom for the design of controllers.
4. If (5.13) is satisfied, the design is complete. Otherwise, change the parameters of the outer controllers in step 2 and repeat steps 2-4.

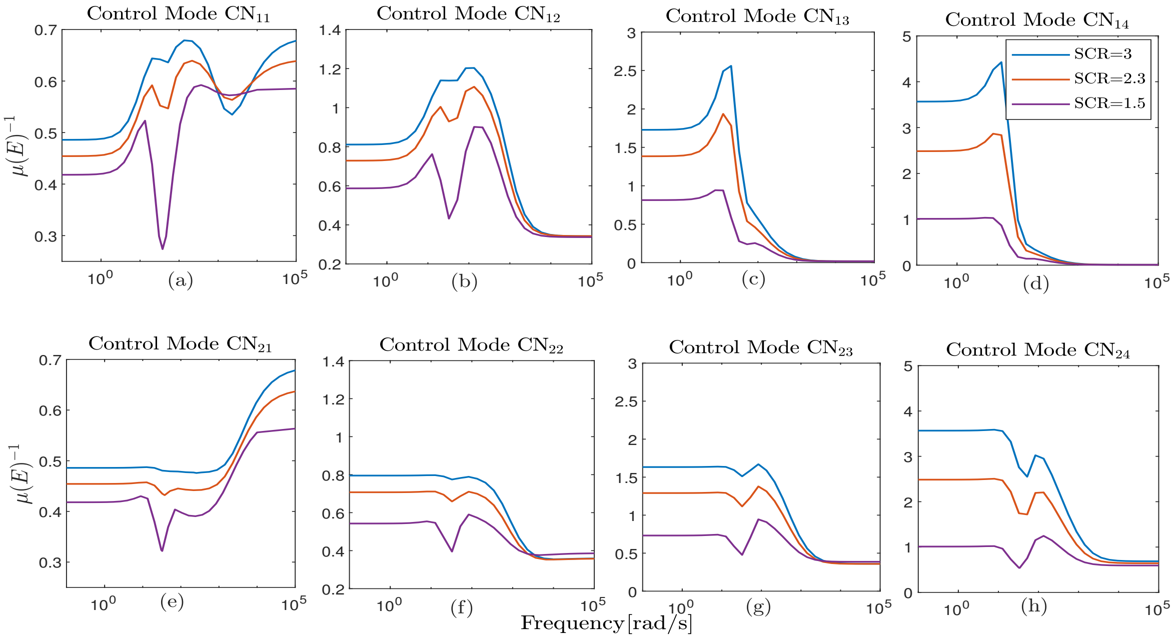

Figure 5.6: $\mu(E)^{-1}$ against frequency for various sets of control modes in Table 5.2 and for several SCRs, $P_1 = P_2 = P_3 = 1$ [pu].

In cases where $\mu(E(0))^{-1} < 1$, a joint controller design for VSCs (in contrast to an independent design) may result in satisfying (5.13) and thus reducing the negative impact of interactions on stability. In the joint design, the coupling among certain converters is taken into account in the control design. To perform the joint control design, $\bar{G}(s)$ in (5.8) is modified after the dynamics of the converters forming a group are moved from the *coupling* term to the *uncoupled dynamics* term in (5.3)-(5.4). As an example, to perform the joint design for VSC_1 and VSC_2, while designing VSC_3 independently, $\bar{G}(s)$ is defined as

$$\bar{G}(s) = \begin{bmatrix} \bar{G}_{11}(s) & \bar{G}_{12}(s) & 0 \\ \bar{G}_{21}(s) & \bar{G}_{22}(s) & 0 \\ 0 & 0 & \bar{G}_{33}(s) \end{bmatrix}. \tag{5.19}$$

The converters involved in the joint design are mainly those manufactured by a single vendor as this will ensure access to the detailed model of those converters. The proposed control design will facilitate the multi-vendor realization of hybrid AC/DC systems as it will ensure design confidentiality by joint design of converters' controllers whose models are available and independent control design of converters whose models are confidential

[27,32].

In Section 5.5, certain recommendations will be given about the control mode of the converters included in the joint control design to reduce the impact of interactions on the interconnected system stability. These recommendations will be based on the magnitude of $\mu(E(s))^{-1}$ for various control modes of the converters forming a group.

5.5 Case Study

In this section, the impact of control modes on the interactions and the viability of the proposed stability criterion for the controller design are studied using a test system with three converters sharing a PCC with the parameters given in Table 5.1. This study covers the range of SCRs from strong (SCR>3) to weak ($2 < \text{SCR} < 3$) and very weak AC systems (SCR< 2) [42]. The nonlinear model of the test system is built in MATLAB/SIMULINK, and the linearized system is obtained to form the small-signal model required for the aforementioned studies.

5.5.1 Impact of converters' control modes on interactions

To evaluate the impact of control modes on the level of interactions among converters, $\mu(E(s))^{-1}$ for various SCR values and the control modes of Table 5.2 is depicted in Fig. 5.6. In Fig. 5.6, the sub-figures next to each other have the same d-axis control mode, and the ones on the top and bottom rows have the same q-axis control mode.

To investigate the impact of q-axis control mode on the interactions, Figs. 5.6a-d show $\mu(E(s))^{-1}$ for various sets of q-axis control modes and a fixed d-axis control mode (DC voltage control mode). In Figs. 5.6a-b, $\mu(E(0))^{-1} < 1$, which violates (5.13) for any well-tuned controller, and thus the INSYS stability is not guaranteed even if IFSYS is stable. However, in Figs. 5.6c-d, $\mu(E(0))^{-1} > 1$ for several SCR values. Therefore, the controller parameters of the IFSYS in control modes CN_{13} and CN_{14} can be set based on the step-by-step procedure discussed in Section 5.4 to satisfy (5.13) and consequently stabilize the INSYS. Additionally, for all SCRs, $\mu(E(s))^{-1}$ is larger in Fig. 5.6d than that of Fig. 5.6c for the low- and mid-frequency ranges, which results in a larger available headroom for designing the converters' controllers in control mode CN_{14}. Similar conclusions can be made about the impact of q-axis control mode on the interactions based on Figs. 5.6e-h.

To study the impact of d-axis control mode on the interactions, each of Figs. 5.6a-d are compared with their counter-parts in Figs. 5.6e-h, with the same q-axis control mode

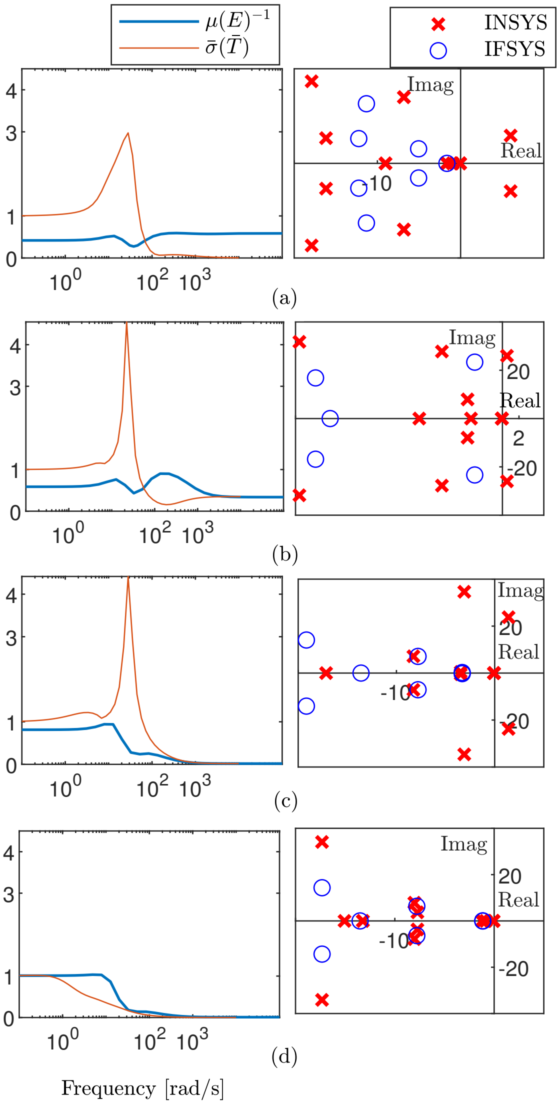

(a)

(b)

(c)

(d)

Figure 5.7: $\bar{\sigma}(\bar{T})$, $\mu(E)^{-1}$ and eigenvalue plot of IFSYS and INSYS for (a)-(b) control mode CN_{11}, (c)-(d) control mode CN_{12}, (e)-(f) control mode CN_{13}, and (g)-(h) control mode CN_{14}, SCR=1.5.

and a different d-axis control mode. It is observed that the d-axis control mode does not impact $\mu(E(0))^{-1}$, which was also proved in Section 5.3. This means that, in the proposed control design based on (5.13), the d-axis control mode does not affect the relationship between the IFSYS and INSYS stability.

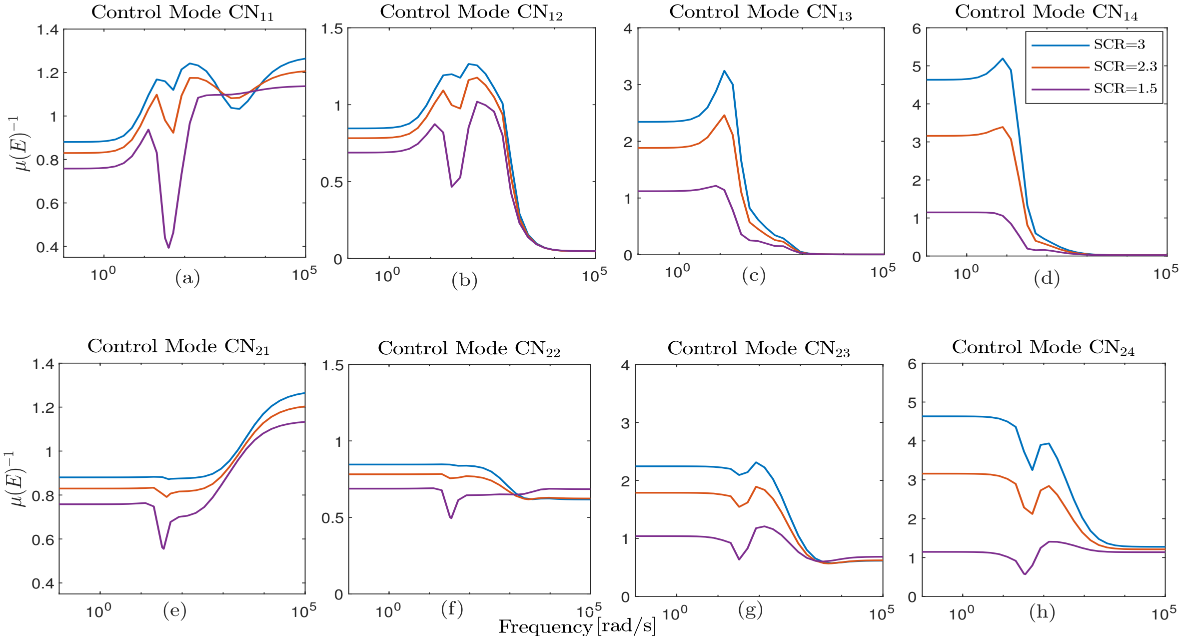

Figure 5.8: $\mu(E(s))^{-1}$ against the frequency for various sets of control modes in Table 5.2 with VSC_1 and VSC_3 forming a group.

In summary, when all the VSCs operate in AC voltage control mode, the largest interactions happen (Figs. 5.6a and e). Moving from Fig. 5.6a (e) toward Fig. 5.6d (h) with more VSCs in the reactive power control mode will reduce the impact of interactions on the stability of INSYS, regardless of the d-axis control mode. However, the control design headroom in the DC voltage control mode is larger than that in the active power control mode as $\mu(E(s))^{-1}$ is larger, Fig. 5.6.

Fig. 5.7 shows $\mu(E(s))^{-1}$ and $\bar{\sigma}(\bar{T})$ for DC voltage control mode and various sets of q-axis control mode. It should be noted that Fig. 5.7 is plotted for a certain set of controller parameters for illustration purposes only. As Fig. 5.7 shows, the only control mode for which (5.13) is satisfied and thus for which the independent design of the converters has stabilized the INSYS is control mode CN$_{14}$, where all the converters control the reactive power. In this control mode, the set-point tracking capability as well as stability are ensured for the INSYS by the independent control design of the IFSYS. In other control modes in Figs. 5.7a-c, while the order of the controller can adjust the high-frequency characteristics of $\bar{\sigma}(\bar{T})$, the low-frequency characteristics of $\bar{\sigma}(\bar{T})$ mainly depends on the integral action. Since $\mu(E(0))^{-1} < 1$ in Figs. 5.7a-c, $\bar{\sigma}(\bar{T}) < \mu(E(s))^{-1}$ cannot be achieved and the stability of the INSYS cannot be guaranteed. The eigenvalue map of the system for each control mode verifies the INSYS stability in control mode CN_{14}, which is shown in Fig. 5.7.

5.5.2 Impact of converters' joint control design on interactions

For the set of control modes discussed in Table 5.2, various scenarios of joint design can be considered. For example, in control mode CN_{12}, the first scenario would consider the two VSCs in the AC voltage control mode as a group (VSC_1 and VSC_2), and the third VSC in the reactive power control mode as an independent unit (VSC_3). The second scenario is to form a group consisting of one of the converters in AC voltage control mode and one in reactive power control mode ((VSC_1 or VSC_2) and VSC_3) for the joint design, while designing the controller of the other VSC in AC voltage control mode independently (VSC_2 or VSC_1). For control mode CN_{11} in Table 5.2, since all the VSCs have similar parameters and ratings, there is only one joint design scenario, where any of the two VSCs are involved in the joint design and the third VSC is considered as an independent unit. The rest of the possible joint design scenarios can be obtained similarly.

Fig. 5.8 shows $\mu(E(s))^{-1}$ when VSC_2 controller is designed as an independent unit, and VSC_1 and VSC_3 form a group and their controllers are jointly designed. By comparing Fig. 5.8 against Fig. 5.6 in each control mode, it can be observed that due to the joint control design, all $\mu(E(s))^{-1}$ curves have shifted up, indicating that the available headroom for designing stabilizing controllers has become larger, and the interactions have decreased. However, even with the joint control design, in control modes CN_{11} and CN_{21}, $\mu(E(0))^{-1} < 1$ and thus, (5.13) cannot be satisfied for any controller with an integral action, Figs. 5.8a and e. Also, there is not any other distinct joint design scenario that would result in $\mu(E(0))^{-1} > 1$. Thus, having all the VSCs in AC voltage control mode results in the highest interaction level among the VSCs, and the joint design will not be a remedial action in this case to make $\mu(E(0))^{-1} > 1$ and consequently the INSYS stability cannot be guaranteed.

Another scenario is the joint design of VSC_1 and VSC_2 in control modes CN_{12} and CN_{22}, where the converters operating in AC voltage control mode form a group, and the converter in reactive power control mode is considered as an individual unit. For this scenario, $\mu(E(s))^{-1}$ is shown in Figs. 5.9a and c. Comparing $\mu(E(s))^{-1}$ in Figs. 5.9a and c with Figs. 5.8b and f reveals that this joint design scenario results in a larger $\mu(E(s))^{-1}$. Especially, $\mu(E(0))^{-1} > 1$ in Figs. 5.9a and c indicating that (5.13) can be met and the INSYS can be stabilized with stabilizing the IFSYS.

In control modes CN_{13} and CN_{23}, the joint control design of VSC_2 and VSC_3 results in another feasible scenario, where the controllers of VSCs operating in reactive power control mode are jointly designed, and the controller of the VSC in AC voltage control mode is designed independently. Comparing $\mu(E(s))^{-1}$ in Figs. 5.9b and d against Figs. 5.8c and g shows that a smaller $\mu(E)^{-1}$, and thus, a smaller stability headroom is provided with the joint design of the VSCs when the VSC in the AC voltage control mode is designed independently.

Based on Figs. 5.6, 5.8 and 5.9, it can be concluded that

1. joint design of VSCs's controllers can always lessen the impact of interactions on the interconnected system stability as $\mu(E(s))^{-1}$ curves have shifted up in Figs. 5.8-5.9 compared to Fig. 5.6.
2. joint control design of converters operating in AC voltage control mode, such that no converter in AC voltage control mode is designed individually, corresponds to the recommended design scenario in terms of interaction mitigation. However, when all converters operate in AC voltage control mode, the joint design might not necessarily reduce the high level of interactions and may not ensure the INSYS's stability.
3. if for any operational reasons, it is not possible to jointly design the converters in AC voltage control mode, it is recommended to form the groups of the converters such that the lowest number of converters in AC voltage control mode are designed independently.

5.5.3 Joint design of stabilizing controllers

Joint design of VSC_1 and VSC_2 in control mode CN$_{12}$

As an example to clarify the impact of controllers' joint design on the external control loop interactions, control mode CN$_{12}$ is considered with the 3-VSC system operating under SCR=1.5. As shown in Fig. 5.6 and Fig. 5.9, CN$_{12}$ is the control mode with the highest interaction level for which the controllers can be designed independently to satisfy (5.13) and consequently to ensure the stability of the INSYS. It should be noted that for CN$_{11}$, stabilizing controllers cannot be designed based on (5.13). It is assumed that VSC_1 and VSC_2, operating in AC voltage control mode, are built by the same manufacturer, and thus their joint controller design is possible. Fig. 5.10 shows $\mu(E(s))^{-1}$ and $\bar{\sigma}(\bar{T})$ for the controllers designed based on steps 1-4 of the control design procedure in Section 3. C for VSC_1 and VSC_2 as a group and for VSC_3 as an individual unit. As the sufficient condition (5.13) is satisfied according to Fig. 5.10, it is guaranteed that the INSYS of three VSCs is stable even in the presence of interactions. The eigenvalue map of the INSYS of three VSCs is also shown in Fig. 5.10, which confirms that the INSYS is stable.

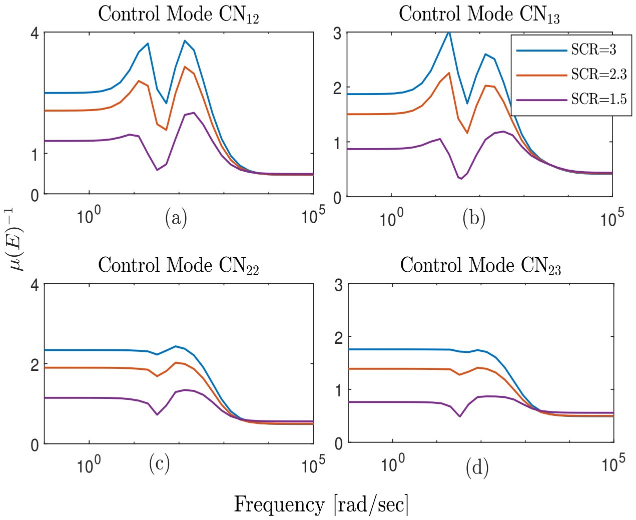

Figure 5.9: $\mu(E)^{-1}$ against frequency for various SCRs with joint design for (a) and (c) VSC_1 and VSC_2, and (b) and (d) VSC_2 and VSC_3.

Joint design of VSC_1 and VSC_3 in control mode CN$_{13}$

In control mode CN$_{13}$, when the 3-VSC system operates under SCR=1.5, the joint control design of the VSC controlling the AC voltage (VSC_1) and the VSC controlling the reactive

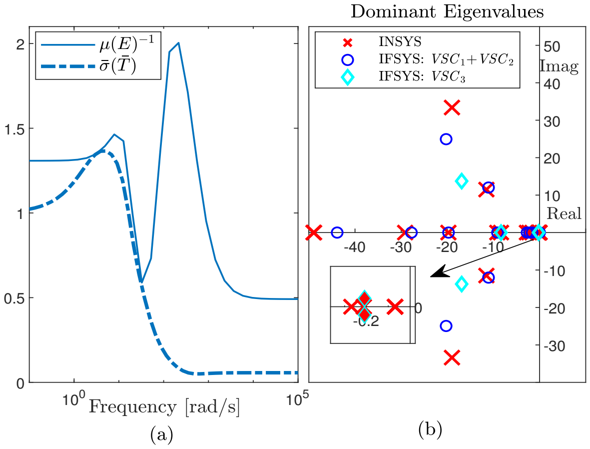

Figure 5.10: $\bar{\sigma}(\bar{T})$, $\mu(E)^{-1}$ and eigenvalue plot of IFSYS and INSYS for the joint design of VSC_1 and VSC_2 in control mode CN$_{12}$.

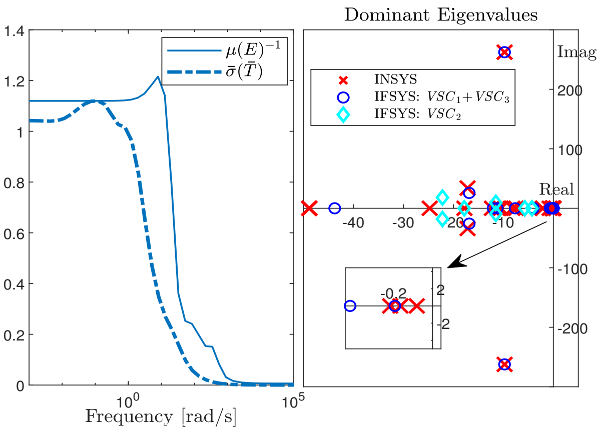

(a) (b)

Figure 5.11: $\bar{\sigma}(\bar{T})$, $\mu(E)^{-1}$ and eigenvalue plot of IFSYS and INSYS for the joint design of VSC_1 and VSC_3 in control mode CN_{13}.

power (VSC_3) is a remedial action to reduce the interactions. Based on the procedure discussed in Section III. C, Fig. 5.11 shows $\mu(E(s))^{-1}$ and $\bar{\sigma}(\bar{T})$ for the designed controllers. As shown in Fig. 5.11, the sufficient condition (5.13) is satisfied in this control design and therefore, it is guaranteed that the INSYS of three VSCs is stable even in the presence of interactions. Fig. 5.11 shows the eigenvalue map confirming that the INSYS is stable.

5.6 Conclusion

In this chapter, external control loop interactions among VSCs sharing a common AC system were studied, and the impact of control mode on the interactions was investigated. μ analysis was used to measure the level of interactions for various sets of control modes and identify the set of control modes for which the stability of individual VSCs can ensure the stability of the interconnected system (INSYS) of VSCs. The analysis indicated that, regardless of the d-axis control mode, the largest interactions occur if the adjacent converters simultaneously regulate the AC voltage via their q-axis control loop. Furthermore, having more VSCs in the reactive power control mode will lessen the impact of interactions on stability. Moreover, there is a larger headroom for the independent design of stabilizing converters' controllers in the DC voltage control mode than in the active power control mode.

A sufficient stability criterion was proposed for the independent design of converters' outer control loops such that the multi-VSC system stability is ensured. In case of severe interactions, where the INSYS becomes unstable even if each VSC is stable, a joint control design was proposed to stabilize the INSYS. The performed stability analysis illustrated that the joint control design of converters in AC voltage control mode such that the lowest number of converters in AC voltage control mode are designed independently is the best remedial action to reduce the impact of control loop interactions on the stability of multi-VSC systems.

Chapter 6

Mitigating AC Side External Control Loop Interactions in Multi-Vendor Multi-VSC Systems: Converters' Designers Viewpoint[1]

6.1 Introduction

In parallel voltage-sourced converter (VSC) schemes (or equivalently multi-VSC systems), where the converters have a connection at the AC side, the control loops of adjacent converters may impact each other and result in the interconnected system instability. The control design, therefore, is of high importance due to the control loop interactions. With multi-vendor considerations, the controller of each converter station needs to be designed individually to preserve model confidentiality.

This chapter develops a controller design method for mitigating the negative impact of these interactions on the stability of multi-VSC systems. The proposed controller design approach incorporates the external interactions as uncertainties into the system model and obtains the outer controllers of individual converters using H_∞ controller synthesis. The controllers are designed based on the model of individual VSCs rather than the exact model

---

[1] Ahmadloo, Fatemeh, and Pirooz Azad, Sahar. "A Robust Controller Design for Mitigating Control Loop Interactions in Multi-VSC Systems Built by Multiple Vendors." 2022 IEEE Power Energy Society General Meeting (PESGM). IEEE, 2022.

of the interconnected multi-VSC system, and thus they require only the exact model of individual VSCs and a reduced-order model of coupling dynamics. This modeling requirement ensures design confidentiality in multi-VSC systems built with multiple manufacturers due to the individual design of converter controllers, which does not require the exact model of adjacent converters. The performance of the proposed robust controller is evaluated using time-domain simulations and eigenvalue analysis in MATLAB/SIMULINK.

6.2 Modeling of VSCs Connected to a Shared PCC

Fig. 6.1a shows the schematic diagram of VSCs sharing the same AC system, and Fig. 6.1b shows the control system of each converter. Because the focus of this chapter is the interactions among the grid-side converters that are connected to a shared PCC, the

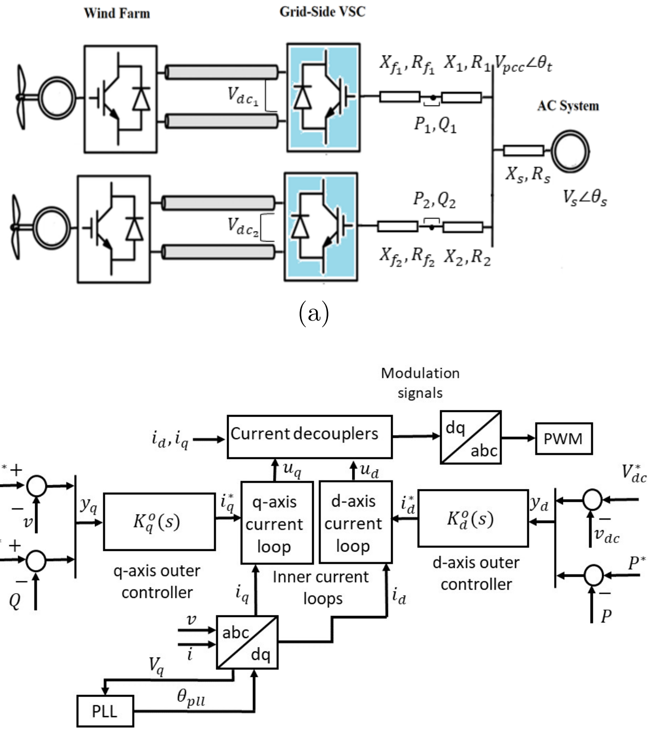

(a)

(b)

Figure 6.1: (a) Schematic diagram of parallel VSC stations and (b) the cascaded inner-outer control scheme.

perturbations from the DC side will be neglected in the rest of the chapter. The transfer function model of converters sharing the same AC system is obtained by considering the active power, reactive power, and DC-link voltage equations [86] of each VSC in Fig. 6.1.

The transfer function model of a 2-VSC system is represented by

$$G(s) = \begin{bmatrix} [G_{11}(s)] & [G_{12}(s)] \\ [G_{21}(s)] & [G_{22}(s)] \end{bmatrix}, \tag{6.1}$$

where each block is a 2 × 2 matrix. The off-diagonal blocks in (6.1) correspond to the couplings among the converters due to their AC side connection. The transfer function model of the uncoupled system of the two converters, where there is no interaction among them, can be described by

$$\tilde{G}(s) = \begin{bmatrix} [\tilde{G}_{11}(s)] & 0 \\ 0 & [\tilde{G}_{22}(s)] \end{bmatrix}. \tag{6.2}$$

The formulations of (6.1)-(6.2) is also applicable to a multi-VSC system, where the converters are divided into two groups. In such a case, the controllers of the converters in each group are jointly designed.

6.3 Robust H_∞ Controller Design

In this section, a robust H_∞ controller design is proposed such that the individual tuning of VSCs' controllers leads to the stability of the interconnected converters. The interactions among the converters are incorporated in the design of controllers as a specific type of uncertainty. The proposed control design facilitates the individual design of converter controllers without requiring the detailed model of converters built by other manufacturers.

6.3.1 Conventional H_∞ controller design

One of the challenges associated with control design techniques that rely on system models is the differences between the real-world systems and the available models due to imperfect plant data, time-varying dynamics, neglected high-frequency dynamics or non-linearity and complexity of systems [96]. Fig. 6.2a shows the structure of an uncertain system with the plant N_i, controller C_i, and uncertainty Δ_i. Although modeling of Δ_i depends on the source of uncertainty in the system which can be found in [96], any given uncertain system can be re-arranged to obtain the structure of Fig. 6.2a. Fig. 6.2b is another representation of Fig. 6.2a ($M - \Delta$ structure [96]) and is obtained by combining the controller and the plant of Fig. 6.2a.

Considering Fig. 6.2b, if for the given set of uncertainties $\Delta_i \in RH_\infty$ with $\bar{\sigma}(\Delta_i) < \gamma$,

$$\bar{\sigma}(\Delta_i M_i) < 1; \tag{6.3}$$

the structure in Fig. 6.2b (equivalently Fig. 6.2a) maintains robust stability. RH_∞ is the set of all real rational, stable transfer functions for which H_∞ norm can be defined.

6.3.2 Proposed H_∞ controller

The proposed controller of this chapter does not use the robust approach to address typical uncertainties associated with the system model. Rather, converter interactions are incorporated as uncertainties in the system model and then mitigated through the design of a robust controller. The rest of this subsection expounds on modeling the uncertainties to consider the external control interactions in the robust design of converters' controllers.

According to [19], a sufficient stability condition for a multi-VSC system is

$$\rho(E\tilde{T}) < 1, \tag{6.4}$$

where [96]

$$E = (G - \tilde{G})\tilde{G}^{-1}, \tag{6.5}$$

$\tilde{T} = \tilde{G}K(I + \tilde{G}K)^{-1}$, and ρ is the spectral radius operator. K is a diagonal matrix representing the transfer function models of converters' controllers. Because [96]

$$\rho(E\tilde{T}) < \bar{\sigma}(E\tilde{T}), \tag{6.6}$$

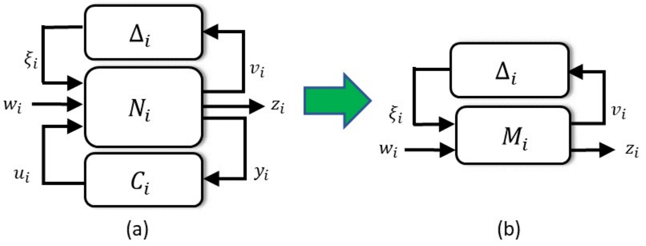

Figure 6.2: System configuration for H_∞ controller design: (a) general structure and (b) M-Δ structure.

where $\bar{\sigma}()$ shows the maximum singular value, a sufficient stability condition is obtained as:

$$\bar{\sigma}(E\tilde{T}) < 1. \tag{6.7}$$

In the following, a robust control design problem (type I) is formed based on (6.7). Assuming $\tilde{G}'$ as

$$\tilde{G}' = \begin{bmatrix} G_{11} & 0 \\ 0 & G_{22} \end{bmatrix}, \tag{6.8}$$

and by replacing $\tilde{G}$ with $\tilde{G}'$ in (6.5),

$$E = (G - \tilde{G}')\tilde{G}'^{-1} = \begin{bmatrix} 0 & G_{12}G_{22}^{-1} \\ G_{21}G_{11}^{-1} & 0 \end{bmatrix}. \tag{6.9}$$

Consequently,

$$\begin{aligned} E.\tilde{T} &= \begin{bmatrix} 0 & G_{12}G_{22}^{-1} \\ G_{21}G_{11}^{-1} & 0 \end{bmatrix} \begin{bmatrix} \tilde{T}_1 & 0 \\ 0 & \tilde{T}_2 \end{bmatrix} \\ &= \begin{bmatrix} 0 & G_{12}G_{22}^{-1}\tilde{T}_2 \\ G_{21}G_{11}^{-1}\tilde{T}_1 & \end{bmatrix} \\ &= \begin{bmatrix} 0 & G_{12}K_2(I + G_{22}K_2)^{-1} \\ G_{21}K_1(I + G_{11}K_1)^{-1} & 0 \end{bmatrix}. \end{aligned} \tag{6.10}$$

According to (6.10), which has zero diagonal blocks, the sufficient stability condition of (6.7) can be decomposed into two distinct conditions of

$$\bar{\sigma}(\underbrace{G_{12}}_{\Delta_2}\underbrace{K_2(I + G_{22}K_2)^{-1}}_{M_2}) < 1 \tag{6.11}$$

and

$$\bar{\sigma}(\underbrace{G_{21}}_{\Delta_1}\underbrace{K_1(I + G_{11}K_1)^{-1}}_{M_1}) < 1, \tag{6.12}$$

where each is associated with the control design of a single VSC or a group of VSCs. The objective is to determine the controllers $K_i(s)$ such that (6.11)-(6.12) are held, which is possible by solving a robust H_∞ control problem. Comparing (6.11)-(6.12) with (6.3) shows that G_{21} and G_{12} appear as multiplicative uncertainties to the systems M_1 and M_2.

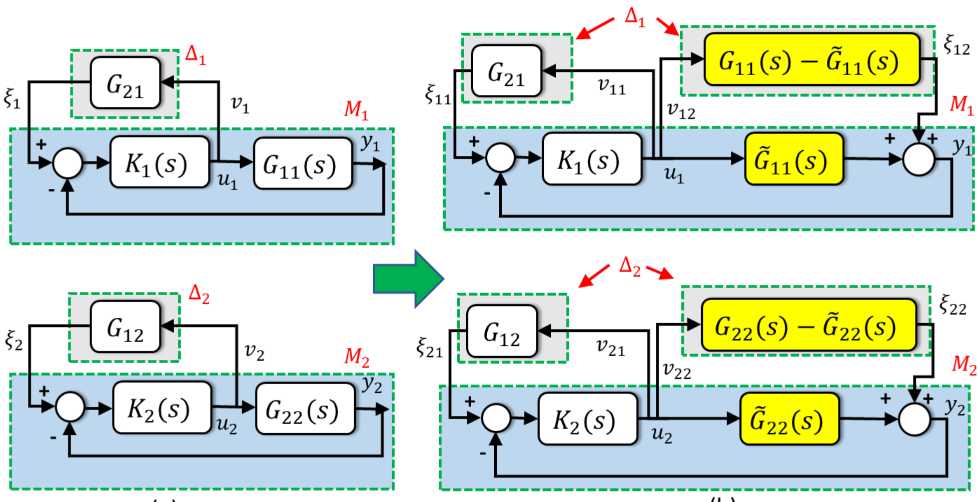

(a) (b)

Figure 6.3: Block diagram of the system structure for (a) type I robust controller requiring the exact model of G_{ii} and (b) type II robust controller requiring the exact model of $\tilde{G}_{ii}$.

The uncertainties Δ_i as well as the structure of M_i whose transfer function from ξ_i to ν_i is given in (6.11)-(6.12) are shown in Fig. 6.3a.

Based on Fig. 6.3a, the exact model of transfer function matrix G_{ii} is required for the design of controllers. In order to preserve the design confidentiality and to enable the control design for the uncoupled transfer function $\tilde{G}$, the type I robust control defined earlier is transformed into another design problem (type II), where all the transfer functions that depend on an adjacent converter are incorporated in the uncertainty blocks. Fig. 6.3b is another representation of Fig. 6.3a, where G_{ii} is decomposed into two transfer functions: I) $G_{ii} - \tilde{G}_{ii}$ that is considered as an uncertainty, and II) $\tilde{G}_{ii}$, which forms the main transfer function included in M_i. Since the proposed controller design of this chapter is based on the H_∞ approach, the exact models of G_{ij} and $G_{ii} - \tilde{G}_{ii}$ transfer functions, which are associated with the coupling dynamics, are not needed. Reduced-order models of G_{ij} and $G_{ii} - \tilde{G}_{ii}$ transfer functions that do not rely on detailed system models are used in the proposed controller design approach preventing the violation of design confidentiality.

The proposed controller design ensures the interconnected system stability in the presence of all uncertainties Δ_i with an H_∞ norm similar to that of the reduced-order transfer functions associated with adjacent converters. Thus, the individual design of the converter controllers does not require the exact model of the interconnected converter system and only requires the exact model of transfer function matrices $\tilde{G}_{ii}$. This design method also

Table 6.1: Parameters of the test system

Quantity	Value	Description
P	200 MW	Active power of each VSC
V_{dc}	400 KV	DC voltage
V_s	230 KV	AC grid RMS voltage
f	60	Frequency
L	0.0291 H	Transformer+ transmission line inductance
L_f	0.0725 H	Filter inductance
C_{dc}	300 μ F	DC side capacitance

handles the system parametric uncertainties in addition to the interactions, because the reduced-order models of the coupling dynamics in the uncertainty blocks, which are primarily used to ensure design confidentiality, also account for a range of parametric uncertainties in the system model.

6.4 Simulation Results

This section aims at verifying the effectiveness of the controller design method using time-domain simulations. The model of two converters sharing a common PCC with the parameters given in Table 6.1 is built in MATLAB/SIMULINK and used for simulations. Unless it is stated otherwise, SCR=2.5.

Only H_∞ controllers designed for the VSCs operating in the DC voltage/AC voltage control mode are provided in this chapter as this control mode results in the largest interactions between the converters compared to the other control modes [19]. In the proposed design process, the reduced-order model of Δ_i is used instead of its exact model as it is assumed that the exact model of the coupling dynamics between the converters is not available. As explained earlier in (6.3), any reduced-order model of Δ_i with a similar H_∞ norm to that of the exact model can be used in the design of individual controllers. Fig. 6.4 compares the singular values of the exact model and the reduced-order model of the uncertainty blocks of Fig 6.3. As Fig. 6.4 shows, the largest singular value of the reduced-order models is equal to or greater than that of the exact models. As H_∞ norm of a transfer function is the maximum of the largest singular values of that transfer function over all frequencies, the H_∞ norm of the reduced-order uncertainty is similar to that of the exact model according to Fig. 6.4. Thus, the reduced-order models of uncertainty blocks, which are associated with the coupling dynamics, are appropriate alternatives for the exact models.

To assess the efficiency of the proposed controller design approach, the outer controllers of VSCs designed based on the robust control scheme shown in Fig. 3b are compared against those designed based on the robust control scheme depicted in Fig. 3a. The former only requires the exact model of $\tilde{G}_{ii}$, while the latter requires the exact model of G_{ii}. Fig. 6.5 shows the eigenvalues of the closed-loop system with the two aforementioned robust controllers. As the eigenvalues' location indicates, the interconnected system is stabilized when the proposed controllers are employed. Furthermore, the dominant eigenvalues of the interconnected closed-loop system with both types of robust controllers are almost the same. Fig. 6.6 shows the transient response of VSCs when the designed robust controllers are employed. The time-domain responses clearly show that the individual design of controllers using the proposed method performs satisfactorily in the interconnected system, although an exact model of coupling dynamics is not used in the design. While both type I and type II controllers work satisfactorily, controller type II is superior to type I as it only requires the exact model of VSC_i, i.e., it employs the exact model of the uncoupled transfer function matrix $\bar{G}(s)$.

To show the robustness of the designed H_∞ controllers to parameter variations, time-

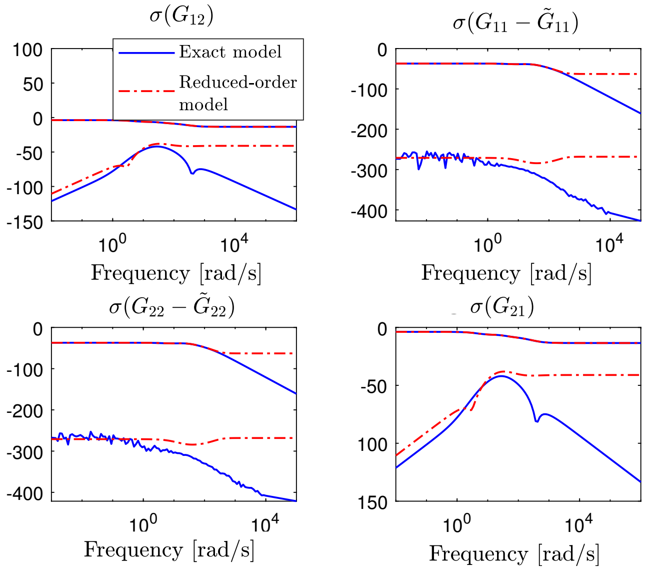

Figure 6.4: Singular values of the exact and reduced-order model of Δ_i.

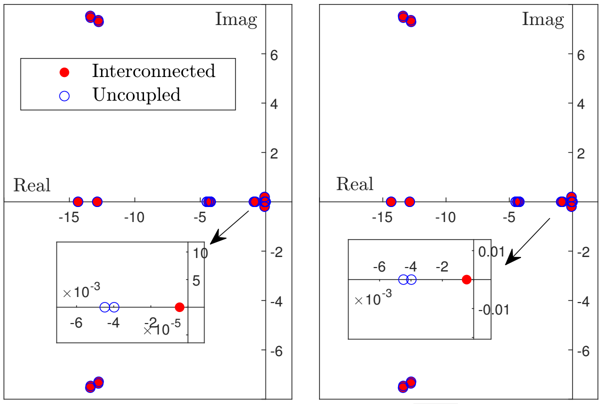

(a)

(b)

Figure 6.5: Dominant closed-loop system eigenvalues with (a) type I robust controller and (b) type II robust controller.

domain control outputs of VSC_1 and VSC_2 for a 10% change in the set-points of DC and AC voltages and for three SCRs are shown in Fig. 6.7. In these figures, SCR is varied as it is the most important system parameter impacting the interactions [18, 19].

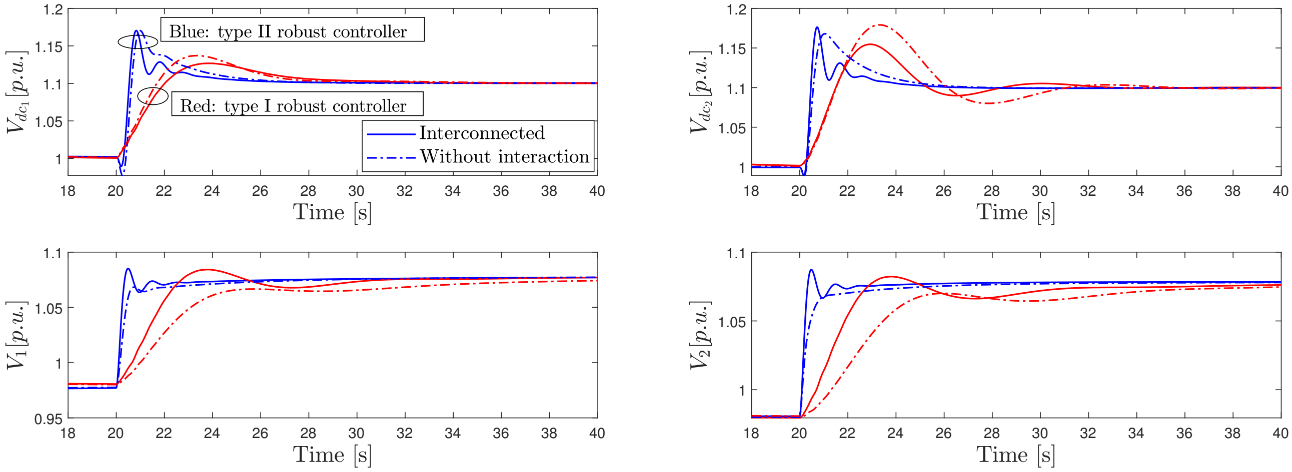

Figure 6.6: Time-domain control outputs of VSC_1 and VSC_2 for a 10% change in the set-points of DC voltage and AC voltage.

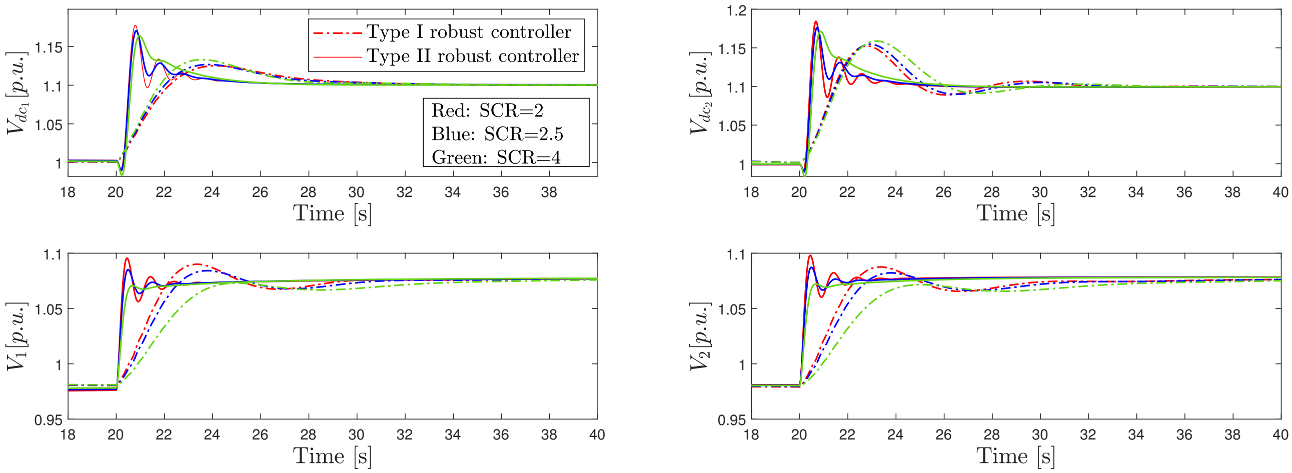

Figure 6.7: Time-domain control outputs of VSC_1 and VSC_2 for a 10% change in the set-points of DC and AC voltages and for various SCRs.

As demonstrated in Fig. 6.7, the transient response of the VSCs with the designed H_∞ controllers is satisfactory with variations in SCR, verifying the robustness of the proposed controllers with respect to parametric uncertainties.

6.5 Conclusion

This chapter focused on the external control loop interactions among the converters sharing the same AC system. A controller design method for mitigating the negative impact of these interactions on multi-VSC systems' stability was developed. The proposed robust H_∞ controllers are designed individually such that they stabilize the multi-VSC system. The individual tuning of the controllers makes the multi-vendor realization of the multi-VSC system possible. The developed method also takes the confidentiality of the design into account, as only the exact model of individual VSCs and a reduced-order model of coupling dynamics are required in the design of the controllers. It was also shown that the developed controller design approach is robust to system parameter variations.

Chapter 7

Mitigating AC Side External Control Loop Interactions in Multi-Vendor Multi-VSC Systems: Grid Integrator Viewpoint

7.1 Introduction

Connecting multiple voltage-sourced converters (VSCs) built by various vendors to a shared point of common coupling (PCC) results in various control challenges due to the interactions among the converters, which may lead to the interconnected converters' response deviating from the desired one. Although the individual converters with independently designed controllers may be stable, their connection to a PCC may cause system instability [79].

This chapter tackles the model confidentiality of converters and focuses on mitigating the interactions to integrate VSCs with independently designed controllers into an interconnected multi-VSC system, where the converters are connected to a single PCC. The developed method uses the transfer function models of the converters in the direct quadrature (dq)-frame, the controllers of which are designed independently based on vendor-specific models (thereby complying with confidentiality requirements) to design two interaction filters (IFs). One IF is added to the d-axis loop and another one is placed in the q-axis loop, to filter the measurements entering the converter controllers. The filters are obtained through solving an H_∞ minimization problem such that the multi-VSC system is stabilized, and its dynamic behavior closely matches the desired response of the individual converters with independently designed controllers. Such a design will significantly reduce the negative impact of interactions on the dynamic behavior of interconnected converters and will not create new disruptive interactions, because the coupling dynamics among the converters are considered in designing the IFs. In addition, this chapter analytically proves that the developed IFs increase the robust stability margin of the multi-VSC system. The simulation studies performed on the nonlinear model of an interconnected 2-VSC system demonstrate the effectiveness of the developed IFs in reducing the interactions among converters and improving the robust stability of the interconnected system.

7.2 System Model Requirements

Fig. 7.1 shows a schematic diagram of multiple VSCs sharing a PCC (multi-VSC system) as well as the internal structure of the control system associated with VSC_k. In a multi-VSC system, the converters are not necessarily in close proximity, and they can be located at far distances. The impedance between the terminal of each converter and the PCC (R_k, X_k) in Fig. 7.1a corresponds to that distance. Although the schematic in Fig. 7.1a is a general configuration considered in the literature [45, 55, 79], the formulation presented in this section can be extended to any arbitrary topology with multiple converters connected to a common PCC such as that of Fig. 7.1b.

In this section, first, the averaged dynamic model of the multi-VSC system shown in Fig. 7.1a is presented in the dq-frame, and the transfer function model of the multi-VSC system is obtained. Then, the specific converter models used by each vendor for designing the converters' controllers are discussed. Finally, the required information for the multi-vendor realization of a multi-VSC system is presented.

7.2.1 Averaged-Model of VSCs Connected to a Shared PCC

Based on Fig. 7.1a, the space-phasor representation of the current-voltage dynamics at the AC side of the converters is given by

$$R_{f_k}\overrightarrow{i}_k + L_{f_k}\frac{\mathrm{d}\overrightarrow{i}_k}{\mathrm{d}t} = \overrightarrow{V}_{t_k} - \overrightarrow{V}_k, \tag{7.1}$$

$$R_k\overrightarrow{i}_k + L_k\frac{\mathrm{d}\overrightarrow{i}_k}{\mathrm{d}t} = \overrightarrow{V}_k - \overrightarrow{V}_{pcc}, \tag{7.2}$$

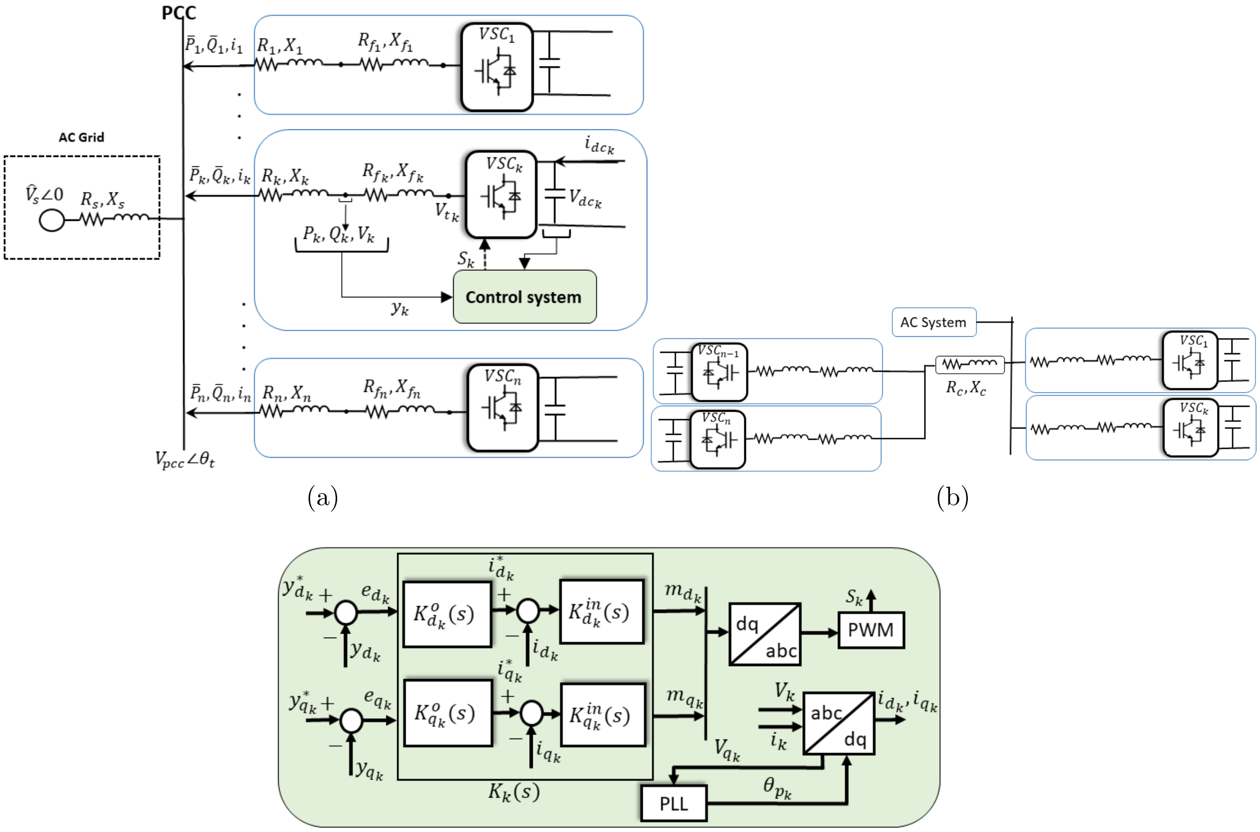

(a) (b)

(c)

Figure 7.1: (a) Schematic diagram of parallel VSCs, (b) an alternative multi-VSC system configuration, and (c) each VSC's controller.

$$R_s \sum_{j=1}^{n} \vec{i}_j + L_s \sum_{j=1}^{n} \frac{\mathrm{d}\,\vec{i}_j}{\mathrm{d}t} = \vec{V}_{pcc} - \vec{V}_s. \tag{7.3}$$

Obtaining the derivative of current from (7.2) and substituting it into (7.3) results in

$$\underbrace{[1 + \sum_{j=1}^{n} \frac{L_s}{L_j}]}_{C_v} \vec{V}_{pcc} = \vec{V}_s + R_s \sum_{j=1}^{n} \vec{i}_j + L_s \sum_{j=1}^{n} \frac{\vec{V}_j - R_j \vec{i}_j}{L_j}. \tag{7.4}$$

Similarly, substituting for the derivative of current in (7.2) from (7.1) leads to:

$$[1 + \frac{L_k}{L_{f_k}}]\vec{V}_k = \vec{V}_{pcc} + R_k \vec{i}_k + \frac{L_k}{L_{f_k}}[\vec{V}_{t_k} - R_{f_k} \vec{i}_k]. \tag{7.5}$$

To find the AC voltage of VSC$_k$, $\overrightarrow{V}_{pcc}$ in (7.5) is replaced by that in (7.4), which results in

$$\begin{aligned}\underbrace{[1+\frac{L_k}{L_{f_k}}-\frac{1}{C_v}\frac{L_s}{L_k}]}_{\bar{C}_v}\overrightarrow{V}_k &= \frac{1}{C_v}[\overrightarrow{V}_s + R_s\sum_{j=1}^{n}\overrightarrow{i}_j] + (R_k - R_{f_k}\frac{L_k}{L_{f_k}} - R_k\frac{1}{C_v}\frac{L_s}{L_k})\overrightarrow{i}_k \\ &+ \frac{L_k}{L_{f_k}}\overrightarrow{V}_{t_k} + \frac{L_s}{C_v}\sum_{j=1,j\neq k}^{n}\frac{\overrightarrow{V}_j - R_j\overrightarrow{i}_j}{L_j}.\end{aligned} \tag{7.6}$$

Equation (7.6) can be decomposed into the d and q axis components using

$$\overrightarrow{V}_k = (V_{d_k} + jV_{q_k})e^{j\theta_{p_k}}; \quad k = \{1, 2, ..n\}, \tag{7.7}$$

and will result in

$$\begin{aligned}V_{d_k} = \frac{1}{\bar{C}_v}\Bigg[&\frac{\hat{V}_s}{C_v}cos\theta_{p_k} + [R_k - L_k\frac{R_{f_k}}{L_{f_k}} + \frac{1}{C_v}(R_s - L_s\frac{R_k}{L_k})]i_{d_k} \\ &+ \frac{L_k}{L_{f_k}}V_{t_{d_k}} + \underbrace{\frac{1}{C_v}\sum_{j=1,j\neq k}^{n}\Bigg(R_s(i_{d_j}cos\theta_{p_kp_j} + i_{q_j}sin\theta_{p_kp_j}) + L_s\frac{[V_{d_j} - R_j i_{d_j}]cos\theta_{p_kp_j} + [V_{q_j} - R_j i_{q_j}]sin\theta_{p_kp_j}}{L_j}\Bigg)}_{C_{d,k}}\Bigg],\end{aligned} \tag{7.8}$$

$$\begin{aligned}V_{q_k} = \frac{1}{\bar{C}_v}\Bigg[&\frac{-\hat{V}_s}{C_v}sin\theta_{p_k} + [R_k - L_k\frac{R_{f_k}}{L_{f_k}} + \frac{1}{C_v}(R_s - L_s\frac{R_k}{L_k})]i_{q_k} \\ &+ \frac{L_k}{L_{f_k}}V_{t_{q_k}} + \underbrace{\frac{1}{C_v}\sum_{j=1,j\neq k}^{n}\Bigg(R_s(i_{q_j}cos\theta_{p_kp_j} - i_{d_j}sin\theta_{p_kp_j}) + L_s\frac{[V_{q_j} - R_j i_{q_j}]cos\theta_{p_kp_j} - [V_{d_j} - R_j i_{d_j}]sin\theta_{p_kp_j}}{L_j}\Bigg)}_{C_{q,k}}\Bigg].\end{aligned} \tag{7.9}$$

In (7.9), $\hat{V}_s$, X_s, and R_s are respectively the voltage magnitude, reactance, and resistance of the AC system; i_k is the alternating current (AC) line current of VSC_k; R_{f_k} (X_{f_k})

and R_k (X_k) are respectively the resistance (reactance) of the VSCs' filters and the total resistance (reactance) of the transformer and the transmission line connecting each VSC to the PCC; and $\theta_{p_j p_k} = \theta_{p_j} - \theta_{p_k}$. (7.9) shows the general representation of the current-voltage dynamics for the multi-VSC system shown in Fig. 7.1a. For 2-level (or 3-level) VSCs, $V_{t_{dq_k}}$ is given by [86]

$$V_{t_{dq_k}}(t) = \frac{V_{dc_k}}{2} m_{dq}(t) \tag{7.10}$$

where m_d and m_q are the modulation signals generated by controllers. For converters utilizing an inner-outer control scheme with inner decoupling terms [86], (7.8)-(7.9) will have a simpler form. Using (7.8)-(7.9), the active and reactive powers at the terminal of each converter are then obtained by

$$\begin{cases} P_k = V_{d_k} i_{d_k} + V_{q_k} i_{q_k}, \\ Q_k = -V_{d_k} i_{q_k} + V_{q_k} i_{d_k}. \end{cases} \tag{7.11}$$

Assuming a negligible converter loss, the dynamic of the DC voltage is given by

$$C_k \frac{\mathrm{d}V_{dc_k}}{\mathrm{d}t} = i_{dc_k} - \frac{P_k}{V_{dc_k}}. \tag{7.12}$$

7.2.2 Interconnected Multi-VSC System Model

According to (7.8)-(7.9), the adjacent converters interact with one another through different variables. The coupling terms $C_{d,k}$ and $C_{q,k}$ in (7.8)-(7.9) indicate how the variables of adjacent converters impact one another. Considering the coupling terms, the multi-VSC system transfer function matrix is given by

$$\underbrace{\begin{bmatrix} y_1 \\ y_2 \\ . \\ y_n \end{bmatrix}}_{y} = \underbrace{\begin{bmatrix} G_{11}(s) & G_{12}(s) & . & . & . & . & G_{1n}(s) \\ G_{21}(s) & G_{22}(s) & . & . & . & . & G_{2n}(s) \\ . & . & . & . & . & . & . \\ G_{n1}(s) & G_{n2}(s) & . & . & . & . & G_{nn}(s) \end{bmatrix}}_{G(s)} \underbrace{\begin{bmatrix} m_1 \\ m_2 \\ . \\ m_n \end{bmatrix}}_{m}, \tag{7.13}$$

where $y_k = [y_{d_k}, y_{q_k}]$ and $m_k = [m_{d_k}, m_{q_k}]$. $G(s)$ is the interconnected multi-VSC system transfer function (ISTF).

7.2.3 Vendor-Specific Models

Confidentiality is an important aspect of the multi-vendor realization of power systems in which the vendors' proprietary information is protected and not shared with other suppliers [64]. Therefore, a third-party (grid integrator) is required to facilitate the coordination among different manufacturers and perform the necessary assessments to ensure the reliable performance of the multi-VSC system [64]. In such assessments, the detailed dynamic models of adjacent converter stations are not available to the grid integrator or supplier k because of confidentiality concerns. To address the confidentiality in this chapter, it is assumed that the shared information among the vendors is the grid impedance (X_s), frequency (f), and Thevenin equivalent grid voltage (V_s) as well as the active/reactive power set-points of adjacent converters. Therefore, from the viewpoint of VSC_k, the adjacent converters are treated as constant loads as the transient response of the adjacent converters remains unpredictable due to restricted access to the corresponding dynamic models.

Each vendor uses an exclusive vendor-specific transfer function (VSTF) model to design its corresponding controller $K_k(s)$. It is assumed that the VSTF model of VSC_k is denoted as $\tilde{G}_{kk}$, and it represents the relationship between the modulation signals and controlled outputs of VSC_k:

$$\begin{bmatrix} y_{d_k} & y_{q_k} \end{bmatrix}^T = \underbrace{\tilde{G}_{kk}(s)}_{2\times 2} \begin{bmatrix} m_{d_k} & m_{q_k} \end{bmatrix}^T . \tag{7.14}$$

The transfer function matrix associated with all VSTFs is denoted as

$$\tilde{G}(s) = \mathrm{diag}(\tilde{G}_{11}(s), \tilde{G}_{22}(s), ..., \tilde{G}_{nn}(s))_{2n\times 2n}, \tag{7.15}$$

and the transfer function matrix associated with the corresponding controllers is given by

$$K(s) = \mathrm{diag}(K_1(s), K_2(s), ..., K_n(s))_{2n\times 2n}, \tag{7.16}$$

where n is the number of converters. It should be noted that $G(s)$ in (7.13) and $\tilde{G}_{kk}(s)$ in (7.15) are different in two ways: I) $\tilde{G}_{kk}(s)$ is exclusive to each vendor, and II) in the computation of $\tilde{G}_{kk}(s)$, the adjacent converters are treated as constant loads and thus the coupling terms are neglected. Furthermore, $\tilde{G}(s)$ is a block diagonal matrix, while $G(s)$ is a dense matrix.

In this chapter, the controllers are designed using the inner-outer cascaded control scheme shown in Fig. 7.1c. In this scheme, the controlled outputs (y_{d_k} and y_{q_k}) are regulated by the outer control loops, and the AC lines' currents are controlled by the inner loops to provide the modulation signals (m_{d_k} and m_{q_k}). The gains of the inner control loops are set based on the system parameters [86]. The outer controllers of each VSC are designed based on the transient response specifications of the corresponding VSC and without considering the transient response of other VSCs; thereby complying with confidentiality requirements. Because controller $K_k(s)$ is designed for $\tilde{G}_{kk}(s)$, employing such a controller in a multi-VSC system should be carried out with caution as it may result in the instability of the interconnected system. This will be demonstrated in Section 7.3.

7.2.4 Required Information to Integrate the Converters into an Interconnected System

To integrate multiple converters from different manufacturers with unique designs into the power grid and reliably operate the interconnected multi-VSC system, certain information from manufacturers needs to be shared with the grid integrator, namely I) $\tilde{G}_{kk}(s)$, II) $K_k(s)$, and III) the transfer function associated with PLL (from V_{q_k} to θ_{p_k}). Since each transfer function has several realizations, sharing these transfer function models with the grid integrator does not reveal sensitive information about the converter model and does not violate confidentiality requirements. $K_k(s)$ is shared with the grid-integrator as a black-box model without revealing its detailed formulation. Having black-box models without disclosing the internal structure of the control system is the least requirement for the successful realization of multi-vendor AC-DC systems [64].

7.3 Stability and Performance of Multi-VSC Systems with Independently Designed Controllers

In this section, the impact of independently designed controllers on the stability and dynamic performance of the interconnected multi-VSC system is investigated.

Fig. 7.2a shows the vendor-specific loop of VSC_k, including the VSTFs and their independently designed controllers. The independently designed controllers K_1 and K_2 are such that the closed-loop systems in Fig. 7.2a are stable and provide an acceptable dynamic performance. Fig. 7.2b shows the closed-loop control system for the 2-VSC system, in which the controllers are those of Fig. 7.2a. It should be noted that the transfer functions in Fig. 7.2a are the VSTFs, while that in Fig. 7.2b is the ISTF. Since ISTF is not available for the design of controllers, the coupling dynamics among the converters are not considered in the independent design of controllers K_1 and K_2. Therefore, the

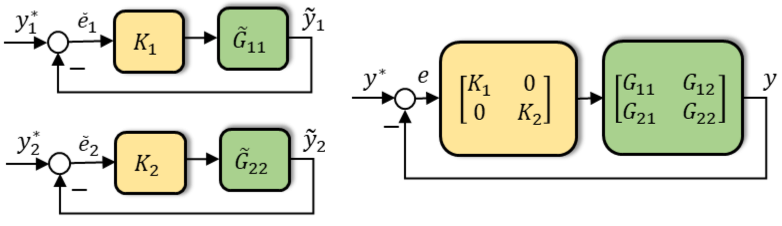

(a) (b)

Figure 7.2: (a) Vendor-specific loop of VSC_k and (b) the interconnected 2-VSC system with independently designed controllers from (a).

stability and dynamic performance of the system in Fig. 7.2b is not guaranteed and must be evaluated.

Although any vendor-specific model can be selected, for the studies of this chapter, the converter transfer functions $\tilde{G}_{kk}$ obtained from (7.1)-(7.9) are used. To obtain $\tilde{G}_{kk}$ from (7.1)-(7.9), $L_j, j \neq k$ is set to ∞ to decouple the dynamics of adjacent converters from VSC_k. In this case, the terms $C_{d,k}$ and C_{q_k} disappear from (7.8)-(7.9). It should be noted that the generality of the method presented later is not limited to the employed vendor-specific model, i.e., $\tilde{G}_{kk}$.

It is worth mentioning that the conclusions and discussions provided in this chapter regarding a 2-VSC system are expandable to a multi-VSC system. Furthermore, the analysis can be generalized to all control modes, and those selected in the case studies are only for illustration purposes. The system parameters for numerical illustrations are given in Table 7.1.

7.3.1 Illustrative Examples

Two examples are provided to demonstrate the stability and performance of an interconnected 2-VSC system, for which the VSC controllers are independently designed. Table 7.2 includes the sets of outer controller gains for these two examples. The control parameters of the inner current loops are set as $K_p = \frac{L_f}{\tau}, K_I = \frac{R_f}{\tau}$ [86].

To illustrate the impact of interactions on the VSCs' dynamic response for the first set of controller gains, a 5% step change is applied to the reference signal of VSCs' controllers. The responses of VSTFs in Fig. 7.2a and VSCs in the interconnected 2-VSC system in Fig. 7.2b are compared against each other in Fig. 7.3. Fig. 7.3 demonstrates how the integration of independently designed controllers into an interconnected 2-VSC system

Table 7.1: Parameters of the test system [5]

Quantity	Value	Description
P	200 MW	Active power
V_{dc}	400 KV	DC voltage
V_s	230 KV	AC grid RMS voltage
f	60	Frequency
L	0.0291 H	Transformer plus transmission line inductance
L_f	0.0725 H	Filter inductance
R_f	0.005 Ω	filter and switches on-state resistance
C_{dc}	300 μ F	DC side capacitance
τ	2 ms	Inner current loop time constant
SCR	1.5	AC system short circuit ratio
K_p^{pll}, K_I^{pll}	50,716	Proportional and integral gains of PLL

distorts the dynamic behavior of VSCs from the desired behavior for which the controllers were tuned.

The second example, in which the second set of controller gains from Table 7.2 are considered, demonstrates that the integration of independently designed converter controllers

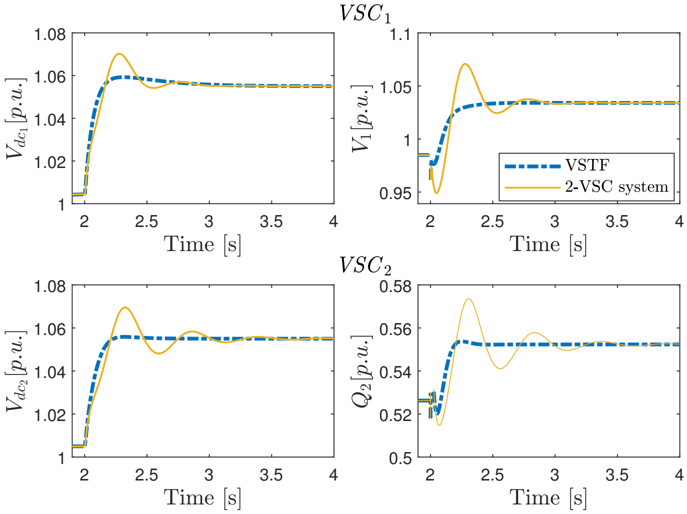

Figure 7.3: The response of VSCs to a 5% step change in the reference signal of control loops (with controller gains set #1).

Table 7.2: Set of controller gains for numerical illustrations

	VSC_1	VSC_2
Controller Gains Set #1	$K^o_{d_1} = 2.875 + \frac{10.76}{s}$ $K^o_{q_1} = 0.0034 + \frac{17.67}{s}$	$K^o_{d_2} = 2.115 + \frac{16.92}{s}$ $K^o_{q_2} = \frac{9.634}{s}$
Controller Gains Set #2	$K^o_{d_1} = 10.7 + \frac{120.2}{s}$ $K^o_{q_1} = 0.5 + \frac{40}{s}$	$K^o_{d_2} = 2.23 + \frac{100}{s}$ $K^o_{q_2} = \frac{30}{s}$

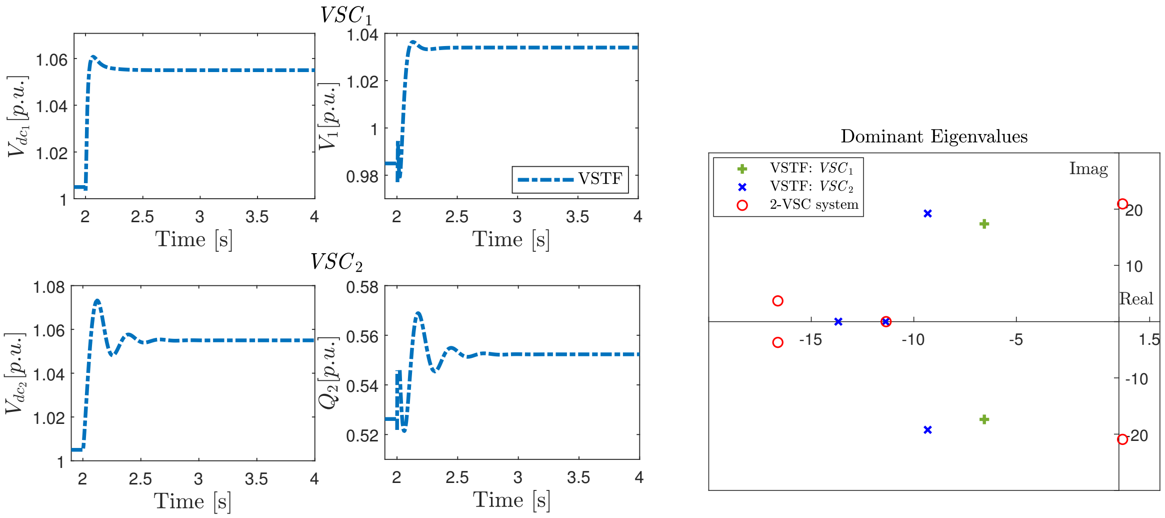

(a)

(b)

Figure 7.4: (a) The response of VSCs to a 5% step change in the reference signal of control loops (with controller gains set #2) and (b) eigenvalue map of the individual VSCs and the interconnected system.

into the 2-VSC system may cause closed-loop instability. Fig. 7.4a shows the response of VSCs in Fig. 7.2a to a 5% step change in the reference inputs. The time-domain response of the closed-loop 2-VSC system is not shown due to instability. Fig. 7.4b shows the eigenvalue map for the closed-loop systems of Fig. 7.2a and Fig. 7.2b with the second set of controller gains. As Fig. 7.4b indicates, although all the eigenvalues associated with the VSTFs lie in the left-half plane (LHP), the interconnected 2-VSC system is unstable.

These two examples illustrate that forming a multi-VSC system from converters whose controllers are designed independently may result in interconnected system instability or unacceptable dynamic performance.

7.3.2 Dynamic Response of an Interconnected Multi-VSC System with Independently Designed Converter Controllers

The coupling dynamics $C_{d,k}$ and $C_{q,k}$ make the dynamic performance of the multi-VSC system with independently designed controllers deviate from that of the individual converters. The relative difference between VSTFs and ISTF can be formulated as [75]

$$E = (G - \tilde{G})\tilde{G}^{-1}, \tag{7.17}$$

and the relationship between the sensitivity functions of VSTFs and ISTF is given by

$$S = \tilde{S}(I + E\tilde{T})^{-1}, \tag{7.18}$$

where $\tilde{S}$ (S) is the closed-loop transfer function from y^* to $\tilde{e}$ (e) in Fig. 7.2 and $\tilde{T} = I - \tilde{S}$. (7.18) is indicative of the sensitivity of the multi-VSC system dynamics to the differences between VSTFs and ISTF. The reader is referred to [75] for the derivation of (7.18).

According to (7.18), the sensitivity function associated with the ISTF deviates from that of the VSTFs by $(I+E\tilde{T})^{-1}$. If $(I+E\tilde{T})^{-1}$ is close to I (identity matrix), $S \approx \tilde{S}$, and consequently, each converter in the multi-VSC system behaves similarly to the dynamic response of individual converters. Moreover, in terms of stability, it can be verified that [75]

$$det(I + GK) = det(I + E\tilde{T})det(I + \tilde{G}K), \tag{7.19}$$

where $det(I + E\tilde{T})$ relates the characteristic polynomial of the ISTF to that of the VSTFs. Because the individually designed controllers stabilize VSTFs, all the roots of $det(I + \tilde{G}K)$ are in the LHP. Thus, the interconnected multi-VSC system with the employment of independently designed controllers is stable if and only if all the roots of $det(I + E\tilde{T})$ are in the LHP [75]. Therefore, according to (7.18) and (7.19), the term $(I + E\tilde{T})^{-1}$ is a decisive transfer function impacting both the stability and performance of the multi-VSC system. If $(I + E\tilde{T})^{-1}$ is stable, the stability of the multi-VSC system is ensured, and if it is close to the identity matrix, the detrimental impact of interactions on the dynamic performance of the multi-VSC system is minimized.

7.4 Interaction Filters for Integrating the VSCs with Independently Designed Controllers into a Multi-VSC System

According to Section 7.3, it is desirable to have a stable $(I + E\tilde{T})^{-1}$ close to the identity matrix ($(I + E\tilde{T})^{-1} \approx I$) to both ensure stability based on (7.19) and reduce the negative impact of interactions on the multi-VSC system's dynamic performance based on (7.18). To achieve this objective, an IF is added to the ISTF G as follows:

$$\bar{G} = \bar{K}G, \tag{7.20}$$

where $\bar{K}$ is a block-diagonal transfer function matrix of size $2n$ with 2×2 blocks as

$$\bar{K} = \mathrm{diag}(\bar{K}_1, \bar{K}_2, ..., \bar{K}_n). \tag{7.21}$$

As shown in the modified control system in Fig. 7.5b, $\bar{K}_k$ is placed in the feedback path of the closed-loop control system of VSC_k to filter the converter outputs. Although $\bar{K}_k$ is placed in the control system, it is not called a controller and is called a filter, because it is placed in the loop such that it filters the control outputs before entering the control system. It also does not change the structure of the control system. To minimize the deviation of the dynamic response of ISTF from VSTFs, $\bar{K}$ should be determined such that

$$S \approx \tilde{S}. \tag{7.22}$$

Using (7.18), (7.22) leads to the minimization problem

$$\gamma = \min_{\bar{K}} \quad ||S - \tilde{S}||_\infty = \min_{\bar{K}} ||\tilde{S}(I + \bar{E}\tilde{T})^{-1} - \tilde{S}||_\infty. \tag{7.23}$$

Since $\tilde{S}$ is a fixed matrix, (7.23) is equivalent to

$$\gamma = \min_{\bar{K}} \quad ||\underbrace{I - (I + \bar{E}\tilde{T})^{-1}}_{G_f}||_\infty, \tag{7.24}$$

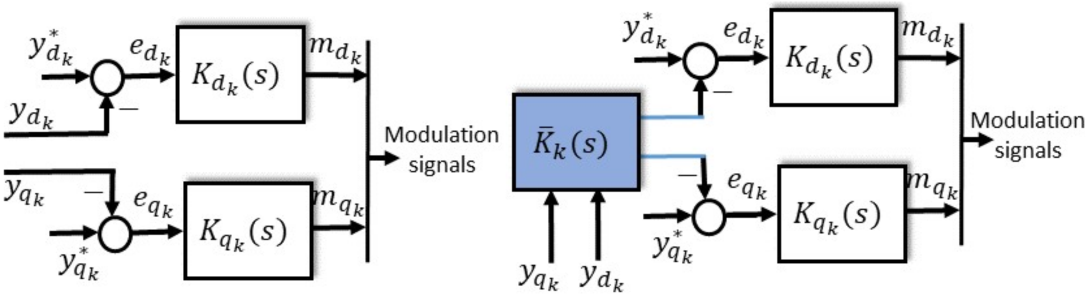

(a) (b)

Figure 7.5: (a) Original cascaded control system of VSC_k and (b) the modified control system with IFs for mitigating the interactions.

where $\bar{E} = (\bar{G} - \tilde{G})\tilde{G}^{-1}$. The rationale behind minimizing the H_∞ norm in (7.24) (rather than any other norm) is to minimize the highest impact of interactions on the dynamic behavior of ISTF. As a result of reducing the peak of the largest singular value of G_f in (7.24), i.e., $||G_f||_\infty$, the largest singular values of G_f in all other frequencies will be reduced. If γ is small enough, the deviation of the dynamic behavior of the multi-VSC system from that designed by vendors will not be significant. Additionally, any $\bar{K}$ obtained from solving (7.24) stabilizes G_f because H_∞ norm is only defined for stable transfer functions [96]. Since G_f stability ensures $(I + \bar{E}\tilde{T})^{-1}$ stability, according to (7.19), $\bar{K}$ stabilizes the multi-VSC system.

To solve (7.24), it is transformed into the standard form of H_∞ controller design. To do so, G_f is assumed to be a transfer function from a fictitious input, denoted as d_f, to a fictitious output, denoted as Y_f. Fig. 7.6a shows the forming loop of G_f and the signals d_f and Y_f. Fig. 7.6b shows an equivalent diagram to that of Fig. 7.6a with rearrangement of the blocks to take $\bar{K}$ out as a separate block. Fig. 7.6c shows the standard H_∞ structure and is equivalent to Fig. 7.6b with $P(s)$ given by

$$P(s): \begin{bmatrix} Y_f \\ v_f \end{bmatrix} = \begin{bmatrix} -\tilde{G}K & (I + \tilde{G}K) \\ GK & -GK \end{bmatrix} \begin{bmatrix} d_f \\ u_f \end{bmatrix}. \tag{7.25}$$

$P(s)$ is obtained according to Fig. 7.6b, considering d_f and u_f as the inputs and Y_f and v_f as the outputs. For the given $P(s)$, which is known to the grid integrator, and a fixed structure $\bar{K}(s)$, solving (7.24) is equivalent to minimizing the H_∞ norm of the closed-loop transfer function from d_f to Y_f in Fig. 7.6c. After constructing $P(s)$, the standard H_∞ optimization problem is solved to find the filter $\bar{K}$.

Remark 0: If S is stable and $||S - \tilde{S}||_\infty$ is small enough with $\bar{K} = I$, interactions are insignificant, and the IFs are not needed. Otherwise, $\bar{K}$ needs to be obtained by solving (7.24). This criterion can be evaluated prior to designing the IFs.

Remark 1: The first element of the matrix in (7.25) may have a pole at $s = 0$ due to the integrator in K. This pole results in an undefinable H_∞ norm of the closed-loop transfer function from d_f to Y_f in Fig. 7.6c. To overcome this issue, the pole of $K(s)$ at $s = 0$ is replaced by $s = \epsilon$, where ϵ is sufficiently small [96].

Remark 2: Inserting $\bar{K}$ in the feedback path of the control system changes the unity feedback control system to a non-unity feedback system, Fig. 7.5b. To prevent $\bar{K}$ from disturbing the set-point tracking capability of the multi-VSC system, the DC-gain of $\bar{K}$ should be set to one (i.e., $\bar{K}(0) = I$). This criterion must be imposed in the minimization problem of (7.24).

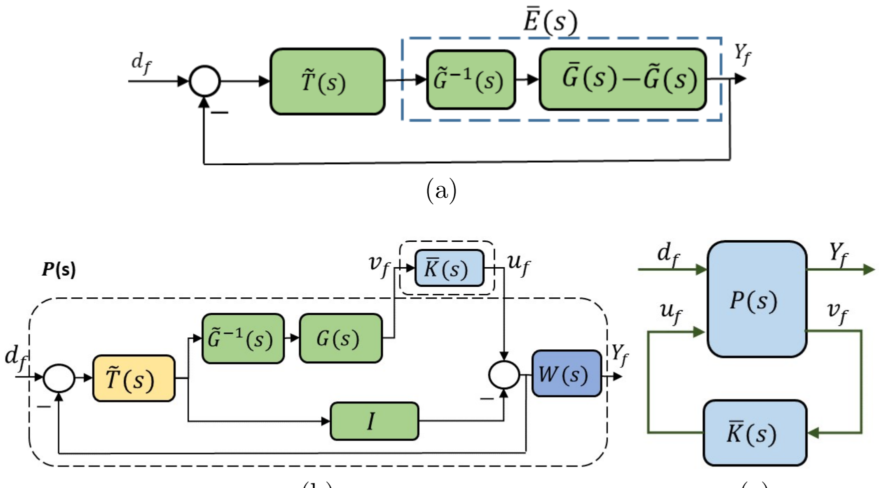

(a)

(b)

(c)

Figure 7.6: Block diagram of the fictitious loop for solving (7.24): (a) structure of the fictitious loop, (b) an equivalent block diagram showing $\bar{K}$ as a separate block, and (c) the standard representation of H_∞ optimization.

Remark 3: (7.24) allocates the same weight to all the controlled outputs of the system and minimizes the impact of interactions on all the outputs equally. If the interactions distort a specific output more than the others, a larger weight can be assigned to that output to further reduce the impact of interactions. This weighting matrix can be added as $W(s)$ in the output of Fig. 7.6b.

Remark 4: If the vendor-designed controllers K do not stabilize the multi-VSC system, solving (7.24) both stabilizes the system and minimizes the impact of interactions on the dynamic performance of converters. In scenarios where K alone stabilizes the multi-VSC system, the negative impact of interactions on the dynamic performance of the multi-VSC system can be reduced using IFs.

7.5 Robust Stability Margin of an Interconnected Multi-VSC System with Interaction Filters

In this section, it will be demonstrated that employing IFs increases the system's robust stability margin. Although the main objective of the minimization problem of (7.24) is to reduce the negative impact of interactions on the multi-VSC system's dynamics, with the SFs, the robustness of the system will be also improved. The enhanced robust stability margin of the interconnected multi-VSC system is an indirect consequence of the optimization problem. To elaborate upon the system's robustness in the presence of SFs, the stability of the perturbed system with multiplicative output uncertainty, which is shown in Fig. 7.7 is studied. The multiplicative uncertainty is one of the most common types of uncertainty, which accounts for the unforeseen dynamics and nonlinearities that are often neglected for model simplicity [96].

In the presence of multiplicative uncertainty, the multi-VSC system model becomes

$$G_{\Delta}(s) = (I + \underbrace{\delta_0\Delta_0}_{\Delta})G(s); \quad ||\Delta_0||_{\infty} < 1, \tag{7.26}$$

where Δ includes all sources of uncertainty in the system. Δ_0 is a diagonal matrix representing the structure of Δ, and δ_0 is the magnitude of Δ.

To evaluate the stability of the system in the presence of the multiplicative uncertainty, the characteristic polynomial of the perturbed closed-loop system shown in Fig. 7.7 is given by

$$det(I + \bar{K}G_{\Delta}K) = 0. \tag{7.27}$$

Expanding (7.27) and factoring $(I + \bar{K}GK)$ transform (7.27) into

$$det(I + \Delta GK(I + \bar{K}GK)^{-1}\bar{K})det(I + \bar{K}GK) = 0. \tag{7.28}$$

In (7.28), $det(I + \bar{K}GK)$ has all its roots in the LHP, as the optimization of (7.24) will result in $\bar{K}$ that stabilizes the closed-loop interconnected system. Therefore, to maintain stability of the multi-VSC system in the presence of uncertainties, the roots of $det(I + \Delta GK(I + \bar{K}GK)^{-1}\bar{K})$ must not leave the LHP for all the bounded perturbations Δ. To achieve this

$$\bar{\sigma}(\Delta T) < 1 \tag{7.29}$$

must be maintained [41,96], where $\bar{\sigma}$ is the maximum singular value of a transfer function and $T = GK(I + \bar{K}GK)^{-1}\bar{K}$. Based on (7.29), an upper-limit for perturbations for which system stability is guaranteed is given by

$$\bar{\sigma}(\Delta) < \rho^{-1}, \tag{7.30}$$

where $\rho = \max_{\omega} \mu(T)$ is given by [96]:

$$\mu(T) = \frac{1}{\min_{\Delta}\{\bar{\sigma}(\Delta)|det(I - T\Delta)\}}. \tag{7.31}$$

In (7.31), $\mu(T)$ indicates a stability margin of the closed-loop system as it corresponds to the smallest Δ (determined in terms of $\bar{\sigma}(\Delta)$) that destabilizes the interconnected system, and, based on the definition of ρ, ρ^{-1} also becomes a measure of system stability in the presence of structured perturbations. The smaller ρ^{-1} is, the smaller the robust stability margin will be. If $\rho^{-1} < 1$, there exists at least one set of perturbations that destabilizes the system [96]. Thus, to compare the robust stability margin of the system in the presence of IFs and without them, ρ^{-1} in these two cases need to be compared.

According to (7.24), the employment of the IFs minimizes $||G_f||_\infty$ and results in $(I + E\tilde{T})^{-1}$ becoming closer to the identity matrix and, according to (7.18), S being reduced. Since $T = GKS\bar{K}$, T will be reduced as S reduces. As T becomes smaller in the presence of SFs, $\mu(T)$ will intuitively become smaller. Therefore, using the IFs reduces ρ, and thus, provides a larger robust stability margin, according to (7.30). Since $\mu(T)$ does not have a closed-form and needs to be computed numerically, the impact of IFs on $\mu(T)$ will be demonstrated using simulation results in Section 7.6.

7.6 Case Studies

The simulations have been performed on the nonlinear averaged model of a 2-VSC system built in MATLAB/SIMULINK. Without loss of generality, it is assumed that VSC_1 is in the DC voltage/AC voltage control mode, and VSC_2 operates under the DC voltage/reactive power control mode. The parameters of the test system are provided in Table 7.1.

In this section, first, the impact of the IFs on the stability and dynamic response of the interconnected system is studied. Then, a robust stability analysis is performed with respect to variations in the operating point of adjacent converters to show the impact of IFs on reducing the interactions under a very low SCR (SCR=1.5). The study results are only presented for a low SCR as it corresponds to the case where the interactions among the converters are significant.

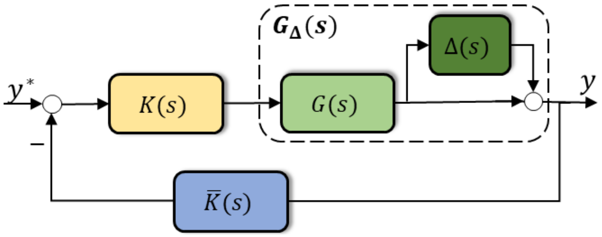

Figure 7.7: Closed-loop interconnected system with multiplicative uncertainty.

7.6.1 Case 1: Impact of IFs on the interconnected system stability

Referring to the second set of controller gains of Table 7.2 and the eigenvalue map shown in Fig. 7.4, the 2-VSC system with independently designed controllers is unstable, while

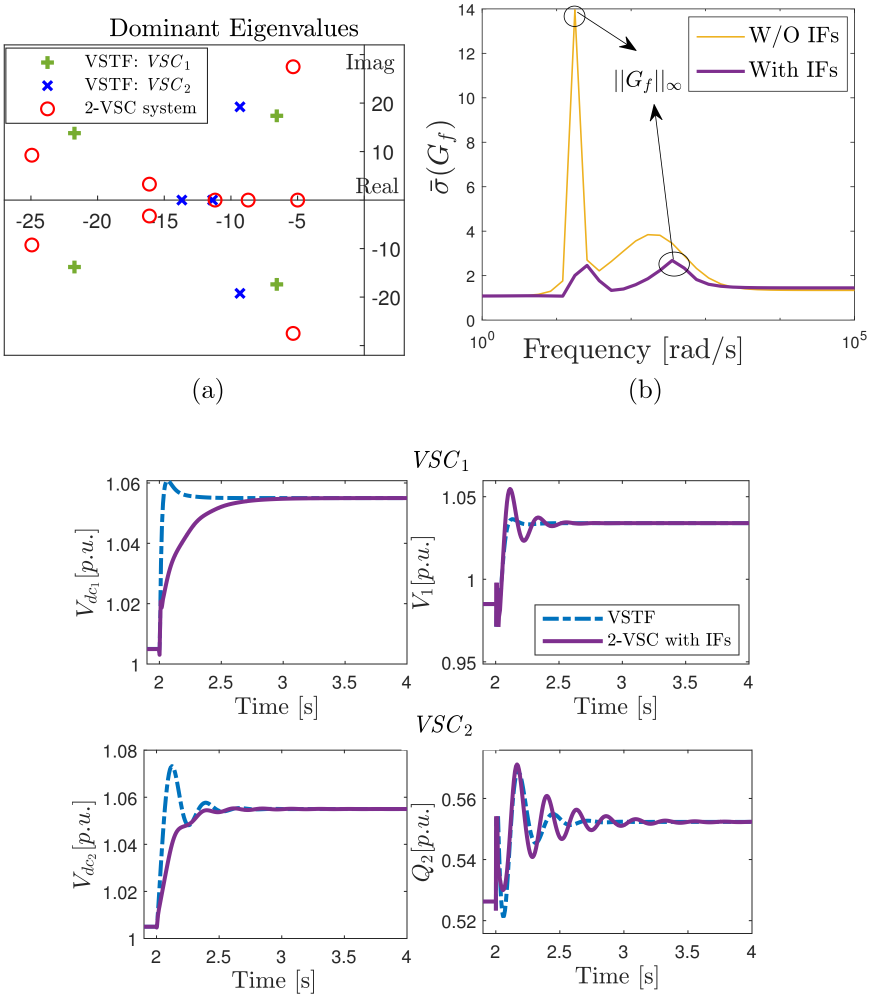

(a) (b)

(c)

Figure 7.8: The impact of IFs on the 2-VSC system stability, (a) eigenvalues map, (b) $\bar{\sigma}(G_f)$, and (c) time-domain response of the system to a 5% change in the reference inputs.

the controllers stabilize the individual converters. In this case study, the objective is to use the IFs to seamlessly integrate VSC_1 and VSC_2 to the AC system and to stabilize the 2-VSC system. To achieve this objective, (7.25) is formed, and the minimization problem of (7.24) is solved for $\bar{K}(s)$. The following filters are obtained:

$$\gamma_1 = 2.7 : \begin{cases} \bar{K}_1 = \text{diag}(\frac{4.032s+20.56}{s+20.56}, \frac{1.158s+38.08}{s+38.08}), \\ \bar{K}_2 = \text{diag}(\frac{8.917s+77.6}{s+77.6}, \frac{0.2188s+147.7}{s+147.7}). \end{cases}$$

It should be noted that the IFs that stabilize the multi-VSC system are not unique, and various IFs can be found to satisfy (7.24), and the achieved performance will consequently be different. Fig. 7.8a shows the system's dominant eigenvalues with the selected IFs. Comparing Fig. 7.8a with Fig. 7.4 shows that although the 2-VSC system with the independently designed controllers is unstable, utilizing the IFs has stabilized the system. Fig. 7.8b shows the impact of IFs on $||G_f||_\infty$ defined in (7.24). Based on Fig. 7.8b, the IFs have reduced the peak of $||G_f||_\infty$, which is indicative of the level of interactions among the converters. The large peak in $||G_f||_\infty$ occurs because G_f is unstable without the IFs. To evaluate the impact of IFs on the dynamic response of the interconnected system, Fig. 7.8c compares the response of individual and interconnected VSCs to a 5% step change in the reference input of converter controllers with and without the IFs. While the 2-VSC system without the IFs is unstable, Fig. 7.8c shows an acceptable dynamic performance in the presence of the IFs. It should be noted that the dynamic response of the 2-VSC system without the IFs is not shown in Fig. 7.8c due to the system's instability.

7.6.2 Case 2: Impact of IFs on the interconnected system dynamic response

With the first set of controller gains in Table 7.2, the VSCs maintain stability when they are connected to a shared AC system, but the dynamic behavior of the converters in the 2-VSC system differs from the individual ones, Fig. 7.3. For the first given set of controller parameters in Table 7.2, the following IFs are obtained from solving (7.24):

$$\gamma_2 = 1.35 : \begin{cases} \bar{K}_1 = \text{diag}(\frac{9.319s+182.5}{s+182.5}, \frac{1.1s+3.894}{s+3.894}), \\ \bar{K}_2 = \text{diag}(\frac{11.79s+235.6}{s+235.6}, \frac{0.8969s+6.969}{s+6.969}). \end{cases}$$

Fig. 7.9a shows $||G_f||_\infty$ with and without these IFs and verifies that with the SFs, the peak of $||G_f||_\infty$ is reduced. The smaller peak of $||G_f||_\infty$ is an indication of reduced interactions

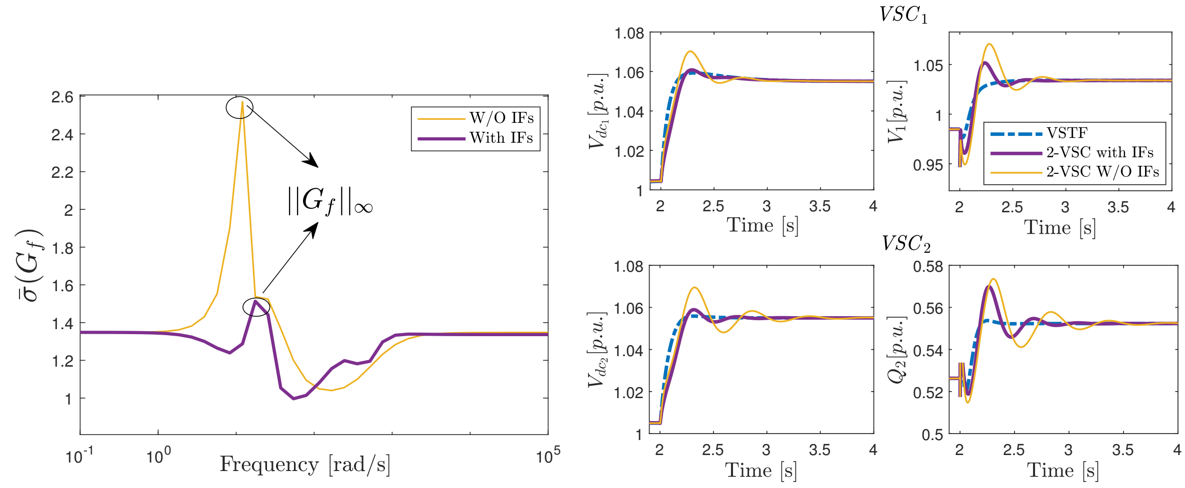

(a)

(b)

Figure 7.9: (a) $\bar{\sigma}(G_f)$ and (b) time-domain response of the system to a 5% step change in the reference inputs.

among the converters. Fig. 7.9b shows the response of the individual and interconnected VSCs to a 5% step change in reference input of the converters with and without the IFs. Fig. 7.9b confirms that the IFs have resulted in the dynamic response of the interconnected system to be closer to that of the individual converters, and thus has reduced the negative impact of interactions on the dynamic performance of the converters.

To verify the effectiveness of the IFs on improving the dynamic behavior of the converters, the interconnected system's closed-loop transfer function (T) from the set-points to the controlled outputs are computed as

$$T = \left[\begin{array}{c|c} \begin{bmatrix} T_{y_{d_1} y^*_{d_1}} & T_{y_{d_1} y^*_{q_1}} \\ T_{y_{q_1} y^*_{d_1}} & T_{y_{q_1} y^*_{q_1}} \end{bmatrix} & \begin{bmatrix} T_{y_{d_1} y^*_{d_2}} & T_{y_{d_1} y^*_{q_2}} \\ T_{y_{q_1} y^*_{d_2}} & T_{y_{q_1} y^*_{q_2}} \end{bmatrix} \\ \hline \begin{bmatrix} T_{y_{d_2} y^*_{d_1}} & T_{y_{d_2} y^*_{q_1}} \\ T_{y_{q_2} y^*_{d_1}} & T_{y_{q_2} y^*_{q_1}} \end{bmatrix} & \begin{bmatrix} T_{y_{d_2} y^*_{d_2}} & T_{y_{d_2} y^*_{q_2}} \\ T_{y_{q_2} y^*_{d_2}} & T_{y_{q_2} y^*_{q_2}} \end{bmatrix} \end{array} \right]_{4\times 4}. \tag{7.32}$$

The magnitude and phase angle of different entries of T are plotted in Figs. 7.10-7.11. The magnitude and phase angle of the block-diagonal and off-diagonal transfer functions are presented in Fig. 7.10 and Fig. 7.11, respectively. Although the phase angles of the closed-loop transfer functions with and without IFs are close to those of the VSTFs as shown in Fig. 7.10b, the magnitude of the diagonal transfer functions are closer to those of the VSTFs in the presence of IFs as shown in Fig. 7.10a. Moreover, based on Fig. 7.11, the magnitude of the off-diagonal transfer functions are smaller with the employment of SFs, indicating the effectiveness of IFs in reducing the interactions and providing a closer

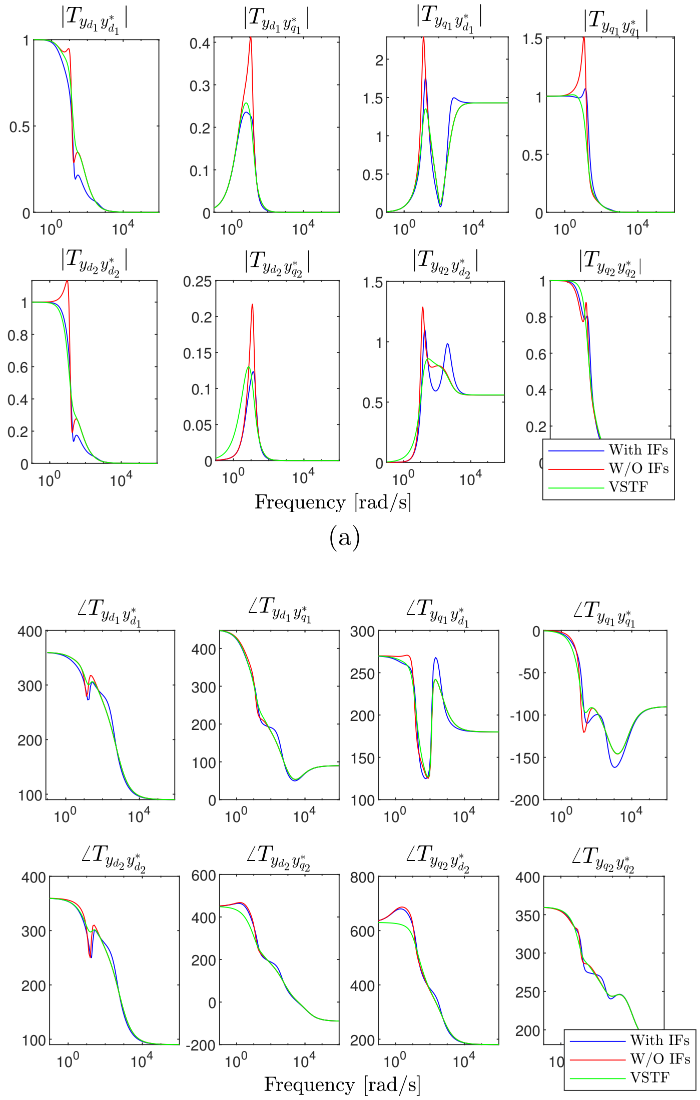

(a)

(b)

Figure 7.10: (a) Magnitude and (b) phase angle of the closed-loop block-diagonal transfer functions.

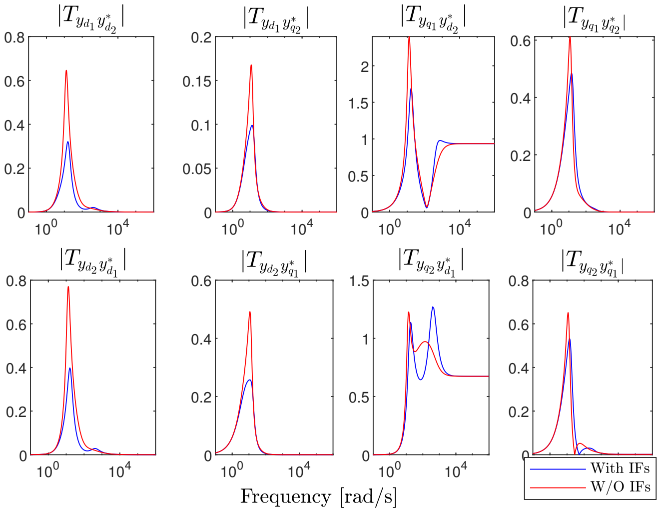

Figure 7.11: Magnitude of the closed-loop off-diagonal transfer functions.

response of the interconnected system to that of VSTFs.

7.6.3 Case 3: Impact of the IFs on the interconnected system's robust stability

To show the impact of IFs on the system's robust stability, a multiplicative uncertainty Δ with an amplitude of 0.4 ($\delta_0 = 0.4$) is considered. Δ covers a maximum of 40% change in the system model due to parametric uncertainties, perturbations in the operating point, measurement errors, and unforeseen dynamics that do not change with frequency. As the purpose of this section is to study the impact of IFs on the system's stability margin, the simplest form of uncertainty is considered in the simulations. The simulations in this section are performed based on the first set of controller parameters in Table 7.2. For the second set of controller parameters, the system without IFs is unstable and therefore, the time-domain responses with and without IFs cannot be compared).

Fig. 7.12 shows the impact of IFs on $\mu(T)$ against frequency. Fig. 7.12 shows that the IFs reduce the peak of $\mu(T)$ and result in a smaller ρ. A smaller ρ, according to (7.30), corresponds to a higher robustness level of the multi-VSC system against unstructured uncertainties. With Δ having a diagonal form (as it corresponds to a structured uncertainty), the peak of $\mu(T)$ is less than one and is larger than one without IFs. Thus, there is at least one set of structured uncertainties that destabilizes the perturbed system when IFs

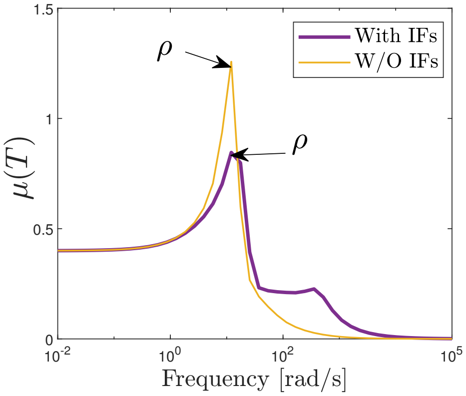

Figure 7.12: $\mu(T)$ against frequency.

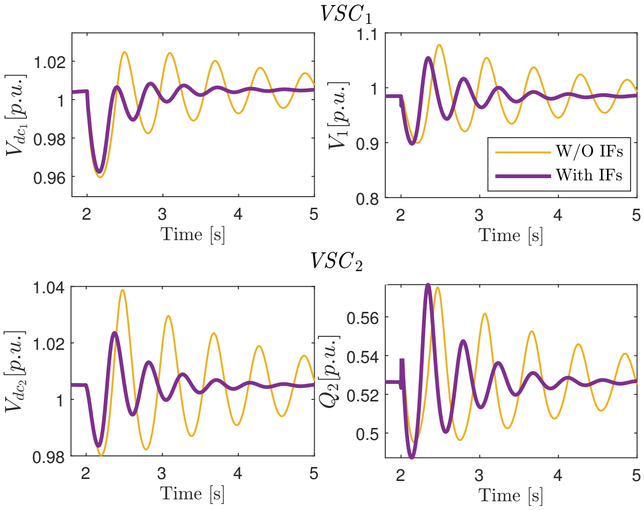

Figure 7.13: Time-domain response of the 2-VSC system to a 10% reduction in the DC voltage measurement and 2% increase in the AC voltage measurement of VSC_1.

are not employed, whereas the interconnected system in the presence of IFs maintains its stability for all sets of structured uncertainties.

To evaluate the impact of IFs on system stability in the presence of uncertainties, the DC voltage measurement of VSC_1 is decreased by 10%, and its AC voltage is increased by 2% at $t = 2s$. These two changes account for measurement errors in the converter output. Fig. 7.13 shows the system response to these changes and verifies that the oscillations in the response of the system persist without the SFs, whereas utilizing the IFs is beneficial in dampening these oscillations. This observation is in line with Fig. 7.12 and shows that the IFs enhance the robustness of the interconnected system.

7.7 Conclusion

This chapter contributed to the multi-vendor realization of multi-VSC systems by proposing interaction filters (IFs) that can reduce the negative impact of interactions on both the stability and dynamic performance of multi-VSC systems built by various manufacturers. An H_∞ minimization problem was defined to stabilize the multi-VSC system and reduce the deviation of the dynamic behavior of the multi-VSC system from the desired response of the individual converters with independently designed controllers. Two IFs were placed in the control system of each converter, one in the d-axis loop and one in the q-axis loop, to filter the measurements entering the converter controllers. These filters were obtained by solving an H_∞ minimization problem. It was also shown that the developed IFs in this chapter increase the robust stability margin of the multi-VSC system. The simulation results on the nonlinear model of a 2-VSC system verified the effectiveness of the IFs in reducing the interactions among the converters and increasing the robust stability margin of the multi-VSC system.

A potential drawback of the employment of the IFs might be the delayed response of the control system, which can be negligible if the poles of IFs are non-dominant compared to the system poles. Additionally, in the developed method, the IFs are obtained through a model-based approach, which requires sharing some level of information among the manufacturers and the grid integrator. The future work of this research will focus on the development of control methods, which would require a reduced exchange of information among different parties.

Chapter 8

AC Side External Control Loop Interactions in Parallel Converters with Grid-Forming Control Philosophy

8.1 Introduction

The alternating current (AC)-direct current (DC) power converters can be controlled using a grid-following (GFL) or a grid-forming (GFM) control philosophy. The former control scheme regulates the AC line current to replicate a current source, while the latter controls the magnitude and angle of the terminal voltage to form an ideal voltage source. Given the drawbacks of GFL converters, the inclusion of GFM converters in the AC system has been the topic of several studies recently. This chapter is divided into three parts. After the dynamic modeling of the system, in the second part, the interactions among the converters with different control philosophies (GFL or GFM) are studied. The objective is to evaluate the level of interactions and find out if a GFL converter can be replaced by a GFM converter under the same control mode. Hybrid connections of GFL and GFM converters are considered and compared against each other in terms of small-signal stability and the level of couplings. To perform the analysis, first, state-space and transfer function models of a two converter system are obtained. Eigenvalue analysis is used to evaluate stability. The impact of grid inductance and transmission line length on the stability in the presence of hybrid connections of GFL and GFM converters is also studied. Coupling among the converters is measured using the off-diagonal closed-loop transfer functions and evaluated for various combinations of control philosophies. The analysis shows that there is a strong coupling between the voltage of the GFM converter and the active power/AC voltage of the GFL converter. Thus, although having a converter in the GFM control scheme improves stability, tight control of the AC voltage is essential to not impact the performance of the adjacent converter negatively.

In the second part, the small-signal stability of multiple parallel GFM converters is analytically investigated. The stability of the system in the presence of two general types of GFM control schemes is studied. The approach is based on theoretical stability analysis rather than simulation/numerical evaluations. Using the properties of diagonally dominant matrices and matrix polynomials, it is proved that the parallel connection of GFM converters maintains small-signal stability regardless of the AC system short circuit ratio. In the last part, real-time simulation and hardware-in-the-loop (HIL) test results are presented.

8.2 Multi-VSC System Dynamics

In this section, first, the dynamic equations of a multi-VSC AC-DC power system are derived. Second, the control structures of GFM and GFL converters are explained. Then, the state-space model of the system is derived using dynamic equations, and the small-signal model is validated using the detailed model in EMT/SIMULINK. These dynamic equations along with the control system structure are used in the next sections to explain how the GFL and GFM control philosophies impact the interactions in a 2-VSC system and are also used to study the stability of parallel GFM converters.

8.2.1 System model

Fig. 8.1 shows the connection of several VSCs to a shared AC system. In the following equations, the sub-subscript i refers to the converter index, and superscript $*$ refers to the set-point, around which the equations will be linearized. Neglecting the resistive part of the AC system (R_g, R_{t_i}), the dynamic equations of parallel connection of converters shown in Fig. 8.1 are given by:

$$L_{f_i}\dot{I^d_{c_i}} = V^d_{c_i} - V^d_{t_i} - R_{f_i}I^d_{c_i} + L_{f_i}\omega_i I^q_{c_i}, \tag{8.1}$$

$$L_{f_i}\dot{I^q_{c_i}} = V^q_{c_i} - V^q_{t_i} - R_{f_i}I^q_{c_i} - L_{f_i}\omega_i I^d_{c_i}, \tag{8.2}$$

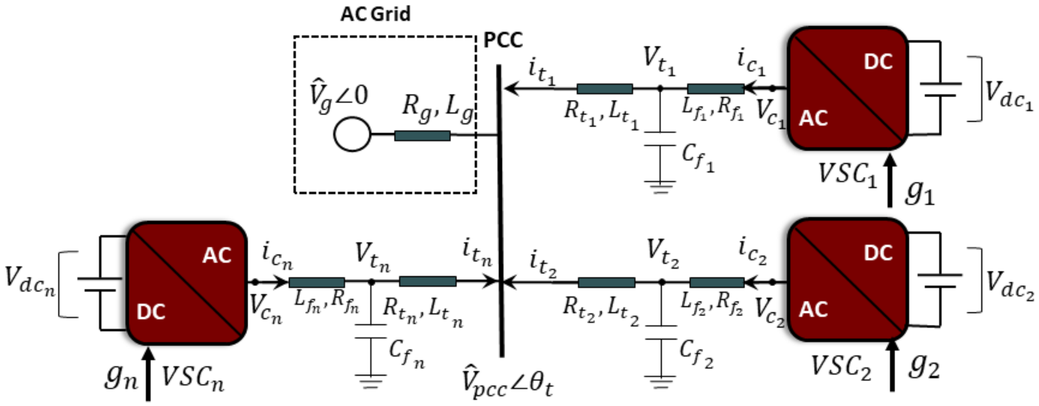

(a) multi-VSC system

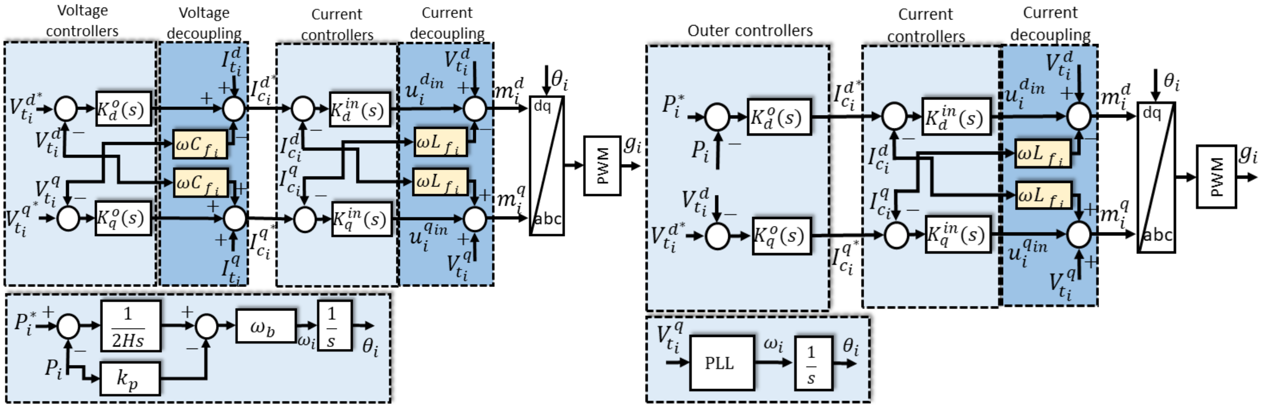

(b) GFM control scheme [62]

(c) GFL control scheme

Figure 8.1: Parallel connection of multiple VSCs and the control system of each converter.

$$C_{f_i}\dot{V}_{t_i}^d = \omega_i C_{f_i} V_{t_i}^q + I_{c_i}^d - I_{t_i}^d, \tag{8.3}$$

$$C_{f_i}\dot{V}_{t_i}^q = -\omega_i C_{f_i} V_{t_i}^d + I_{c_i}^q - I_{t_i}^q, \tag{8.4}$$

$$L_{t_i}\dot{I}_{t_i}^d = V_{t_i}^d - \frac{1}{C_v}[\frac{L_g}{L_{t_i}}V_{t_i}^d + \hat{V}_g cos\theta_i + CT_i^d] + L_{t_i}\omega_i I_{t_i}^q, \tag{8.5}$$

$$L_{t_i}\dot{I}_{t_i}^q = V_{t_i}^q - \frac{1}{C_v}[\frac{L_g}{L_{t_i}}V_{t_i}^q - \hat{V}_g sin\theta_i + CT_i^q] - L_{t_i}\omega_i I_{t_i}^d \tag{8.6}$$

where

$$C_v = 1 + L_g\sum_{i=1}^{n}\frac{1}{L_{t_i}}, \tag{8.7}$$

and

$$CT_i^d = L_g \sum_{j=1,j\neq i}^{n} \frac{1}{L_{t_j}}[V_{t_j}^d cos\theta_{ij} + V_{t_j}^q sin\theta_{ij}], \tag{8.8}$$

$$CT_i^q = L_g \sum_{j=1,j\neq i}^{n} \frac{1}{L_{t_j}}[V_{t_j}^q cos\theta_{ij} - V_{t_j}^d sin\theta_{ij}], \tag{8.9}$$

where $\theta_{ij} = \theta_i - \theta_j$, V_t^{dq} and V_c^{dq} respectively represent the direct quadrature (dq) components of voltage at the filter terminal and at the converter's terminal; I_t^{dq} and I_c^{dq} show the dq components of line current after the LC filter and at the converter-side; L_g, L_t, L_f show respectively the inductance of the AC grid, transmission line and transformer, and AC filter; and C_f is AC filter capacitance.

Equations (8.1)-(8.9) are obtained from the space-phasor representation of the AC-DC system and transforming them to the d-q reference frame. θ_i is the phase angle of the voltage at the terminal of each converter. In a GFL converter, θ_i is provided by a phase-locked loop (PLL) using the equation

$$\dot{\theta}_i = (K_{p_i}^{\text{PLL}} + \frac{K_{I_i}^{\text{PLL}}}{s})V_{t_i}^q, \tag{8.10}$$

and in a GFM converter, θ_i is provided by an active power control loop given by

$$\dot{\theta}_i = \omega_b(\frac{1}{2H_i s}(P_i^* - P_i) - K_{p_i}P_i), \tag{8.11}$$

where the active power is given by the quasi-static power transfer equation of

$$P_i = -\frac{V_{t_i}^d}{X_{t_i}C_v}[\frac{L_g}{L_{t_i}}V_{t_i}^q - \hat{V}_g sin\theta_i + CT_i^q]. \tag{8.12}$$

Therefore, the required phase angle is produced either by

$$\textbf{GFM control}\begin{cases} \dot{\theta}_i = \omega_b(\frac{1}{2H_i}x_{\theta_i} - K_{p_i}P_i), & (8.13)\\ \dot{x}_{\theta_i} = P_i^* - P_i, & (8.14)\end{cases}$$

where K_{p_i} and H_i are the proportional and integral gains of active power loop and ω_b is the base frequency, or

$$\textbf{GFL control}\begin{cases}\dot{\theta}_i = K_{p_i}^{\text{PLL}} V_{t_i}^q + K_{I_i}^{\text{PLL}} x_{\theta_i}, & (8.15)\\ \dot{x}_{\theta_i} = V_{t_i}^q, & (8.16)\end{cases}$$

where K_p^{PLL} and K_I^{PLL} are proportional and integral gains of PLL.

The time-domain representation of the active power is given by

$$P_i = I_{t_i}^d V_{t_i}^d + I_{t_i}^q V_{t_i}^q. \tag{8.17}$$

In the GFL mode, the time-domain representation of active power in (8.17) will be used to form the system matrices, and in the GFM mode, (8.12) will be utilized.

8.2.2 Control system

Fig. 8.1b shows how a converter is controlled under the GFM control philosophy [62]. The dq-components of the voltage are controlled by the outer control loops, which provide the set points for the inner current loops. The active power is controlled through controlling the phase angle in a separate control loop. This GFM scheme does not require the nominal grid frequency. Fig. 8.1c presents the GFL control philosophy. The active power and the d component of the voltage are controlled through the outer control loops, which, similar to the GFM control philosophy, provide the set points to the inner current loops. The required angle is generated by setting the q-component of the voltage to zero through the PLL.

In this study, it is assumed that both converters in Fig. 8.1 are operated under the same control mode (i.e., controlling active power and AC voltage) with exactly similar set points and the same system parameters. The only difference between the converters is the control philosophy. In the GFL control scheme, the active power is controlled by adjusting the d-axis current and through the outer control loop while in the GFM converter, the active power is controlled by controlling the voltage phase angle. In both control systems, the q-axis component of the voltage is set to zero, i.e., $V_{t_i}^{q^*} = 0$. The inner current loops have the same parameters for both GFL and GFM schemes. The parameters of the inner loop are computed using the approach proposed in [86]. the outer control loops are tuned for an appropriate transient response. The controller parameters are given in Table 8.2. Fig. 8.2 shows the black-box model of the converters focusing on the set points and the controlled outputs.

Due to the decoupling terms in the inner current loops for both GFL and GFM control schemes, (8.1)-(8.2) transform into [86]

$$L_{f_i}\dot{I_{c_i}^{dq}} = u_i^{dq_{in}} - R_{f_i}I_{c_i}^{dq}. \tag{8.18}$$

Additionally, in a GFM control scheme, due to the decoupling terms in the outer loops according to Fig. 8.1b, (8.3)-(8.4) transform into [61]

$$C_{f_i}\dot{V_{t_i}^{dq}} = I_{c_i}^{dq}. \tag{8.19}$$

(8.1)-(8.17) show that the dynamics of adjacent converters are coupled to each other through the current $I_{t_i}^{dq}$ and via the coupling terms CT_i^{dq}. In a GFL VSC, $I_{t_i}^{dq}$ impacts the voltage and the active power directly according to (8.3) and (8.17). Therefore, both the active power and the AC voltage of a GFL converter are impacted by the dynamics of the adjacent converter. On the other hand, in a GFM converter, the AC voltage is decoupled from the dynamics of the adjacent converter according to (8.18) and (8.19), and only the active power control loop interacts with the adjacent converter. Therefore, it seems that by employing a GFM converter, a smaller part of the system is impacted by the interactions.

According to (8.5)-(8.9), two important parameters may affect the interactions: the grid inductance (L_g) and the distance of the converters from the PCC (L_{t_i}). According to (5)-(9), the larger the grid inductance is, the larger $\frac{CT^{dq}}{C_v}$ becomes. In the extreme cases

$$if L_g \rightarrow 0, \frac{CT^{dq}}{C_v} = 0,$$

$$if L_g \rightarrow \infty, \frac{CT^d}{C_v} = \frac{\sum_{j=1, j\neq i}^{n} \frac{1}{L_{t_j}}[V_{t_j}^d cos\theta_{ij} + V_{t_j}^q sin\theta_{ij}]}{\sum_{i=1}^{n} \frac{1}{L_{t_i}}},$$

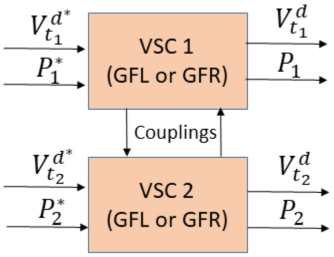

Figure 8.2: Black-box model of the two-converter system.

$$if L_g \to \infty, \frac{CT^q}{C_v} = \frac{\sum_{j=1,j\neq i}^{n} \frac{1}{L_{t_j}}[V_{t_j}^q cos\theta_{ij} - V_{t_j}^d sin\theta_{ij}]}{\sum_{i=1}^{n} \frac{1}{L_{t_i}}}.$$

Therefore, the impact of coupling terms on the dynamics of the converters becomes larger as the grid inductance increases.

Regarding the impact of the distance of the converters from PCC, if the GFL converter is located far from the AC grid, the GFL converter may be unable to follow the grid specifications, and consequently causes instability. On the other hand, in a GFM converter, the voltage is stiffly controlled irrespective of the grid inductance. Therefore, the GFM converter will still be stable when located in a farther location from the AC grid. Additionally, in extreme cases when $L_{t_2} \to \infty$, $\frac{CT^{dq}}{C_v} \to 0$, which means that the impact of the dynamic interactions on the GFL converter becomes smaller. In summary, it seems that locating the GFM converter farther from the AC grid is not detrimental to system stability, while locating the GFL converter in farther locations from PCC may cause instability.

8.2.3 State-space representation of 2-VSC system

Linearizing the system equations (8.1)-(8.17), and considering either (8.18) or (8.19), or both depending on the control philosophy, the linear state-space representation of the open-loop system becomes

$$\dot{X} = AX + BU + \bar{B}\tilde{P}^*, \tag{8.20}$$

$$Y = CX + DU, \tag{8.21}$$

where $X = [X_1; X_2]$, $X_i = [\tilde{I}_{c_i}^d, \tilde{I}_{c_i}^q, \tilde{V}_{t_i}^d, \tilde{V}_{t_i}^q, \tilde{I}_{t_i}^d, \tilde{I}_{t_i}^q, \tilde{\theta}_i, \tilde{x}_{\theta_{pi}}]^T$, $\tilde{}$ shows a small perturbation around the operating point, $\tilde{x}_{\theta_{pi}}$ is the internal state variable of the phase angle generation loop given by (14) or (16), $U = [U_1; U_2]$, $U_i = [\tilde{u}_i^{din}, \tilde{u}_i^{qin}]^T$, and $\tilde{P}^* = [\tilde{P}_i^*]$ (for VSC$_i$ under GFM control scheme). The outputs controlled by the outer loops are $Y_i = [\tilde{V}_{t_i}^d, \tilde{V}_{t_i}^q]$ for a GFM converter and $Y_i = [\tilde{P}_i, \tilde{V}_{t_i}^d]$ for a GFL converter.

The closed-loop state-space model then will be obtained by considering the inner-outer control structure in Figs. 8.1b-c as shown in Fig. 8.3.

8.2.4 Model validation

To verify that the small-signal model is precise and compatible with the EMT and nonlinear models, model validation has been performed prior to using the small-signal model. Model validation has only been presented for one scenario, where converter 1 is in the GFL

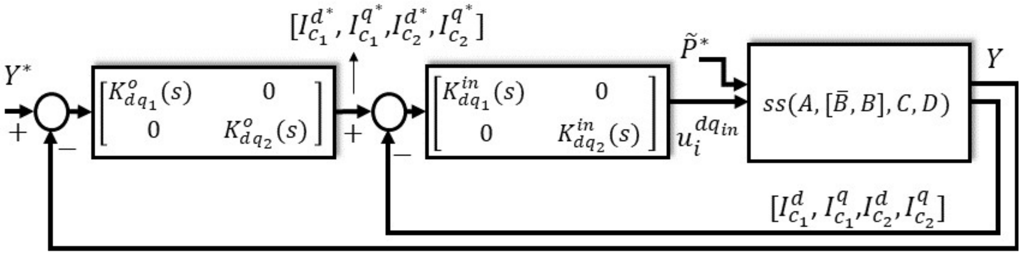

Figure 8.3: Closed-loop system of the 2-VSC system with state-space model given in (8.20)-(8.21).

control mode and converter 2 is in the GFM control mode, and it verifies the validity of the converter models in both the GFL and GFM control schemes. The test system and control parameters are respectively given in Table 8.1 and Table 8.2. Fig. 8.4 shows the response of the converters to 10% increase in the set point of the active power and 10% decrease in the set point of the AC voltage.

Table 8.1: Parameters of the test system [5]

Quantity	Value	Description
P	200 MW	Active power
V_{dc}	400 KV	DC voltage
V_s	230 KV	AC grid RMS voltage
C_f	10uF	AC side filter
f	60	Frequency
L_f	0.0724 H	Filter inductance
L_t	0.0291 H	Transmission line inductance
L_g	0.0391 H	AC grid inductance
R	0.005 Ω	Filter and switches on-state resistance
C_{dc}	300 μ F	DC side capacitance

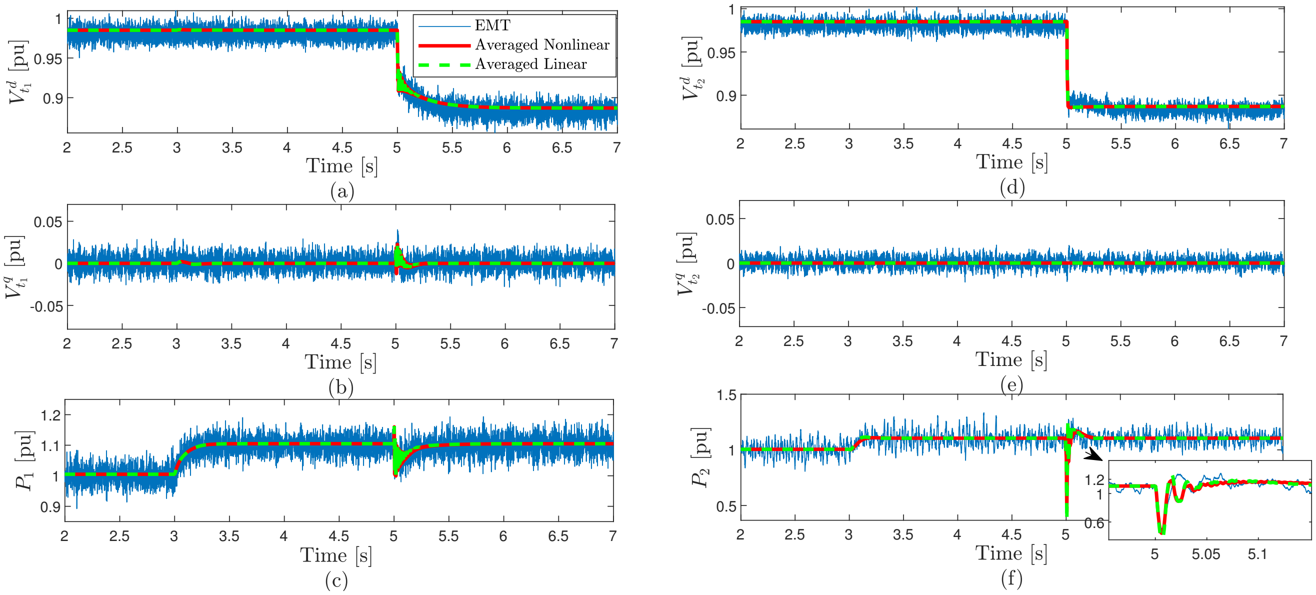

(a) VSC_1 (b) VSC_2

Figure 8.4: Model validation of parallel connection of a GFL and a GFM converter: system response to 10% increase in active powers and 10% decrease in AC voltages.

Table 8.2: Control parameters

GFL Control Scheme	
PLL	$K_p = 50$ and $K_I = 716$
Active power loop	$K_p = 0$ and $K_I = 11.64$
AC voltage loop	$K_p = 0$ and $K_I = -64$
Inner current loop	$K_p = 1.36$ and $K_I = 0.0945$
GFM Control Scheme	
Active power loop	$K_p = 0.01$ and $H = 2.37$
Outer voltage loops	$K_p = 1$ and $K_I = 5$
Inner current loop	$K_p = 1.36$ and $K_I = 0.0945$

8.3 Analysis of Control Loop Interactions in Parallel Grid-Forming and Grid-Following Converters

8.3.1 Interaction analysis

In this section, interaction analysis has been performed on the 2-VSC system. First, the small-signal stability of the system is analyzed under three different scenarios: parallel connections of two GFL converters (denoted as 2GFL), parallel connections of GFL and GFM converters (denoted as GFL, GFM), and parallel connections of two GFM converters (denoted as 2GFM). Next, a coupling analysis is performed to identify which control philosophy causes lower interaction levels. The impact of grid inductance and the distance of the converters from PCC on the interactions are also investigated.

Small-signal stability

Considering the closed-loop system in Fig. 8.3, Fig. 8.5 shows the eigenvalue locus of the 2-VSC system with various control philosophies and variations in the grid inductance. Fig. 8.5a shows the eigenvalues for parallel connections of two GFL converters, in Fig. 8.5b one of the GFL converters is replaced by a GFM converter, and in Fig. 8.5c, both converters are in the GFM mode.

The eigenvalue locus in Fig. 8.5a indicates that the parallel connection of two GFL converters loses stability with increasing the grid inductance while replacing one of the GFL converters or both of them with a GFM converter stabilizes the system (Figs. 8.5b-c). The reason is that in a GFM converter scheme, the voltage is tightly controlled and is not impacted by the adjacent converter dynamics or the characteristics of the AC grid according to (8.18)-(8.19). On the other hand, the AC voltage and the active power of the GFL converter are impacted by the changes in the grid inductance, and as a result by the adjacent converter.

Fig. 8.6 shows the eigenvalue locus of the 2-VSC system with changes in the inductance L_{t_1} and L_{t_2}, representing the impact of distance of the converters from PCC on the interactions. A larger value of the inductance resembles a longer transmission line connecting the converters to the PCC. Based on Figs. 8.6a-b, placing the GFL converter to a farther location from the main grid causes instability; while placing the GFM converter to farther locations from the PCC does not cause instability.

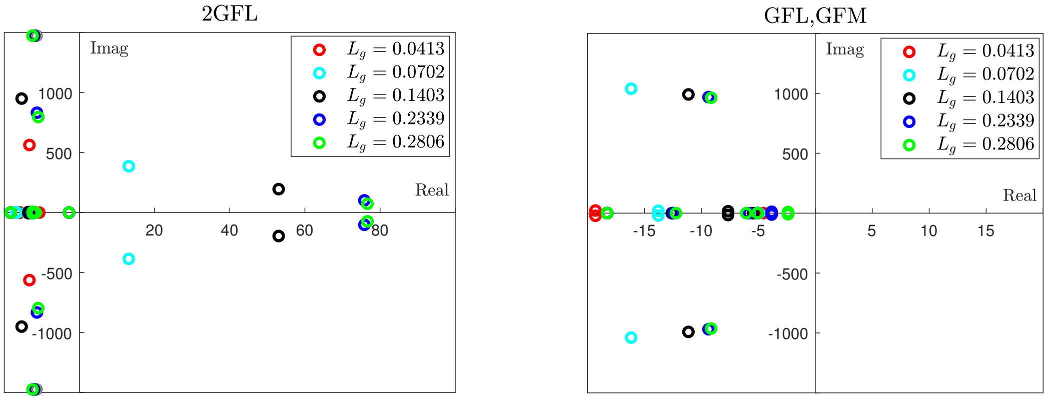

(a) Parallel connection of two GFL converters.

(b) Parallel connection of a GFL and a GFM converter.

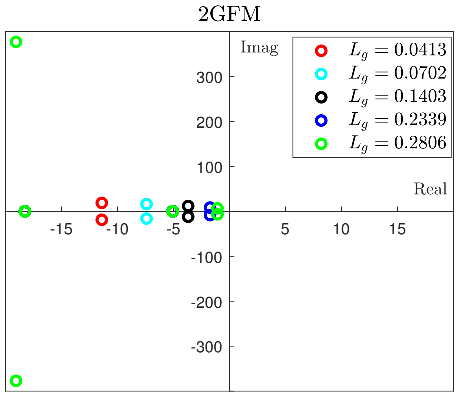

(c) Parallel connection of two GFM converters.

Figure 8.5: Eigenvalue locus for variations in the grid inductance (L_g) .

Comparison of GFL and GFM control philosophies in terms of the level of interactions

The closed-loop transfer function of the 2-VSC system using Fig. 8.3 is given by

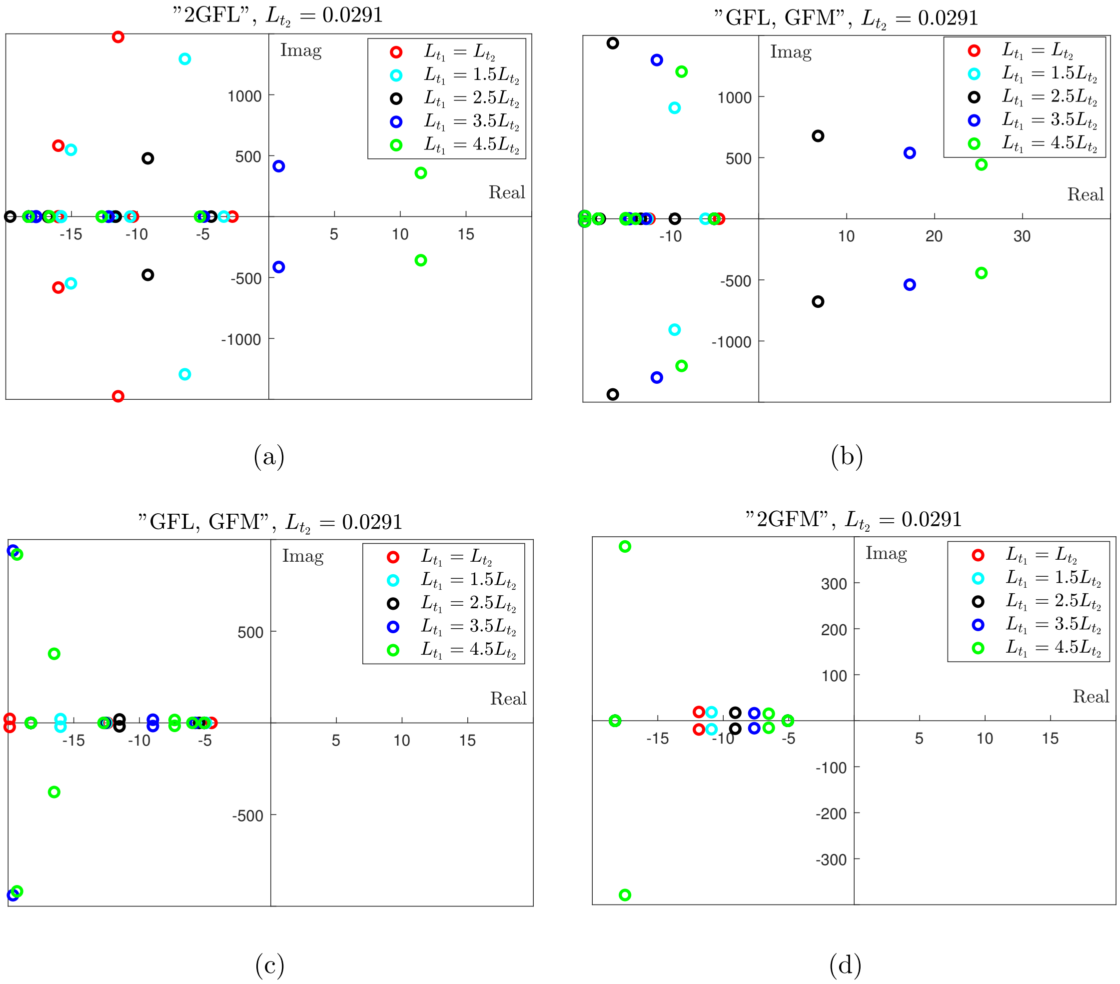

(a) (b) (c) (d)

Figure 8.6: Eigenvalue locus with changes in the transmission line inductance. Increasing the distance of a) the GFL VSC, b) the GFL VSC, c) the GFM VSC, and d) the GFM VSC from the PCC.

$$\begin{bmatrix} P_1 \\ V_{t_{d_1}} \\ P_2 \\ V_{t_{d_2}} \end{bmatrix} = \begin{bmatrix} G^{\mathrm{CP}}_{P_1,P_1^*} & G^{\mathrm{CP}}_{P_1,V^*_{t_{d_1}}} & G^{\mathrm{CP}}_{P_1,P_2^*} & G^{\mathrm{CP}}_{P_1,V^*_{t_{d_2}}} \\ G^{\mathrm{CP}}_{V_{t_{d_1}},P_1^*} & G^{\mathrm{CP}}_{V_{t_{d_1}},V^*_{t_{d_1}}} & G^{\mathrm{CP}}_{V_{t_{d_1}},P_2^*} & G^{\mathrm{CP}}_{V_{t_{d_1}},V^*_{t_{d_2}}} \\ G^{\mathrm{CP}}_{P_2,P_1^*} & G^{\mathrm{CP}}_{P_2,V^*_{t_{d_1}}} & G^{\mathrm{CP}}_{P_2,P_2^*} & G^{\mathrm{CP}}_{P_2,V^*_{t_{d_2}}} \\ G^{\mathrm{CP}}_{V_{t_{d_2}},P_1^*} & G^{\mathrm{CP}}_{V_{t_{d_2}},V^*_{t_{d_1}}} & G^{\mathrm{CP}}_{V_{t_{d_2}},P_2^*} & G^{\mathrm{CP}}_{V_{t_{d_2}},V^*_{t_{d_2}}} \end{bmatrix} \times \begin{bmatrix} P_1^* \\ V^*_{t_{d_1}} \\ P_2^* \\ V^*_{t_{d_2}} \end{bmatrix}, \tag{8.22}$$

where the superscript "CP" stands for the control philosophy. For two GFM converters in parallel, "CP" is 2GFM, for two parallel GFL converters, "CP" is 2GFL, and for a parallel connection of GFL and GFM converter, "CP" will be GFL, GFM. Because the two converters have exactly similar parameters and control modes, three sets of transfer function matrices will be obtained in total.

The off-diagonal transfer functions in (8.22) represent the impact of changes in the voltage/active power set-point of one converter on the voltage/active power of the adjacent converter and thus show the couplings. It is worth mentioning that, according to the control system in Fig. 8.1b and (18)-(19), the voltage of the GFM converter is not impacted by the power or voltage of adjacent converters. Therefore, for VSC$_i$ in GFM mode, $G^{\mathrm{CP}}_{V_{t_{d_i}},V^*_{t_{d_j}}} = 0$, $G^{\mathrm{CP}}_{V_{t_{d_i}},P^*_j} = 0$.

The Bode magnitude diagrams of the off-diagonal transfer functions in (8.22) are plotted in Fig. 8.7. Because the intensity of interactions is of interest, the bode magnitude diagrams are only employed and the phase diagrams are neglected. In the Bode magnitude diagrams, a magnitude less than zero shows a small amplitude, and thus the external interactions are insignificant. As a result, based on Fig. 8.7:

1. The impact of a set-point change in the active power of one converter on the active power of an adjacent converter is insignificant and is valid for various combinations of GFL and GFM control scheme, Fig. 8.7a.
2. The active power of the adjacent converter is significantly impacted due to a set-point change in the voltage of the GFM converter, Fig. 8.7b.
3. The impact of a set-point change in the active power of the GFL or GFM converter on the voltage of the adjacent converter is insignificant, Fig. 8.7c.
4. The AC voltage of the adjacent GFL converter is significantly impacted by a set-point change in the voltage of the GFM converter, Fig. 8.7d.

In summary, the adjacent converter is significantly impacted by the AC voltage changes in a GFM converter; as a result, the AC voltage is a critical variable in a GFM converter scheme which has to be tightly controlled and monitored.

8.3.2 Offline time-domain simulations

A 2-VSC system is simulated in EMT/SIMULINK with the parameters given in Table 8.1.

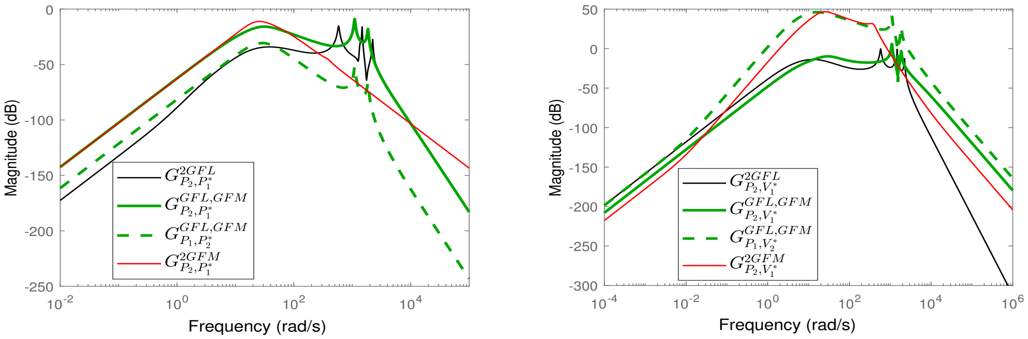

(a) Interaction of active power loops

(b) Interaction of voltage and active power loops

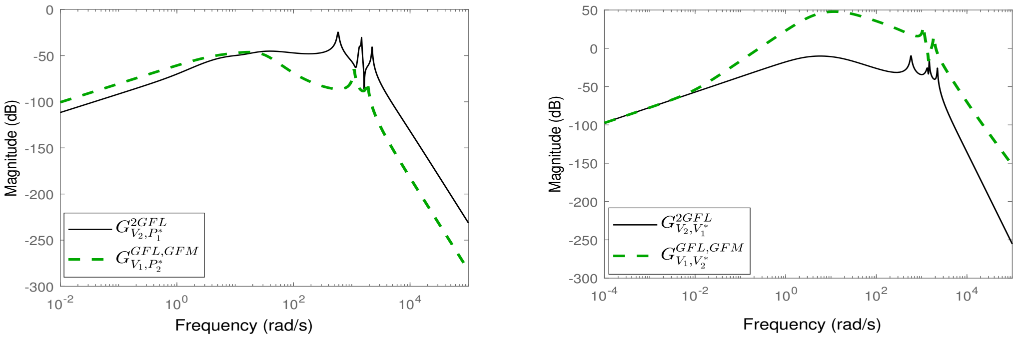

(c) Interaction of voltage and active power loops

(d) Interaction of voltage loops

Figure 8.7: Comparison of "2GFL", "GFL, GFM", and "2GFM" parallel converters in terms of interaction level

Comparison of stability of a 2-VSC system under 2GFL; GFL, GFM; and 2GFM control philosophies

To verify the results of the eigenvalue analysis, the time-domain response of the 2-VSC system under "GFL, GFM" and 2GFM control philosophies is plotted in Figs. 8.8-8.9 with $L_g = 0.1$. The 2-VSC system under 2GFL control scheme is not stable and thus the response of the system is not shown. According to Figs. 8.8-8.9, the 2-VSC system is stable in the case of 2GFM and GFL, GFM control schemes.

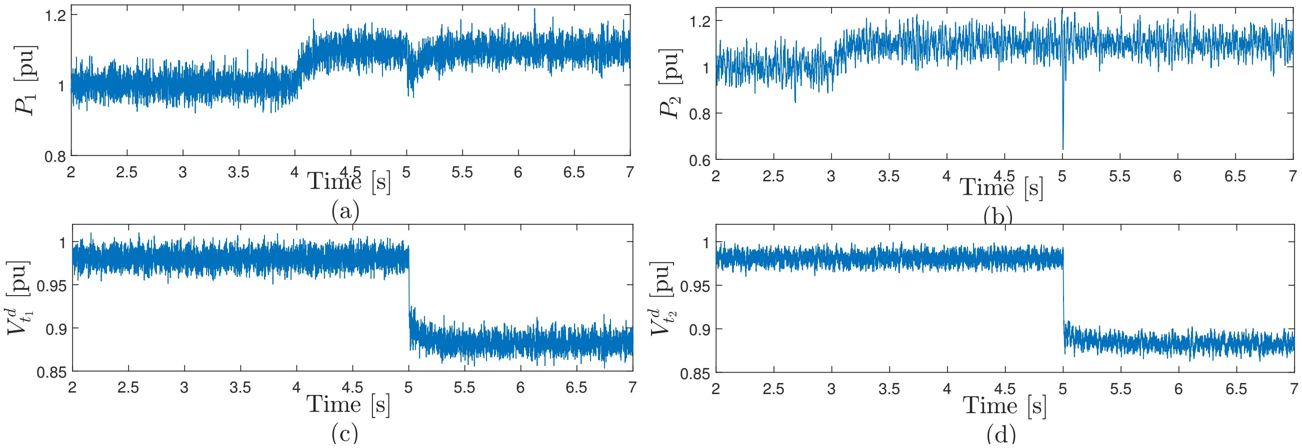

(a) (b) (c) (d)

Figure 8.8: Time-domain response of the 2-VSC under GFL, GFM control scheme (VSC$_1$ and VSC$_2$ have GFL and GFM control schemes) for $L_g = 0.1$.

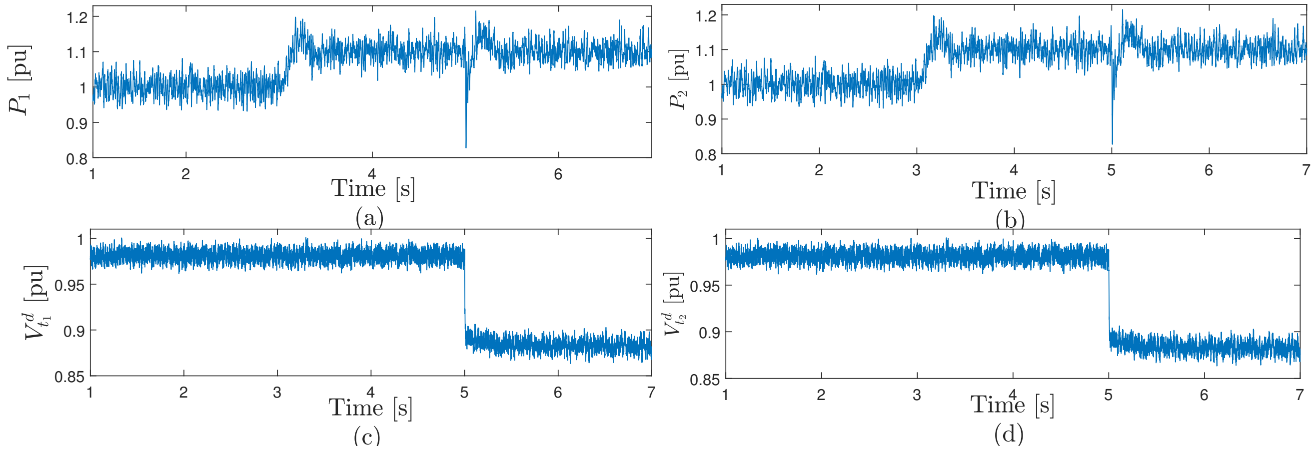

(a) (b) (c) (d)

Figure 8.9: Time-domain response of the 2-VSC under 2GFM control scheme for $L_g = 0.1$.

Impact of the distance of converters from PCC on stability

Figs. 8.10-8.11 shows the time-domain response of the 2-VSC system under the GFL, GFM control scheme. In Fig. 8.10, VSC$_1$ under the GFL control scheme is placed at a farther location from PCC, which indicates instability. In Fig. 8.11, VSC$_2$ under the GFM control scheme is placed at a farther location from PCC, which indicates a stable operation of the 2-VSC system. Time-domain responses in Figs. 8.10-8.11 verify the eigenvalue locus in

Fig. 8.6.

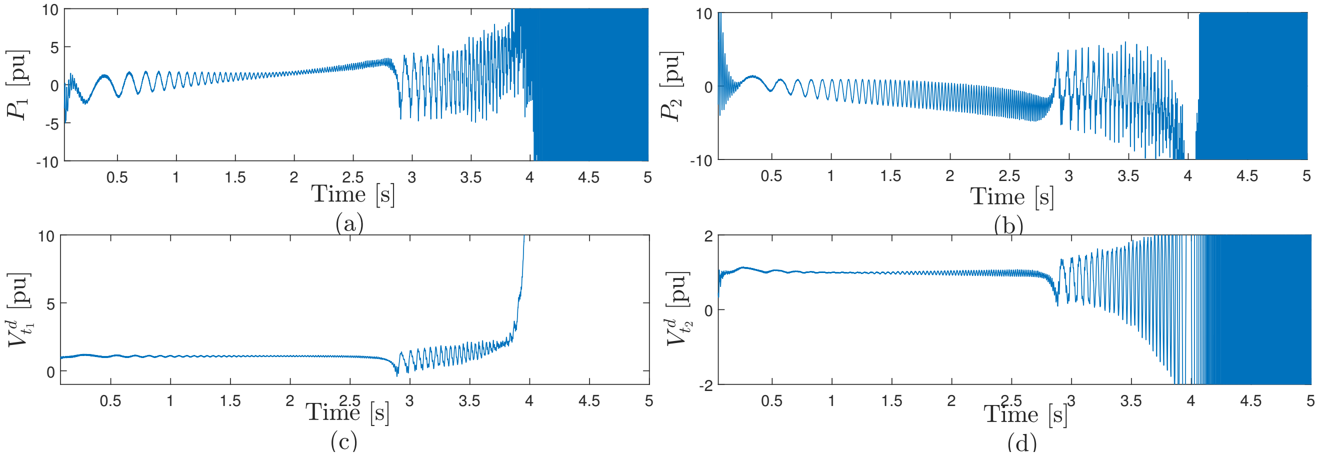

Figure 8.10: Time-domain response of the 2-VSC under GFL, GFM control scheme for $L_{t_1} = 0.331$ and $L_{t_2} = 0.0291$.

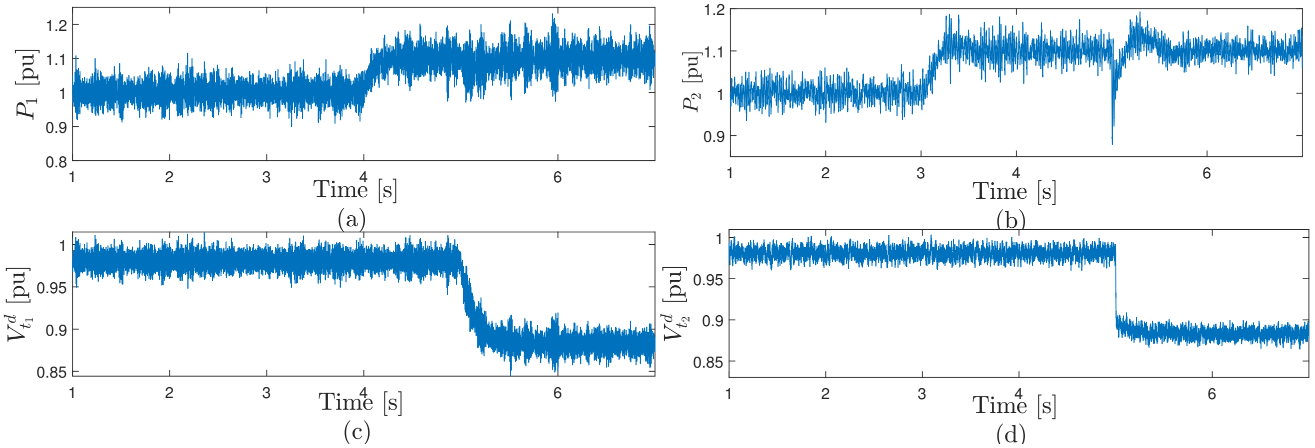

Figure 8.11: Time-domain response of the 2-VSC under GFL, GFM control scheme for $L_{t_1} = 0.0291$ and $L_{t_2} = 0.331$.

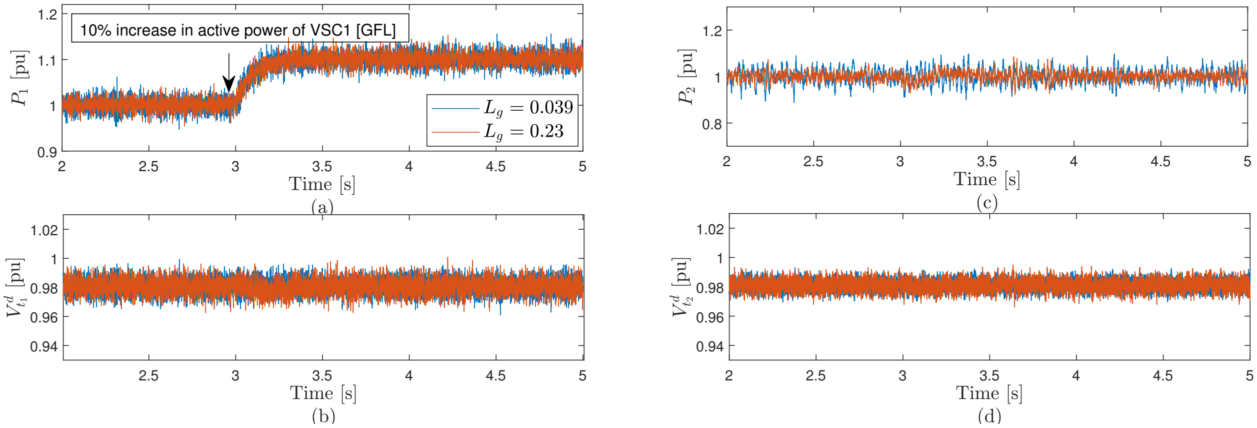

Figure 8.12: Time-domain response of GFL, GFM 2-VSC system to a 10% increase in the active power of GFL converter.

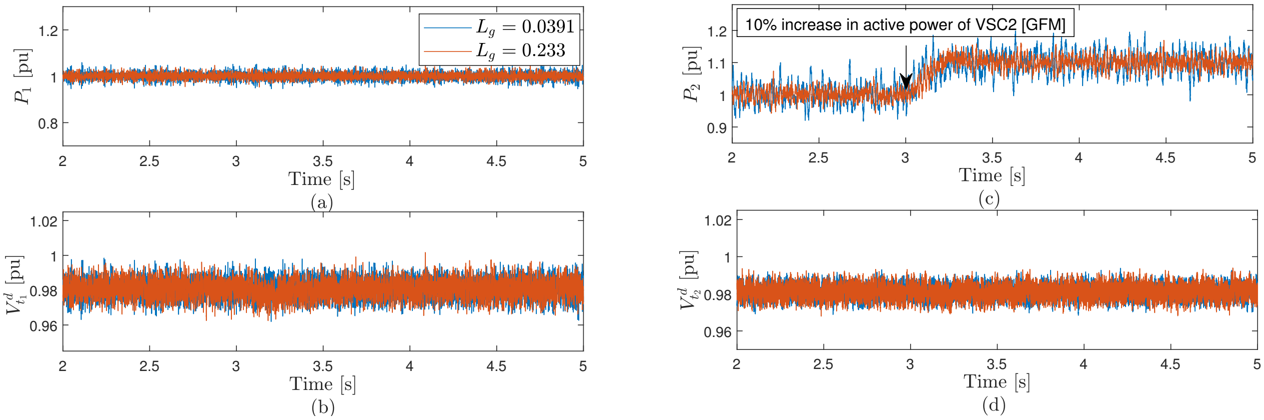

Figure 8.13: Time-domain response of GFL, GFM 2-VSC system to a 10% increase in the active power of GFM converter.

Coupling analysis

Figs. 8.12-8.15 show the time-domain response of a 2-VSC system under GFL, GFM control scheme for two values of grid inductance: $L_g = 0.0391$ (high SCR) and $L_g = 0.233$ (low SCR). A 10% increase is applied to the active power of GFL and GFM converters respectively in Fig. 8.12 and Fig. 8.13 and the response of the other converter is observed.

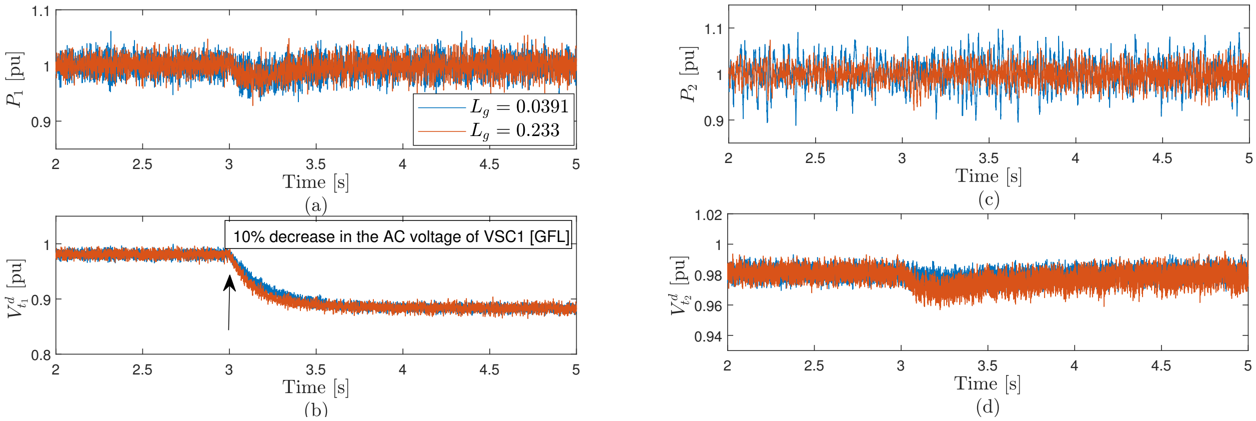

Figure 8.14: Time-domain response of GFL, GFM 2-VSC system to a 10% decrease in the AC voltage of GFL converter.

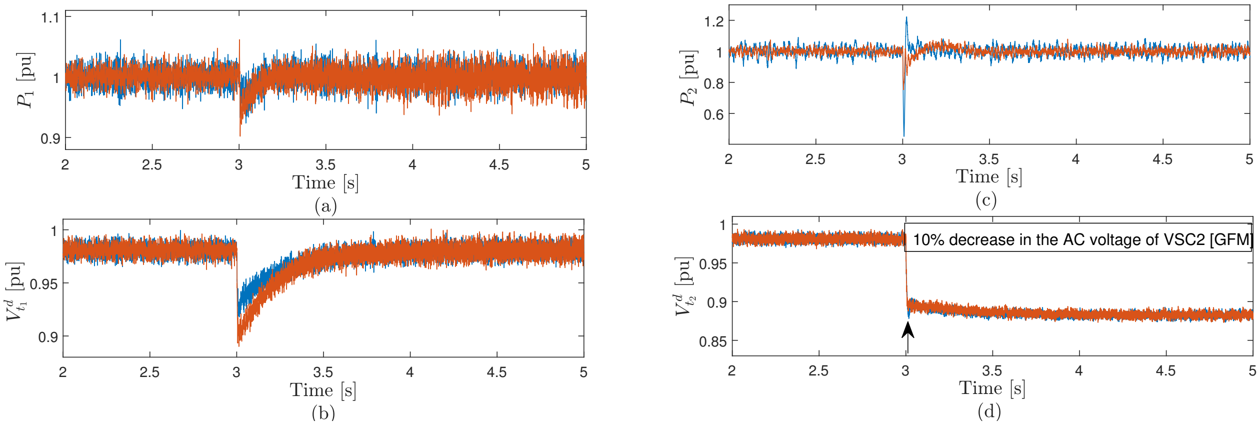

Figure 8.15: Time-domain response of GFL, GFM 2-VSC system to a 10% decrease in the AC voltage of GFM converter.

According to Figs. 8.12-8.13, the impact of a change in the active power of one converter on the response of adjacent converter is insignificant even with a high inductance of the AC grid. This observation is compatible with the Bode diagrams in Figs. 8.7c and 8.7a.

A 10% decrease is applied to the AC voltage of GFL and GFM converters respectively in Fig. 8.14 and Fig. 8.15 and the response of the other converter is observed. According to Fig. 8.14, a change in the AC voltage of the GFL converter does not impact the active power and AC voltage of the GFM converter significantly. However, based on Fig. 8.15, a change in the AC voltage of the GFM converter causes a significant change in the active power and AC voltage of the GFL converter. This observation is compatible with the Bode diagrams in Figs. 8.7b and 8.7d.

8.4 Stability of Parallel Grid-Forming Converters

The GFM control techniques can be classified into two main types based on their synchronization method, namely PLL-based and non-PLL-based methods [62, 63]. In the PLL-based GFM control, the nominal grid frequency is provided to the controller either directly or via a PLL, whereas the non-PLL-based GFM control does not require the nominal grid frequency and does not suffer from the stability issues caused by a PLL. Figs. 8.1c-d shows these two main categories.

Referring to Fig. 8.16, the active power is regulated by controlling the angle either through a non-PLL or a PLL-based scheme [62, 65, 66]:

$$\textbf{Non-PLL-based GFR:}\begin{cases}\dot{\theta}_i = \omega_b(\frac{1}{2H_i}x_{\theta_i} - K_{p_i}P_i) & (8.23)\\ \dot{x}_{\theta_i} = P_i^* - P_i & (8.24)\end{cases}$$

$$\textbf{PLL-based GFR: } \dot{\theta}_i = \omega_b(K_{p_i}(P_i^* - P_i) + \omega_0). \qquad (8.25)$$

Considering (8.1)-(8.12), (8.18)-(8.19), and (8.23)-(8.25) for n-parallel GFM converters, let's define $x_i = [x_i^{[1]}, x_i^{[2]}]^T$, where $x_i^{[1]} = [\Delta I_{c_i}^d, \Delta I_{c_i}^q, \Delta V_{t_i}^d, \Delta V_{t_i}^q]^T$, $x_i^{[2]} = [\Delta\theta_i, \Delta x_{\theta_i}]^T$ (for a non-PLL-based GFM VSC), $x_i^{[2]} = [\Delta\theta_i]$ (for a PLL-based GFM VSC), where Δ

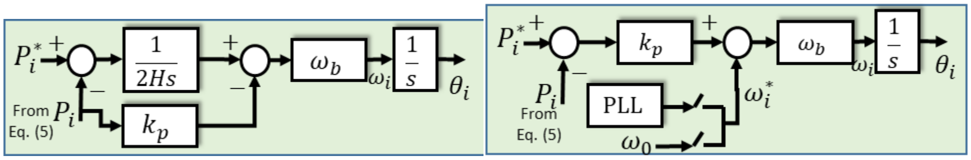

(a) (b)

Figure 8.16: a) Non-PLL-based active power loop, and b) PLL-based active power loop in a GFM control.

corresponds to the small-signal representation. In this definition, the state variables of each VSC are split into two groups: the state variables associated with the inner-outer cascaded voltage and current loops ($x_i^{[1]}$) and the state variables associated with the active power control loop (APCL) ($x_i^{[2]}$). Considering this definition and according to Fig. 8.17, the dynamics of $x_i^{[1]}$ are decoupled from $x_i^{[2]}$ and x_j. The APCL, on the other hand, is impacted by the voltage control loop and the state variables of adjacent VSCs through CT_i^q in (8.12). converter interactions.

Fig. 8.18 shows the coupling among converters for a 2-VSC system. Because the cascaded control loops are stable, the state variables $x_k^{[1]}$ impact the evolution of $x_i^{[2]}$ as exogenous bounded inputs, but $x_k^{[2]}$ does not impact $x_i^{[1]}$. Therefore, the mutual interactions among VSCs via the state variables $x_i^{[2]}$ are the decisive interactions impacting the system's stability.

To obtain the system's state matrix for stability analysis, (8.13)-(8.15) need to be linearized, for which the linearized equation of active power (8.12) with respect to $[x_1^{[2]}, x_2^{[2]}, ..., x_n^{[2]}]^T$ is required:

$$\Delta P_i = \frac{\hat{V}_g V_{t_{i0}}^d cos\theta_{i0}}{X_{t_i} C_v} \Delta\theta_i - \frac{V_{t_{i0}}^d}{X_{t_i} C_v} \Delta CT_i^q, \tag{8.26}$$

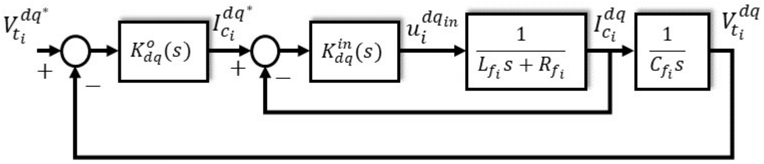

Figure 8.17: Cascaded inner-outer control loops for a GFM converter.

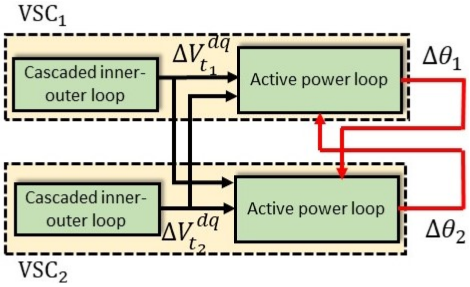

Figure 8.18: Interaction mechanism of a 2-VSC system with GFM control.

$$\Delta CT_i^q = -L_g \sum_{j=1, j\neq i}^{n} L_{t_j}^{-1} V_{t_{j_0}}^d cos\theta_{ij_0}(\Delta\theta_i - \Delta\theta_j), \tag{8.27}$$

assuming that $V_{t_{i_0}}^q = 0$. The subscript 0 represents an operating point. Replacing (8.27) in (8.26) results in

$$\Delta P_i = a_{ii}\Delta\theta_i + \sum_{j=1, j\neq i}^{n} a_{ij}\Delta\theta_j, \tag{8.28}$$

where

$$a_{ii} = \frac{\hat{V}_g V_{t_{i_0}}^d cos\theta_{i_0}}{X_{t_i} C_v} - \sum_{j=1, j\neq i}^{n} a_{ij}, \tag{8.29}$$

$$a_{ij} = -\frac{L_g}{L_{t_j}} \frac{V_{t_{i_0}}^d V_{t_{j_0}}^d}{X_{t_i} C_v} cos\theta_{ij_0}. \tag{8.30}$$

State matrix for PLL-based APCL

Considering (8.28) and (8.15), the system state-space model associated with $x_i^{[2]} = \Delta\theta_i$ becomes

$$[\dot{\Delta\theta_i}] = \left[-K_{p_i}\omega_b a_{ij}\right]_{n\times n}[\Delta\theta_j]; i, j \in \{1, , ..n\}. \tag{8.31}$$

State matrix for non-PLL-based APCL

For the sake of clarity, for this scenario, the state matrix A is only given for $n = 2$. However, all the analyses and conclusions are extendable to the case $n > 2$. Considering (8.28) and (8.13), the system state-space model becomes

$$\begin{bmatrix} \dot{\Delta\theta_1} & \dot{\Delta x_{\theta_1}} & \dot{\Delta\theta_2} & \dot{\Delta x_{\theta_2}} \end{bmatrix}^T = \begin{bmatrix} -K_{p_1}\omega_b a_{11} & \frac{\omega_b}{2H_1} & -K_{p_1}\omega_b a_{12} & 0 \\ -a_{11} & 0 & -a_{12} & 0 \\ -K_{p_2}\omega_b a_{21} & 0 & -K_{p_2}\omega_b a_{22} & \frac{\omega_b}{2H_2} \\ -a_{21} & 0 & -a_{22} & 0 \end{bmatrix} \begin{bmatrix} \Delta\theta_1 \\ \Delta x_{\theta_1} \\ \Delta\theta_2 \\ \Delta x_{\theta_2} \end{bmatrix}. \tag{8.32}$$

8.4.1 Stability analysis

To determine the conditions under which the system maintains stability, in spite of interactions among the converters, the system's characteristic polynomial needs to be evaluated. Before computing the characteristic polynomial, the following theorems and definitions are presented. The reader is referred to the provided references for proofs.

Definition I [38]: Matrix $A = [a_{ij}]_{n \times n}$ is called strictly diagonally dominant if

$$|a_{ii}| > \sum_{j \neq i} |a_{ij}| \quad \text{for all i.} \tag{8.33}$$

Theorem I [38]: If a matrix is strictly diagonally dominant and all its diagonal elements are positive (negative), the real part of its eigenvalues are positive (negative).

Theorem II

$$det(\begin{bmatrix} A_{11} & A_{12} \\ A_{21} & A_{22} \end{bmatrix}) = det(A_{22}) det(A_{11} - A_{12} A_{22}^{-1} A_{21}). \tag{8.34}$$

Theorem III [74] The second order matrix polynomial $M_1 s^2 + M_2 s + M_3 = 0$ is stable if

$$M_1 > 0, M_2 > 0, M_3 > 0. \tag{8.35}$$

Stability of parallel GFM VSCs with a PLL-based APCL

Since, based on (8.29) and (8.30), $a_{ij} < 0$ and $a_{ii} > 0$, the state matrix A given in (8.31) is strictly diagonally dominant and has negative diagonal elements. Therefore, all the eigenvalues of A have negative real parts. As a result, the connection of several PLL-based GFM VSCs maintains stability if $K_{p_i} > 0$ (i.e., positive proportional gain for the APCL).

Stability of parallel GFM VSCs with a non-PLL-based APCL

Rearranging the matrices in (8.32) results in

$$\begin{bmatrix} \dot{\Delta\theta_1} \\ \dot{\Delta\theta_2} \\ \dot{\Delta x_{\theta_1}} \\ \dot{\Delta x_{\theta_2}} \end{bmatrix} = \begin{bmatrix} \omega_b \begin{bmatrix} K_{p_1} & 0 \\ 0 & K_{p_2} \end{bmatrix} \begin{bmatrix} -a_{11} & -a_{12} \\ -a_{21} & -a_{22} \end{bmatrix} & \omega_b \begin{bmatrix} \frac{1}{2H_1} & 0 \\ 0 & \frac{1}{2H_2} \end{bmatrix} \\ \begin{bmatrix} -a_{11} & -a_{12} \\ -a_{21} & -a_{22} \end{bmatrix} & \begin{bmatrix} 0 & 0 \\ 0 & 0 \end{bmatrix} \end{bmatrix} \begin{bmatrix} \Delta\theta_1 \\ \Delta\theta_2 \\ \Delta x_{\theta_1} \\ \Delta x_{\theta_2} \end{bmatrix} \tag{8.36}$$

, where the state matrix is

$$A = \begin{bmatrix} \omega_b \bar{K}_p \bar{A} & \omega_b \bar{H} \\ \bar{A} & 0 \end{bmatrix}.$$

Using $det(sI - A)$ to determine the system's characteristic polynomial and applying theorem II result in

$$\begin{aligned} \Delta(s) = det(sI - A) = det(&\begin{bmatrix} sI - \omega_b \bar{K}_p \bar{A} & -\omega_b \bar{H} \\ -\bar{A} & sI \end{bmatrix}) \\ = det(sI)det(&(sI - \omega_b \bar{K}_p \bar{A}) - \omega_b \bar{H} s^{-1} \bar{A}) \\ =det(&s^2 I + \omega_b \bar{K}_p(-\bar{A})s + \omega_b \bar{H}(-\bar{A})) \\ =det(&\bar{A})det(s^2 \underbrace{(-\bar{A})^{-1}}_{M_1} + \underbrace{\omega_b \bar{K}_p}_{M_2} s + \underbrace{\omega_b \bar{H}}_{M_3}). \end{aligned} \tag{8.37}$$

The characteristic polynomial in (8.37) is a second-order matrix polynomial. According to theorem III, since matrix $\bar{A}$ is strictly diagonally dominant with negative diagonal entries, $\bar{A}$ is stable. Since $\bar{A}$ is symmetric and also stable, it is negative definite. Therefore, $-\bar{A}^{-1}$ is positive definite. If $K_{p_i} > 0$ and $H_i > 0$, the conditions in (8.35) are satisfied, i.e., $M_1 > 0$, $M_2 > 0$, $M_3 > 0$. Thus, the system is small-signal stable irrespective of the grid inductance. Fig. 8.5c shows the eigenvalue locus of a 2-VSC system for various values of AC grid inductance, confirming the small-signal stability of the system.

8.5 Results of Real-Time Simulation and HIL Tests

8.5.1 Experimental setup

The experimental setup is shown in Fig. 8.19 for simulating a 2-VSC system. Two real-time simulators were available, one OPAL-RT (OP5700), and one dSPACE (MicroLab Box). Each simulator is connected to one host PC, shown in Fig. 8.19. Both simulators are SIMULINK-based, and the required software for each one of them is installed on its host PC. The IO ports on the OPAL-RT side are DB37, while the analog signals on the dSPACE side are BNC type. The wiring between the simulators is done using BNC lead connectors and BNC cables due to the unavailability of custom-made cables.

Initially, the idea was to use OPAL-RT for simulating the AC system and the converters, and use the dSPACE for implementing the converters' controllers. For doing so, nine signals per converter needed to be sent from OPAL-RT (physical system) to the dSPACE (controller). These signals include: 1) 3-phase voltages at the filter terminal, 2) 3-phase currents at the converter side, and 3) 3-phase currents after the filter. These signals totally add up to 18 analog signals for a 2-VSC system. However, the number of analog cards in the available OPAL-RT simulator was 16, and it was impossible to transfer 18 signals to the dSPACE.

To solve this issue, it was decided to transfer the signals in the dq-frame rather than abc-frame to reduce the number of required analog output cards to two signals per variable instead of three signals. Also, active power could be computed on both OPAL-RT and dSPACE to free up one IO card. These available IO cards on OPAL-RT simulator were sufficient for this number of signals. However, another issue with implementing both controllers on dSPACE was the startup of the system. In the startup, the initial value of the signals might go beyond the voltage range of the IO cards of both simulators. Although scaling the signals is an option, it reduces the accuracy because the IO cards have a specific resolution. As a result, the controller does not receive the correct signals, and placing the controller in the loop does not stabilize the system.

To solve this issue, it was decided to start up the system on OPAL-RT and then place the controller in the loop. For doing so, the initial condition of the integrators in the control system must be sent to the dSPACE exactly at the time that the controller is placed in the loop. This requirement adds two analog IOs to the required signals per control loop, which exceeds the number of available IOs. All in all, due to the insufficient number of IO cards, it was decided to implement one controller in the dSPACE and the other controller on the OPAL-RT simulator.

Similar studies to the offline EMT simulations that were presented in Section 8.3 are repeated using the real-time simulation on the solo OPAL-RT simulator and using the HIL tests. Figs. 8.20-8.27 show the response of real-time simulation and HIL tests. The results of real-time simulations and HIL tests are similar to the offline simulations. Moreover, the results of HIL tests and real-time simulations are also close to each other. There are some discrepancies that will be explained in the following.

Based on Figs. 8.20-8.27, larger oscillations and noises in the results of HIL tests are observed. This issue is due to two reasons:

1) Improper cabling: Although BNC cables are used, which perform better than using loose wires, the wiring is not uniform and the connection is made using two types of wires/cables. The available noises in the connection of each cable to the other device or cable result in the difference between the waveforms of HIL test and real-time simulation. Employing custom-made cables would reduce the impact of noises on the waveforms.

2) Solution time-step: The solution time-step of the dPSACE cannot be smaller than

50 us, due to the hardware specifications. the In HIL tests, OPAL-RT simulator is run with a 10 us time-step, and dSPACE simulator is run with a 50 us time-step (the results were better than the case when both simulators are run with a 50 us time-step). On the other hand, the real-time simulations on the solo OPAL-RT simulator are performed with a 10 us time-step. As a result, the oscillations of the HIL tests are larger than the case when the real-time simulation is run on OPAL-RT using a 10 us time-step.

In Fig. 8.23, the HIL test results for the case of 2GFM converters are not presented due to the instability of the 2GFM system in the HIL tests. Although the system is stable in real-time simulation, it becomes unstable during HIL tests. The reason behind this discrepancy is the communication delays between the controller (dSPACE) and the simulator (OPAL-RT). To verify that the delay was the reason behind instability in HIL tests, a delay is imposed on the 2GFM converter system in the real-time simulation as well. The 2FGM converter system became unstable in this scenario as well. Therefore, it is observed that the 2GFM system is susceptible to communication delays.

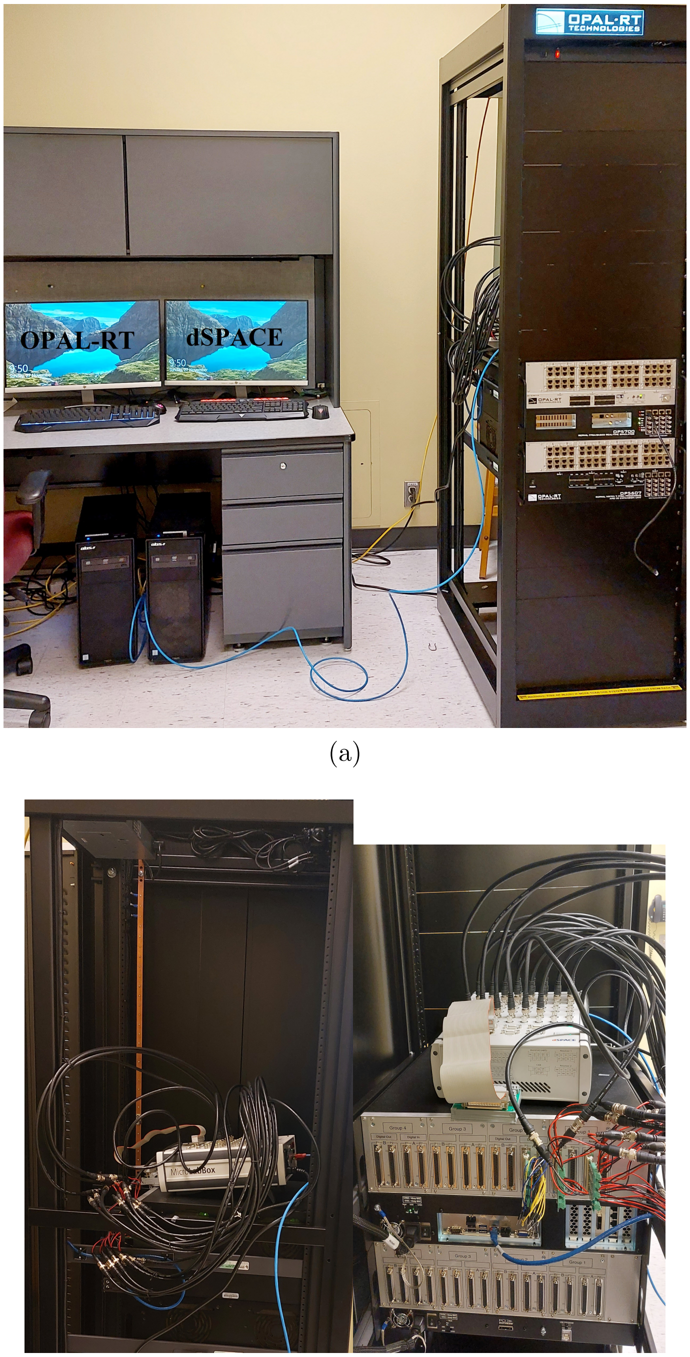

(a)

(b) (c)

Figure 8.19: Hardware-in-the-loop setup, a) host computers and OPAL-RT simulator, b) dSPACE simulator, and c) real-time simulator connection to the controller.

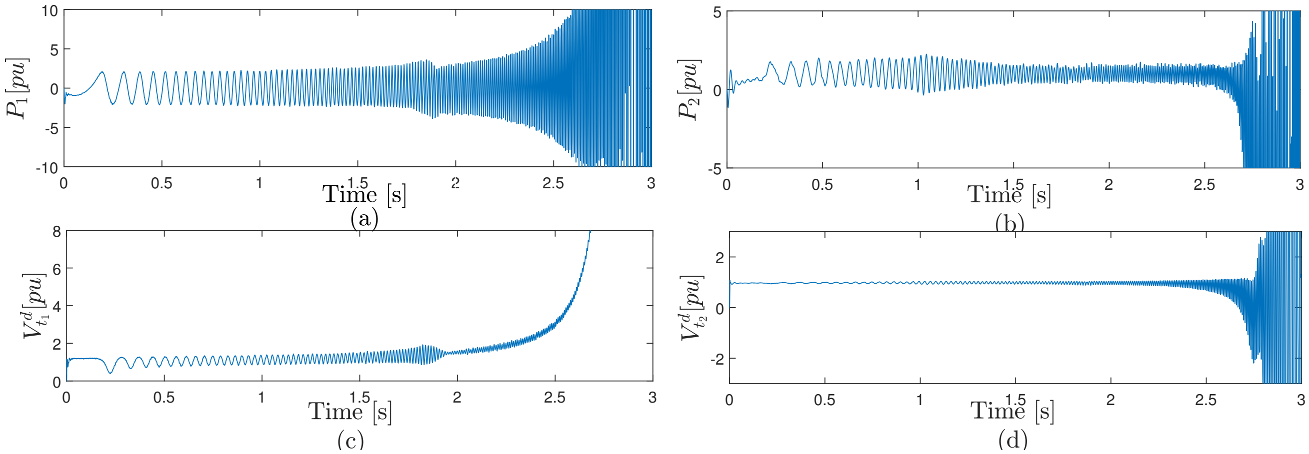

(a) (b) (c) (d)

Figure 8.20: Real-time simulation results: time-domain response of the 2-VSC under GFL, GFM control scheme for $L_{t_1} = 0.331$ and $L_{t_2} = 0.0291$.

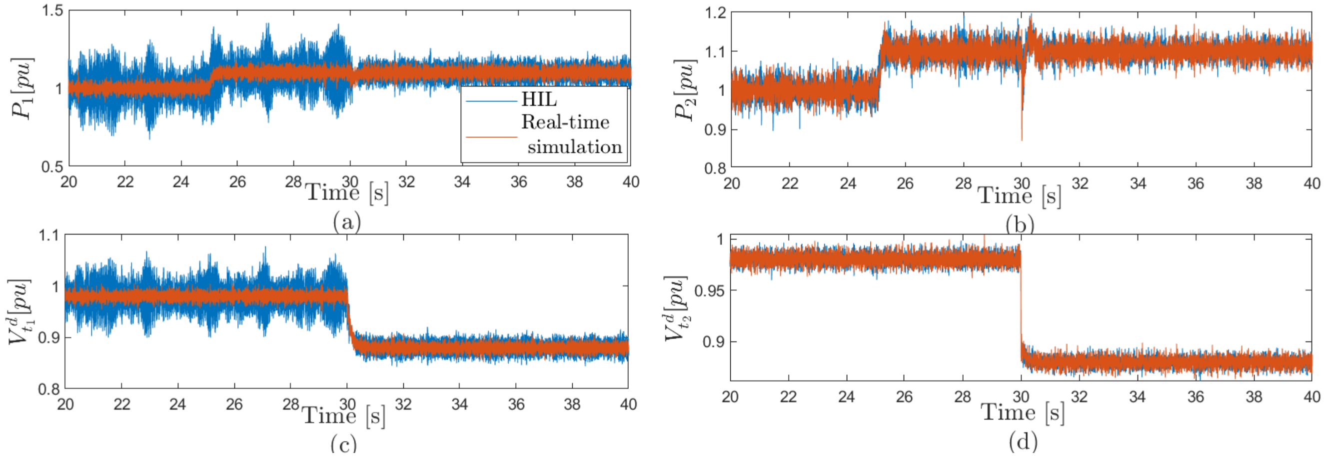

(a) (b) (c) (d)

Figure 8.21: HIL test results: time-domain response of the 2-VSC under GFL, GFM control scheme for $L_{t_1} = 0.0291$ and $L_{t_2} = 0.331$.

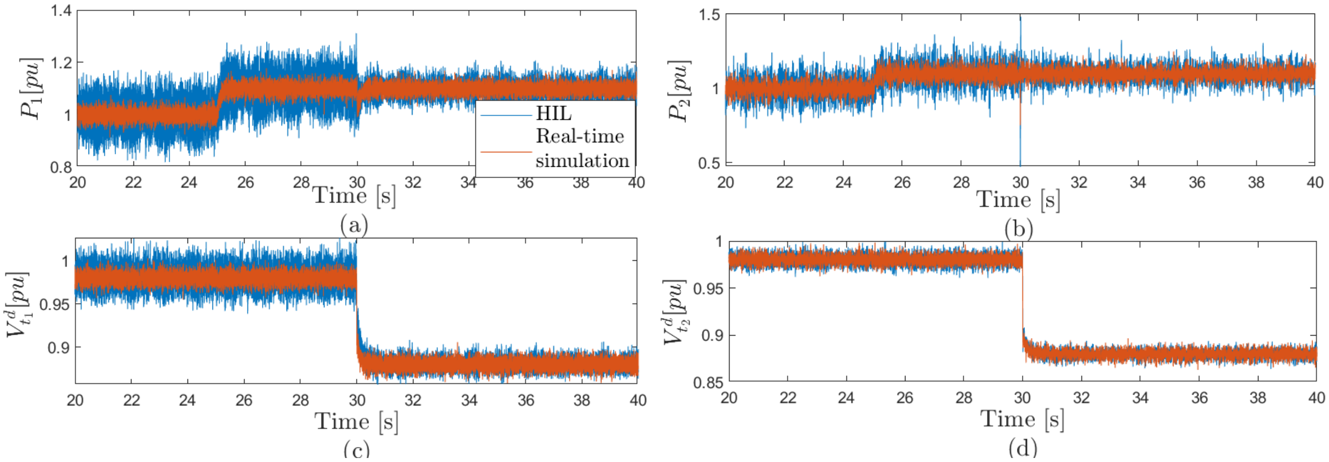

Figure 8.22: HIL test results: time-domain response of the 2-VSC under GFL (VSC_1), GFM (VSC_2) control scheme for $L_g = 0.1$

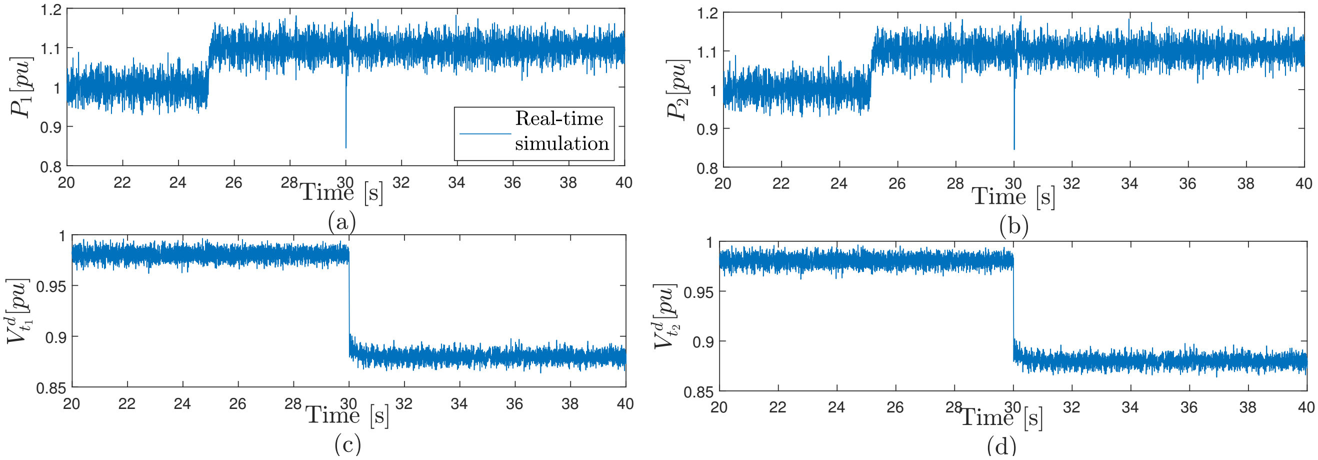

Figure 8.23: Real time simulation results: time-domain response of the 2-VSC under 2GFM control scheme for $L_g = 0.1$.

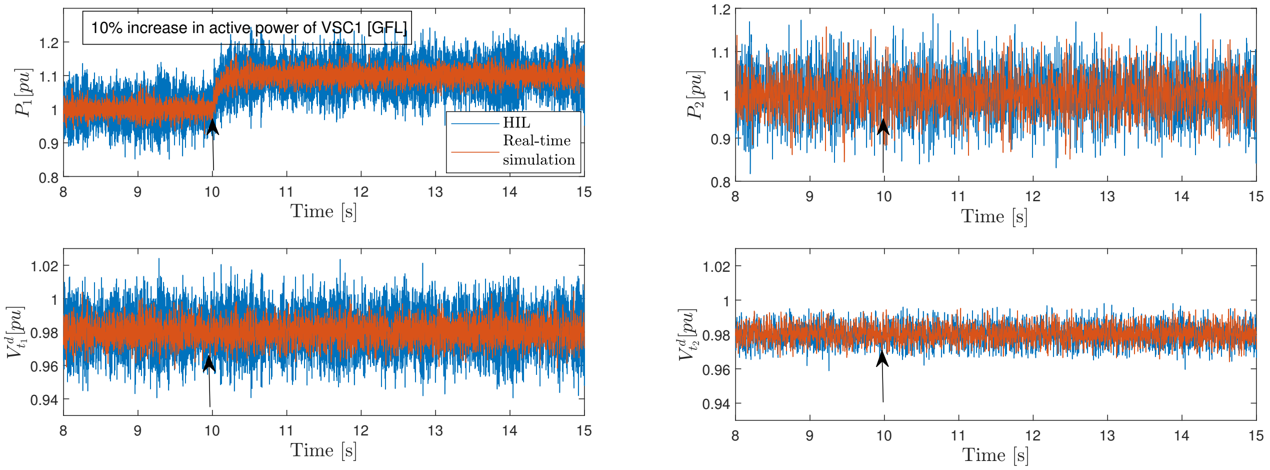

(a) VSC_1 (b) VSC_2

Figure 8.24: Comparison of HIL and real time simulation results: time-domain response of GFL, GFM 2-VSC system to a 10% increase in the active power of GFL converter.

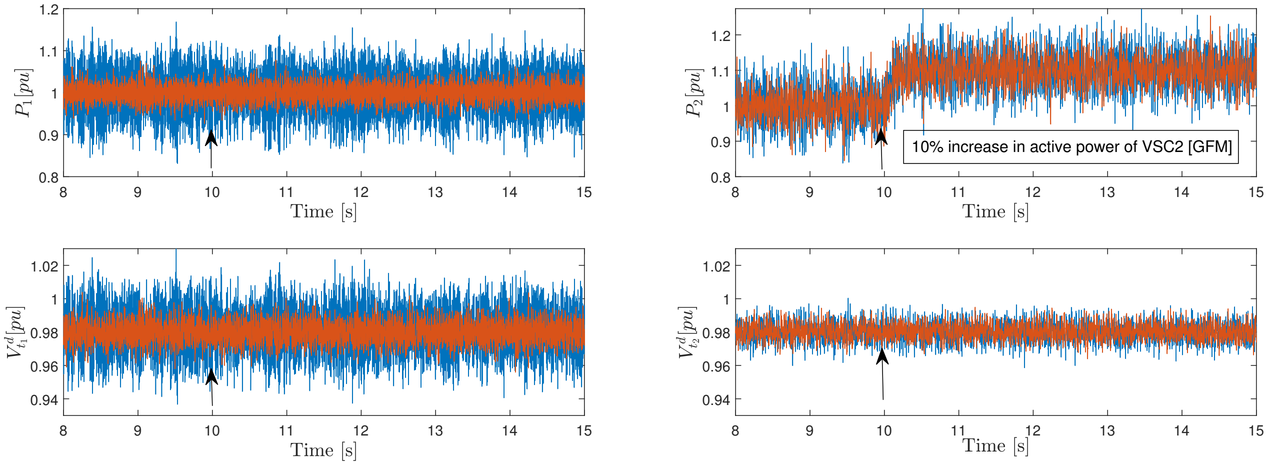

(a) VSC_1 (b) VSC_2

Figure 8.25: Comparison of HIL and real-time simulation results: time-domain response of GFL, GFM 2-VSC system to a 10% increase in the active power of GFM converter.

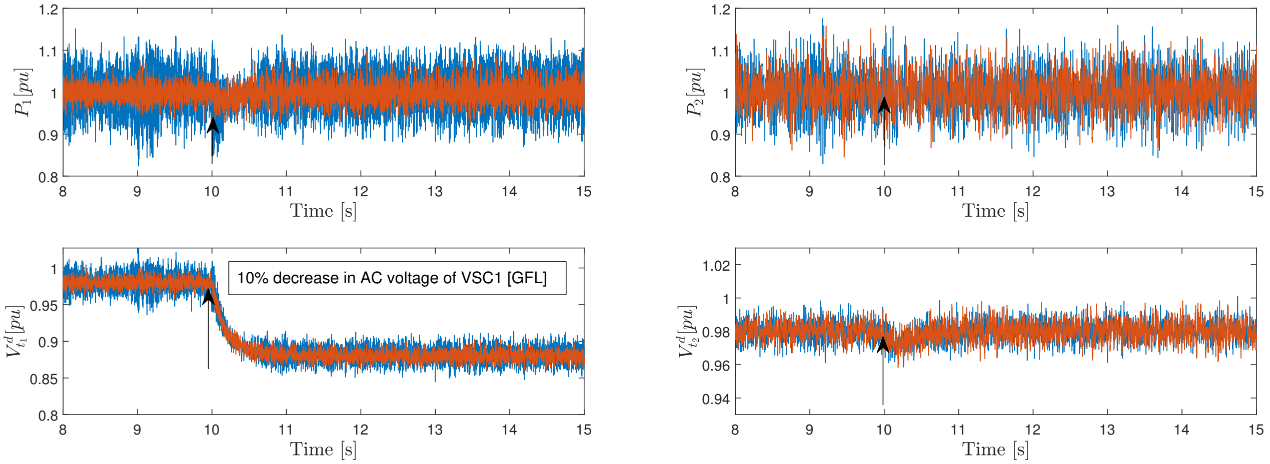

(a) VSC$_1$ (b) VSC$_2$

Figure 8.26: Comparison of HIL and real-time simulation results: time-domain response of GFL, GFM 2-VSC system to a 10% decrease in the AC voltage of GFL converter.

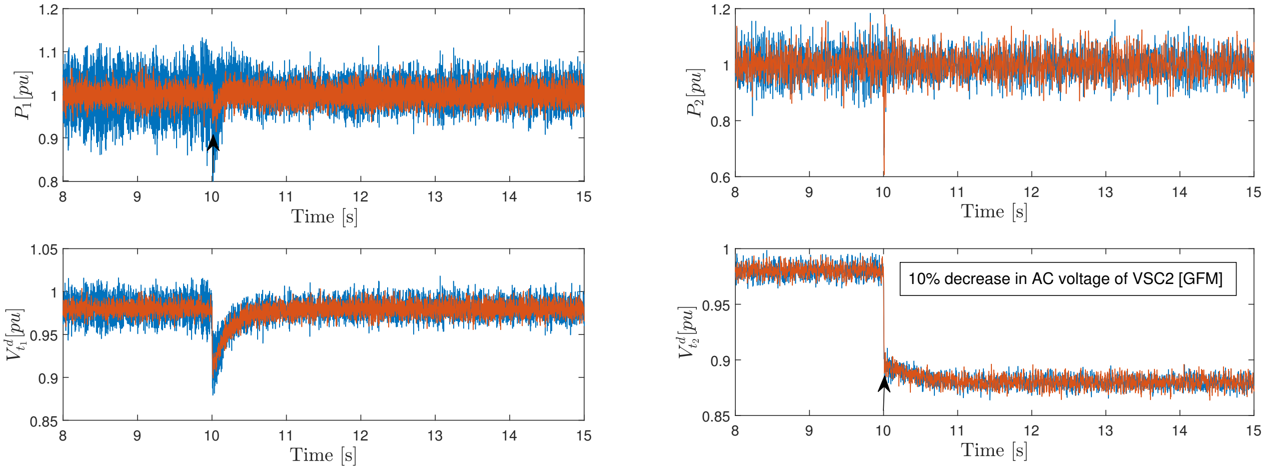

(a) VSC$_1$ (b) VSC$_2$

Figure 8.27: Comparison of HIL and real-time simulation results: time-domain response of GFL, GFM 2-VSC system to a 10% decrease in the AC voltage of GFM converter.

8.6 Conclusion

In this chapter, first, hybrid connections of grid-following (GFL) and grid-forming (GFM) converters were compared against each other in terms of stability and the level of interactions. Both GFM and GFL converters had similar control structures and an equal number of control parameters to make a fair comparison. Eigenvalue analysis indicated that the hybrid connection of GFL and GFM converters maintains stability for a large range of grid-inductance, while the connection of two GFL converters loses stability. Moreover, the GFM converters can be located farther from the PCC without negatively impacting system stability, while placing GFL converters at farther distances from PCC destabilizes the system. The coupling analysis using Bode diagrams of the off-diagonal closed-loop transfer functions showed that there exists a significant coupling between the AC voltage changes in the GFM converter and the active power/ AC voltage of the adjacent converter.

In the next part, the stability of parallel GFM converters connected to a shared AC system was investigated. Two types of GFM control schemes, namely PLL-based and non-PLL-based schemes were analyzed. Using matrix properties, it was analytically proved that the interconnected system with GFM VSCs maintains stability irrespective of the AC system SCR. Finally, the results of HIL tests and real-time simulations were used to validate the conclusions of this chapter.

Chapter 9

Conclusions and Future Work

9.1 Summary

This thesis focused on the control loop interactions in the voltage-sourced converter (VSC)-embedded AC-HVDC systems and investigated the impact of interactions on system stability and performance. The interactions were evaluated and studied from both the converter-level and system-level viewpoints. Furthermore, interactions were studied for different control philosophies, i.e., grid-following (GFL) and grid-forming (GFM) control schemes. In the following, the main conclusions of each chapter are presented:

- Chapter 1 provided introductory information on the subject of the thesis, stated the existing problems, and explained the objectives.
- Chapter 2 presented a comprehensive review of the available studies, which were categorized based on the type of interactions.
- Chapter 3 studied the internal control loop interactions in a single GFL VSC. This chapter studied how the interactions among various control loops in a single VSC affect the stability, transient response, and set-point tracking capability of control loops. The main contributions of the chapter are as follows: 1) The interaction studies in this chapter covered the various configurations of the control loops in a VSC, including DC voltage control loop (DVCL), active power control loop (APCL), AC voltage control loop (AVCL), and reactive power control loop (RPCL). 2) Using the theory of feedback interconnection of linear time-invariant (LTI) systems, the stability regions of interconnected control loops were obtained and compared against those of

the individual control loops to illustrate the impact of interactions on VSC stability. 3) A novel formulation of the VSC stability problem was presented, and the small-gain theorem is utilized to determine a range of stabilizing gains for the interconnected control system. 4) Several indices based on the infinity norm of transfer functions were introduced to study the impact of interactions on the transient response of the direct (d)-axis and quadrature (q)-axis control loops. 5) The impact of interactions on the set-point tracking capability of control loops was studied using the DC gain of specific transfer functions.

- Chapter 4 focused on the external control loop interactions among the VSCs that are connected to a shared DC system. This chapter presented a comparative system-level study to identify suitable individual system models that do not contain the internal dynamics of adjacent converters and only include the coupling dynamics corresponding to the interactive system modes among the converters. The use of these models for control design results in the dynamic response of the interconnected system being close to that of the individual system models. Such models can ensure interconnected stability when converter controllers are designed individually without requiring the complete model of the interconnected or internal dynamics of the adjacent converters.

- Chapter 5 elaborated upon external control loop interactions among VSCs sharing a common AC system and investigated the impact of control mode on the interactions. μ analysis was used to measure the level of interactions for various sets of control modes and develop a sufficient stability criterion for the independent design of converters' outer control loops such that the multi-VSC system stability is ensured. The main conclusions of this chapter are as follows: 1) The largest interactions occur if the adjacent converters simultaneously regulate the AC voltage via their q-axis control loop. 2) The joint control design of converters in AC voltage control mode such that the lowest number of converters in AC voltage control mode are designed independently is the best remedial action to reduce the impact of control loop interactions on the stability of multi-VSC systems.

- Chapter 6 focused on AC side external control loop interactions from the converters' designer viewpoint and developed a method to design the outer controllers of the converters individually such that the multi-VSC system becomes stable, and as a result, the interactions among the converters are mitigated. In this chapter, the stability criterion of a multi-VSC system was transformed into two distinct stability problems, in which the couplings among the converters are modelled by uncertainties. By converting these stability problems into conventional H_∞ problems, the outer controllers of the converters were designed. In the developed design method, converter interactions were incorporated as uncertainties in the system model and then mitigated through the design of a robust controller.

- Chapter 7 focused on AC side external control loop interactions from the grid integrator point of view and contributed to seamlessly integrating converters with independently designed controllers into a multi-VSC system. First, it was analytically shown how the integration of multiple converters into a multi-VSC system results in the deviation of the dynamic response of the interconnected system from that of the individual converters. Then, an H_∞ control problem was defined to design two interaction filters (IFs) per converter, one for the d-axis and one for the q-axis control loop, to simultaneously stabilize the multi-VSC system and minimize the perturbation of the dynamic response of the interconnected converters from the vendors' designed dynamic behaviour. Adding the IFs to the control system of converters did not cause new disruptive interactions, because the coupling dynamics among the converters are considered in designing the IFs. It was also analytically shown that employing the proposed IFs increases the robust stability margin of the multi-VSC system.
- Chapter 8 addressed AC side external control loop interactions in parallel converters with at least one GFM converter. In this chapter, various combinations of GFL and GFM converters were compared against each other in terms of the level of interactions. It was concluded that replacing a GFL converter with a GFM converter improves system stability; however, precautions have to be taken to tightly control the voltage of the GFM converter and as a result, not negatively interfere with the operation of the adjacent converter. The small-signal stability of parallel GFM converters was analytically studied as well. Using the properties of diagonally dominant matrices and matrix polynomials, it was proved that the parallel connection of GFM converters maintains small-signal stability regardless of the AC system short circuit ratio. In the last section of this chapter, the results of real-time simulations and hardware-in-the-loop tests were presented to validate the efficacy of the presented studies.

9.2 Contributions

The main contributions of this thesis are listed below and are categorized based on the type of control loop interactions:

- Internal control loop interactions

  - A novel stability framework is developed to mitigate the interactions.
  - A metric is proposed to measure the interaction levels.
  - A sequential control design is proposed by first tuning the d-axis controller, then PLL, and then the q-axis controller.
- DC side external control loop interactions: suitable individual models are identified to prevent the poorly damped or unstable modes by incorporating dynamics of certain components of the converters' DC side into these models.
- AC side external control loop interactions in grid-following converters
  - The impact of control modes on the interactions is analyzed, and the set of control modes causing the most severe interactions is identified.
  - A novel control design framework using μ analysis is developed to relate the control design of each converter to the interconnected system stability.
  - An interaction mitigation framework is developed from the designers' viewpoint by modeling the interactions as uncertainties and designing robust controllers using a reduced-order model of coupling dynamics.
  - An interaction mitigation framework is developed from the grid integrator viewpoint, by designing interaction filters. The filters are obtained by solving an H_∞ minimization problem. Employing the interaction filters stabilizes the system, and increases its robustness of the system.
- Interactions in parallel converters with GFM control philosophy
  - Coupling and stability analysis are performed for parallel connection of grid-following and GFM converters, and the most important measurement impacting the performance of the adjacent converter is identified.
  - The small-signal stability of parallel GFM converters is analytically proved.
  - Real-time simulations and hardware-in-the-loop tests are performed.

9.3 Future Work

Given the broadness of the topic, further research can be carried out to address the following issues:

- Interaction studies among the converters with simultaneous connections both at the DC side and AC side can be carried out.

- While the current control is the most widely used control approach for GFL converters, there is no such consensus for GFM converters. Therefore, various GFM control schemes can be compared against each other and evaluated in terms of the level of interactions and system stability.

- The GFM converter in this thesis operates under the active-power control mode. Controlling the DC voltage through a GFM converter has rarely been studied in the literature. Having a GFM converter under the DC voltage control mode and simultaneous operation of such converters with GFL converters in MTDC systems can be evaluated in terms of stability and level of interactions.

- Transient stability of parallel VSCs with GFM converter schemes should be evaluated to further study the impact of GFM converters on system stability.

- Including supplementary control loops such as frequency support in the control system and its impact on the mutual interactions among the converters can be studied.

- Interaction among the converters under fault scenarios and the resilience of each control philosophy can be studied using fault-tolerant control approaches.

- The analysis of hybrid connections of GFL and GFM converters in this thesis has only been performed on a 2-VSC system. Another interesting scenario would be a 3-VSC system with two GFL converters and one GFM converter, or one GFL converter and two GFM converters.

- The interactions between DC/DC converters and DC/AC converters in future MTDC systems can be studied.

References

[1] https://pdf.directindustry.com/pdf/siemens-high-voltage-power-transmission/hvdc-high-voltage-direct-current-transmission-unrivaled-practical-experience/32878-889677-_4.html.

[2] https://www.gegridsolutions.com/products/brochures/powerd_vtf/hvdc-systems_gea-31971_lr.pdf.

[3] Best Paths publications, http://bestpaths-project.eu/en/publications.

[4] https://www.pscad.com/knowledge-base/article/191?module_id=1.

[5] 3-terminal hvdc link with 2-level vsc terminals. https://www.pscad.com/knowledge-base/article/191.

[6] The eleclink project. http://www.eleclink.co.uk.

[7] Hvdc projects listing prepared for the hvdc and flexible ac transmission subcommittee of the ieee transmission and distribution committee. http://www.ece.uidaho.edu/hvdcfacts/Projects/HVDCProjectsListingMarch2012.

[8] Hvdc webinar sessions on emt interaction studies using simulation tools. https://www.rte-international.com/hvdc-webinar-sessions-on-emt-interaction-studies-using-simulation-tools/?lang=en.

[9] Hvdc webinar, third session, the johan sverdrup hvdc project – first multivendor hvdc system in grid forming operation. https://www.rte-international.com/webinar-sessions-on-hvdc-interaction-studies-with-emt-simulation-tools/?lang=en.

[10] International energy association. https://www.iea.org/.

[11] Protection and local control of HVDC-grids, working group B4/B5.59. *Cigré*, 2018.

[12] Aswad Adib, Behrooz Mirafzal, Xiongfei Wang, and Frede Blaabjerg. On stability of voltage source inverters in weak grids. *Ieee Access*, 6:4427–4439, 2018.

[13] Adedotun J Agbemuko, José Luis Domínguez-García, and Oriol Gomis-Bellmunt. Robust decentralized approach to interaction mitigation in VSC-HVDC grids through impedance minimization. *Control Engineering Practice*, page 104346, 2020.

[14] Adedotun J Agbemuko, José Luis Domínguez-García, and Oriol Gomis-Bellmunt. Robust decentralized approach to interaction mitigation in vsc-hvdc grids through impedance minimization. *Control Engineering Practice*, 118:104346, 2022.

[15] Adedotun J Agbemuko, Jose Luis Dominguez-Garcia, Oriol Gomis-Bellmunt, and Lennart Harnefors. Passivity-based analysis and performance enhancement of a vector controlledVSCconnected to a weak AC grid. *IEEE Transactions on Power Delivery*, 2020.

[16] Adedotun J Agbemuko, José Luis Domínguez-García, Eduardo Prieto-Araujo, and Oriol Gomis-Bellmunt. Advanced impedance-based control design for decoupling multi-vendor converter hvdc grids. *IEEE Transactions on Power Delivery*, 35(5):2459–2470, 2020.

[17] Fatemeh Ahmadloo and Sahar Pirooz Azad. A comparative study on control loop interactions in vsc-hvdc systems. In *2020 IEEE Power & Energy Society General Meeting (PESGM)*, pages 1–5. IEEE, 2020.

[18] Fatemeh Ahmadloo and Sahar Pirooz Azad. Analysis of internal control loop interactions in vscs: An individual design perspective. *IEEE Transactions on Power Delivery*, 37(3):1465–1475, 2021.

[19] Fatemeh Ahmadloo and Sahar Pirooz Azad. The impact of control modes on the external control loop interactions in VSC-HVDC systems. In *2021 IEEE Power & Energy Society General Meeting.*

[20] Samy Akkari. *Control of a multi-terminal HVDC (MTDC) system and study of the interactions between the MTDC and the AC grids.* PhD thesis, 2016.

[21] Khaled Mohammad Alawasa, Yasser Abdel-Rady I Mohamed, and Wilsun Xu. Modeling, analysis, and suppression of the impact of full-scale wind-power converters on subsynchronous damping. *IEEE Systems Journal*, 7(4):700–712, 2013.

[22] Khaled Mohammad Alawasa, Yasser Abdel-Rady Ibrahim Mohamed, and Wilsun Xu. Active mitigation of subsynchronous interactions between pwm voltage-source converters and power networks. *IEEE Transactions on Power Electronics*, 29(1):121–134, 2013.

[23] Mohammadreza Fakhari Moghaddam Arani and Yasser Abdel-Rady I Mohamed. Analysis and performance enhancement of vector-controlled vsc in hvdc links connected to very weak grids. *IEEE Transactions on Power Systems*, 32(1):684–693, 2016.

[24] Sakthivel Arunprasanth, Udaya D Annakkage, Chandana Karawita, and Rick Kuffel. Generalized frequency-domain controller tuning procedure for vsc systems. *IEEE Transactions on Power Delivery*, 31(2):732–742, 2015.

[25] Jef Beerten, Salvatore D'Arco, and Jon Are Suul. Identification and small-signal analysis of interaction modes in vsc mtdc systems. *IEEE Transactions on Power Delivery*, 31(2):888–897, 2015.

[26] Mokhtar Benasla, Tayeb Allaoui, Mostefa Brahami, Mouloud Denai, and Vijay K Sood. Hvdc links between north africa and europe: Impacts and benefits on the dynamic performance of the european system. *Renewable and Sustainable Energy Reviews*, 82:3981–3991, 2018.

[27] Geraint Chaffey, Md Habibur Rahman, Frederick Page, Ilka Jahn, Bharath Ponnalagan, Keisuke Ishida, Linash Kunjumuhammed, Mian Wang, Dirk Van Hertem, and Ian Cowan. Demonstration of multi-vendor protection systems for multiterminal VSC-HVDC networks. In *2021 IEEE Madrid PowerTech*, pages 1–6. IEEE, 2021.

[28] S Cole and R Belmans. A proposal for standard vsc hvdc dynamic models in power system stability studies. *Electric Power Systems Research*, 81(4):967–973, 2011.

[29] Stijn Cole, Jef Beerten, and Ronnie Belmans. Generalized dynamic vsc mtdc model for power system stability studies. *IEEE Transactions on power systems*, 25(3):1655–1662, 2010.

[30] Salvatore D'Arco, Jef Beerten, and JA Suul. Classification and analysis of impact on small-signal dynamics and stability from expansion of vsc-hvdc systems to multi-terminal hvdc grids. In *13th IET International Conference on AC and DC Power Transmission (ACDC 2017)*, pages 1–8. IET, 2017.

[31] Masoud Davari and Yasser Abdel-Rady I Mohamed. Robust vector control of a very weak-grid-connected voltage-source converter considering the phase-locked loop dynamics. *IEEE Transactions on Power Electronics*, 32(2):977–994, 2016.

[32] O Despouys, P Rault, A Burgos, D Vozikis, X Guillaud, and T Larsson. Assessment of interoperability in multi-vendor VSC-HVDC systems: interim results of the best paths demo# 2. 2018.

[33] John C Doyle, Bruce A Francis, and Allen R Tannenbaum. *Feedback control theory.* Courier Corporation, 2013.

[34] Wenjuan Du, Qiang Fu, and Haifeng Wang. Small-signal stability of an ac/mtdc power system as affected by open-loop modal coupling between the vscs. *IEEE Transactions on Power Systems*, 33(3):3143–3152, 2017.

[35] Agustí Egea-Alvarez, Sajjad Fekriasl, Fainan Hassan, and Oriol Gomis-Bellmunt. Advanced vector control for voltage source converters connected to weak grids. *IEEE Transactions on Power Systems*, 30(6):3072–3081, 2015.

[36] Robert Eriksson. Current sharing in multiterminal dc grids—the analytical approach. *IEEE Transactions on Power Systems*, 33(6):6278–6288, 2018.

[37] Robert Eriksson, Jef Beerten, Mehrdad Ghandhari, and Ronnie Belmans. Optimizing dc voltage droop settings for ac/dc system interactions. *IEEE Transactions on Power Delivery*, 29(1):362–369, 2013.

[38] David G Feingold and Richard S Varga. Block diagonally dominant matrices and generalizations of the gerschgorin circle theorem. *Pacific Journal of Mathematics*, 12(4):1241–1250, 1962.

[39] Julian Freytes, François Gruson, Frédéric Colas, Pierre Rault, Hani Saad, and Xavier Guillaud. Simplified model of droop-controlled mtdc grid-influence of mmc energy management on dc system dynamics. In *2018 Power Systems Computation Conference (PSCC)*, pages 1–7. IEEE, 2018.

[40] Qiang Fu, Wenjuan Du, Haifeng Wang, Bixing Ren, and Xianyong Xiao. Small-signal stability analysis of a vsc-mtdc system for investigating dc voltage oscillation. *IEEE Transactions on Power Systems*, 2021.

[41] Michael Green and David JN Limebeer. *Linear robust control.* Courier Corporation, 2012.

[42] IEEE Working Group et al. Ieee guide for planning dc links terminating at ac locations having low short-circuit capacities, 1997.

[43] Minyuan Guan, Wulue Pan, Jing Zhang, Quanrui Hao, Jingzhou Cheng, and Xiang Zheng. Synchronous generator emulation control strategy for voltage source converter (vsc) stations. *IEEE Transactions on Power Systems*, 30(6):3093–3101, 2015.

[44] Yunhui Huang and Dong Wang. Effect of control-loops interactions on power stability limits of vsc integrated to ac system. *IEEE Transactions on Power Delivery*, 33(1):301–310, 2017.

[45] Yunhui Huang, Dong Wang, Lei Shang, Guorong Zhu, Haiyan Tang, and Yan Li. Modeling and stability analysis of dc-link voltage control in multi-vscs with integrated to weak grid. *IEEE Transactions on Energy Conversion*, 32(3):1127–1138, 2017.

[46] Yunhui Huang, Xiaoming Yuan, Jiabing Hu, and Pian Zhou. Modeling of vsc connected to weak grid for stability analysis of dc-link voltage control. *IEEE Journal of Emerging and Selected Topics in Power Electronics*, 3(4):1193–1204, 2015.

[47] Yunhui Huang, Xiaoming Yuan, Jiabing Hu, Pian Zhou, and Dong Wang. Dc-bus voltage control stability affected by ac-bus voltage control in vscs connected to weak ac grids. *IEEE Journal of Emerging and Selected Topics in Power Electronics*, 4(2):445–458, 2015.

[48] Conseil international des grands réseaux électriques. Comité d'études B4. *Guide for the Development of Models for HVDC Converters in a HVDC Grid*. CIGRÉ, 2014.

[49] Prabha Kundur. Power system stability. *Power system stability and control*, 10, 2007.

[50] Robert H Lasseter, Zhe Chen, and Dinesh Pattabiraman. Grid-forming inverters: A critical asset for the power grid. *IEEE Journal of Emerging and Selected Topics in Power Electronics*, 8(2):925–935, 2019.

[51] Bin Li and Lin Zhou. Power decoupling method based on the diagonal compensating matrix for vsg-controlled parallel inverters in the microgrid. *Energies*, 10(12):2159, 2017.

[52] Guiyuan Li, Zhengchun Du, Ting An, Yuan Xia, and Jingting Lei. Impact of pll and vsc control parameters on the ac/mtdc systems stability. *Electric Power Systems Research*, 141:476–486, 2016.

[53] Yujun Li, Jiapeng Li, Huangqing Xiao, Jianliang Zhang, and Zhengchun Du. Stability analysis of droop-based converter using siso method from dc side perturbation. *IEEE Transactions on Power Delivery*, 36(5):3150–3161, 2020.

[54] Yunfeng Li, Guangfu Tang, Jun Ge, Zhiyuan He, Hui Pang, Jie Yang, and Yanan Wu. Modeling and damping control of modular multilevel converter based dc grid. *IEEE Transactions on Power Systems*, 33(1):723–735, 2017.

[55] Zhou Li, Yan He, Ya-Zhou Li, Wei Gu, Yi Tang, and Xiao-Ping Zhang. Hybrid control strategy for ac voltage stabilization in bipolar vsc-mtdc. *IEEE Transactions on Power Systems*, 34(1):129–139, 2018.

[56] Jia Liu, Yushi Miura, and Toshifumi Ise. Comparison of dynamic characteristics between virtual synchronous generator and droop control in inverter-based distributed generators. *IEEE Transactions on Power Electronics*, 31(5):3600–3611, 2015.

[57] Yingpei Liu, Sai Xie, Haiping Liang, and Hanyang Cui. Coordinated control strategy of multi-terminal vsc-hvdc system considering frequency stability and power sharing. *IET Generation, Transmission & Distribution*, 13(22):5188–5196, 2019.

[58] Katsuhiko Ogata and Yanjuan Yang. *Modern control engineering*, volume 5. Prentice hall Upper Saddle River, NJ, 2010.

[59] Gustavo Pinares and Massimo Bongiorno. Modeling and analysis of vsc-based hvdc systems for dc network stability studies. *IEEE Transactions on Power Delivery*, 31(2):848–856, 2015.

[60] Eduardo Prieto-Araujo, Agustí Egea-Alvarez, Sajjad Fekriasl, and Oriol Gomis-Bellmunt. Dc voltage droop control design for multiterminal hvdc systems considering ac and dc grid dynamics. *IEEE Transactions on Power Delivery*, 31(2):575–585, 2015.

[61] Taoufik Qoria, François Gruson, Frédéric Colas, Xavier Guillaud, Marie-Sophie Debry, and Thibault Prevost. Tuning of cascaded controllers for robust grid-forming voltage source converter. In *2018 Power Systems Computation Conference (PSCC)*, pages 1–7. IEEE, 2018.

[62] Taoufik Qoria, Ebrahim Rokrok, Antoine Bruyere, Bruno François, and Xavier Guillaud. A pll-free grid-forming control with decoupled functionalities for high-power transmission system applications. *IEEE Access*, 8:197363–197378, 2020.

[63] Dayan B Rathnayake, Milad Akrami, Chitaranjan Phurailatpam, Si Phu Me, Sajjad Hadavi, Gamini Jayasinghe, Sasan Zabihi, and Behrooz Bahrani. Grid forming inverter modeling, control, and applications. *IEEE Access*, 2021.

[64] P Rault and O Despouys. D9.3: Best paths demo# 2 final recommendations for interoperability of multivendor HVDC systems. 2018.

[65] Ebrahim Rokrok, Taoufik Qoria, Antoine Bruyere, Bruno Francois, and Xavier Guillaud. Classification and dynamic assessment of droop-based grid-forming control schemes: Application in hvdc systems. *Electric Power Systems Research*, 189:106765, 2020.

[66] Ebrahim Rokrok, Taoufik Qoria, Antoine Bruyere, Bruno Francois, and Xavier Guillaud. Transient stability assessment and enhancement of grid-forming converters embedding current reference saturation as current limiting strategy. *IEEE Transactions on Power Systems*, 37(2):1519–1531, 2021.

[67] Roberto Rosso, Markus Andresen, Soenke Engelken, and Marco Liserre. Analysis of the interaction among power converters through their synchronization mechanism. *IEEE Transactions on Power Electronics*, 34(12):12321–12332, 2019.

[68] Roberto Rosso, Giampaolo Buticchi, Marco Liserre, Zhixiang Zou, and Soenke Engelken. Stability analysis of synchronization of parallel power converters. In *IECON 2017-43rd Annual Conference of the IEEE Industrial Electronics Society*, pages 440–445. IEEE, 2017.

[69] Roberto Rosso, Soenke Engelken, and Marco Liserre. Analysis of the parallel operation between synchronverters and pll-based converters. In *2019 IEEE Energy Conversion Congress and Exposition (ECCE)*, pages 2583–2590. IEEE.

[70] Roberto Rosso, Soenke Engelken, and Marco Liserre. Robust stability investigation of the interactions among grid-forming and grid-following converters. *IEEE Journal of Emerging and Selected Topics in Power Electronics*, 8(2):991–1003, 2019.

[71] Santiago Sanchez, Alejandro Garces, Gilbert Bergna-Diaz, and Elisabetta Tedeschi. Dynamics and stability of meshed multiterminal hvdc networks. *IEEE Transactions on Power Systems*, 34(3):1824–1833, 2018.

[72] L Shen, M Barnes, Jovica V Milanovic, Keith RW Bell, and Manolis Belivanis. Potential interactions between vsc hvdc and statcom. In *2014 Power Systems Computation Conference*, pages 1–7. IEEE, 2014.

[73] Li Shen, Mike Barnes, Robin Preece, Jovica V Milanovic, Keith Bell, and Manolis Belivanis. The effect of vsc-hvdc control on ac system electromechanical oscillations and dc system dynamics. *IEEE Transactions on Power Delivery*, 31(3):1085–1095, 2015.

[74] Leang Shieh, Mohamad Mehio, and Hani Dib. Stability of the second-order matrix polynomial. *IEEE Transactions on Automatic control*, 32(3):231–233, 1987.

[75] Sigurd Skogestad and Ian Postlethwaite. *Multivariable feedback control: analysis and design*, volume 2. Citeseer, 2007.

[76] I Staffell, M Jansen, A Chase, E Cotton, and C Lewis. Energy revolution: global outlook. *Drax: Selby*, 2018.

[77] Ngoc-Tuan Trinh, Marcus Zeller, Klaus Wuerflinger, and Istvan Erlich. Generic model of mmc-vsc-hvdc for interaction study with ac power system. *IEEE Transactions on Power Systems*, 31(1):27–34, 2015.

[78] Dirk Van Hertem and Mehrdad Ghandhari. Multi-terminal vsc hvdc for the european supergrid: Obstacles. *Renewable and sustainable energy reviews*, 14(9):3156–3163, 2010.

[79] Cheng Wan, Meng Huang, K Tse Chi, and Xinbo Ruan. Effects of interaction of power converters coupled via power grid: A design-oriented study. *IEEE Transactions on Power Electronics*, 30(7):3589–3600, 2014.

[80] Dong Wang, Yunhe Hou, and Jiabing Hu. Effect of ac voltage control on the stability of weak ac grid connected dfig system. In *2016 IEEE PES Asia-Pacific Power and Energy Engineering Conference (APPEEC)*, pages 1528–1533. IEEE, 2016.

[81] Dong Wang, Liang Liang, Lei Shi, Jiabing Hu, and Yunhe Hou. Analysis of modal resonance between PLL and DC- link voltage control in weak-grid tied vscs. *IEEE Transactions on Power Systems*, 34(2):1127–1138, 2018.

[82] Dong Wang, Xiaojie Zhang, Lei Yang, Yunhui Huang, Wei Huang, Chen Wu, and Shengnan Li. Analysis of synchronization stability for multi vscs parallel-connected to weak grids by improved net damping criterion. *Energies*, 13(13):3316, 2020.

[83] Wenyuan Wang, Antony Beddard, Mike Barnes, and Ognjen Marjanovic. Analysis of active power control for vsc–hvdc. *IEEE Transactions on Power Delivery*, 29(4):1978–1988, 2014.

[84] Yizhen Wang, Weijie Wen, Chengshan Wang, Haitao Liu, Xin Zhan, and Xiaolong Xiao. Adaptive voltage droop method of multiterminal vsc-hvdc systems for dc voltage deviation and power sharing. *IEEE Transactions on Power Delivery*, 34(1):169–176, 2018.

[85] Chaoran Yang, Linbin Huang, Huanhai Xin, and Ping Ju. Placing grid-forming converters to enhance small signal stability of pll-integrated power systems. *IEEE Transactions on Power Systems*, 36(4):3563–3573, 2020.

[86] Amirnaser Yazdani and Reza Iravani. *Voltage-sourced converters in power systems: modeling, control, and applications*. John Wiley & Sons, 2010.

[87] Amirthagunaraj Yogarathinam and Nilanjan Ray Chaudhuri. Stability-constrained adaptive droop for power sharing in ac-mtdc grids. *IEEE Transactions on Power Systems*, 34(3):1955–1965, 2019.

[88] Hao Yuan, Xiaoming Yuan, and Jiabing Hu. Modeling of grid-connected vscs for power system small-signal stability analysis in dc-link voltage control timescale. *IEEE Transactions on Power Systems*, 32(5):3981–3991, 2017.

[89] Zheng Yuan, Du Zhengchun, and Guiyuan Li. Analysis on the dynamic behaviours and interactions of vsc-mtdc grid. *IET Generation, Transmission & Distribution*, 12(8):1756–1764, 2018.

[90] Lidong Zhang, Lennart Harnefors, and Hans-Peter Nee. Power-synchronization control of grid-connected voltage-source converters. *IEEE Transactions on Power systems*, 25(2):809–820, 2010.

[91] Fangzhou Zhao, Xiongfei Wang, Zichao Zhou, Lennart Harnefors, Jan R Svensson, Łukasz Hubert Kocewiak, and Mikkel Peter Sidoroff Gryning. Control interaction modeling and analysis of grid-forming battery energy storage system for offshore wind power plant. *IEEE Transactions on Power Systems*, 37(1):497–507, 2021.

[92] Wanning Zheng, Jiabing Hu, and Xiaoming Yuan. Modeling of vscs considering input and output active power dynamics for multi-terminal hvdc interaction analysis in dc voltage control timescale. *IEEE Transactions on Energy Conversion*, 34(4):2008–2018, 2019.

[93] Qing-Chang Zhong and George Weiss. Synchronverters: Inverters that mimic synchronous generators. *IEEE transactions on industrial electronics*, 58(4):1259–1267, 2010.

[94] Jenny Z Zhou, Hui Ding, Shengtao Fan, Yi Zhang, and Aniruddha M Gole. Impact of short-circuit ratio and phase-locked-loop parameters on the small-signal behavior¡? pub _bookmark="" command="[quick mark]"?¿ of a vsc-hvdc converter. *IEEE Transactions on Power Delivery*, 29(5):2287–2296, 2014.

[95] Jenny Z Zhou and Aniruddha M Gole. Vsc transmission limitations imposed by ac system strength and ac impedance characteristics. 2012.

[96] Kemin Zhou and John Comstock Doyle. *Essentials of robust control*, volume 104. Prentice hall Upper Saddle River, NJ, 1998.

[97] Pian Zhou, Xiaoming Yuan, Jiabing Hu, and Yunhui Huang. Stability of dc-link voltage as affected by phase locked loop in vsc when attached to weak grid. In *2014 IEEE PES General Meeting— Conference & Exposition*, pages 1–5. IEEE, 2014.

[98] Zhixiang Zou, Jian Tang, Xiongfei Wang, Zheng Wang, Wu Chen, Giampaolo Buticchi, and Marco Liserre. Modeling and control of a two-bus system with grid-forming and grid-following converters. *IEEE Journal of Emerging and Selected Topics in Power Electronics*, 2022.